UNIVERSITÀ DEGLI STUDI DI PARMA

PhD course in Drugs, Biomolecules and Health Products

XXIX cycle

THERMODYNAMICS OF THE INTERACTION BETWEEN BIOLOGICALLY ACTIVE MOLECULES AND SUBSTRATES OF PHARMACEUTICAL INTEREST

Coordinator:
Chiar.mo Prof. Marco MOR

Supervisor:
Chiar.ma Prof.ssa Emilia FISICARO

PhD student:
Dr Laura CONTARDI

To my parents

Table of contents

PRAEFATIO

My research study is divided into two main topics:

1. gemini cationic surfactants, both hydrogenated and partially fluorinated, their mechanism in gene delivery and as potential lung surfactants for the treatment of Acute Lung Injury (ALI) and Acute Respiratory Distress Syndrome (ARDS);
2. study of new ligands potential metal-enzymes inhibitors, to be used as antivirals, for which we are always in search of new molecules due to the onset of resistances.

PART 1

GENE DELIVERY VECTORS

Chapter I

Cationic gemini surfactants

1. INTRODUCTION

INTRODUCTION

Gene therapy is a procedure used to improve the health by modifying the patient's cells genetically[1]. By delivering a therapeutic gene material and its associated regulatory elements into the nucleus is possible to treat both inherited and acquired diseases. In this way, the loss of function caused by mutation can be corrected or the deficient gene can be expressed at physiologic levels[2].

Two methods can be used to deliver genes: *ex vivo* and *in vivo* transfection. During the *ex vivo* transfection, cloned genes are transferred. Normally patient cells (autologous transfection) are used to avoid rejection. In particular, the cells are removed, selected for expression of the gene to be inserted, amplified and reintroduced into the patient's body. This is possible only with tissues that can be removed from the body, genetically engineered and re-introduced into the patient where they grow and survive for a long period of time, as for skin cells or hematopoietic system cells. This procedure is time and cost expensive but it allows to select and amplify the interested cells with high efficiency.

The *in vivo* gene therapy is used when the cells cannot be removed and replanted, such as for cardiac or nervous cells. In this case, the gene of interest is introduced by means of a vector into the organism, through systemic or local access. It is the most difficult protocol to apply but represents a cheaper therapeutic model with a high compliance.

To obtain better results, genetically engineered viral vectors are generally used. The viral genome is removed maintaining the ability to transfect but losing the capability to generate the infection but maintains the ability to transfect: it behaves in this way like a "Trojan horse". The clinical application of gene therapy has been investigated over the past two decades[3].

The major obstacle for gene therapy success is the difficulty to find the viral system with the ability to transfect the targeted cells. Besides, they present some risks too, such as producing a reaction by the immune systems. In addition viral vectors present the possibility of the ectopic chromosomal integration of viral DNA which disrupts the expression of tumor suppressor gene or activates oncogenes leading to the malignant transformation of cells. This is why non-viral vectors have important safety advantage over viral approaches: they tend to show lower immunogenicity and patients do not have pre-existing immunity. They are generally easier to produce than viral vectors[4,5] and they can potentially load and deliver larger genetic materials. However, non-viral delivery systems with high transfection efficiency must still be realized.

1.1 Barriers to non-viral DNA delivery.

One of the challenges to systemic delivery of DNA therapeutics is the potential degradation of the therapeutic gene by endonucleases in physiological fluids and the extracellular space.

The half-life of plasmid DNA has been estimated to be ten minutes following intravenous injection in mice[6]. For this reason, the encapsulation of DNA in a carrier is desirable to provide protection from endonuclease degradation and also to improve its half-life in the blood. For example, zwitterionic lipids have been shown to form a stable structure that envelops DNA and can be used in combination with other formulations to enhance gene delivery *in vivo*[7]. Cationic lipids mixed with neutral lipids and DNA, can originate spontaneously lipoplexes or liposomes. However, at high salt concentrations, electrostatic repulsion between the positively charged complexes is reduced, and they are therefore prone to colloidal instability and aggregation in physiological fluids[8]. In

particular, as a result of colloidal instability or interaction with blood components (such as serum proteins and erythrocytes), the aggregation of nanoparticles in the blood can inhibit localization to the desired tissues, induce rapid clearance by circulating macrophages and even cause embolism in lung capillaries[9]. DNA delivery must also provide transport into the nucleus to allow access to the transcriptional machinery. A non-viral vector, in order to enter the cell, must first cross the plasma membrane[10,11] via different ways, as shown in Figure 1.

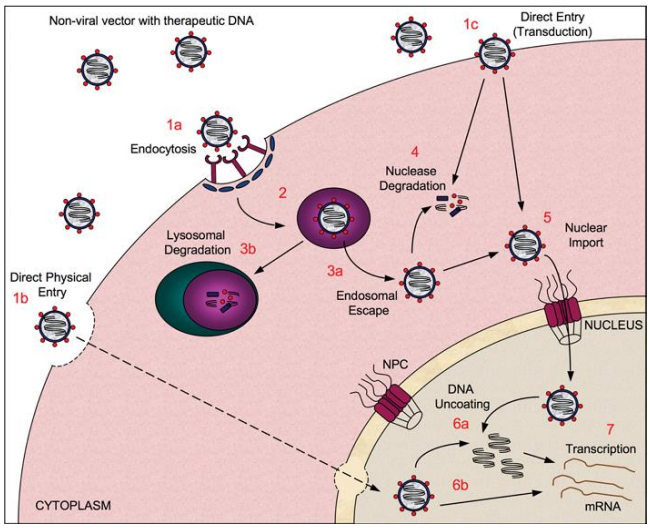

Figure 1. Barriers to successful *in vivo* delivery of nucleic acids using non-viral vectors. A non-viral vector, to enter the cell, must cross the plasma membrane via different ways, including endocytosis-based entry (1a), with a direct physical entry, such as electroporation (1b), or direct entry via protein transduction (1c). Depending on the mode of cellular entry, the vector may become encapsulated in an endosome (2). The vector must escape from the endosome (3a) or it will incur in a lysosomal degradation (3b). The DNA will at some point be subjected to degradation by cytosolic nucleases (4), as it traverses through the cytoplasm to reach the nucleus. Finally, the vector must undergo nuclear transport (5). Once in the nucleus, the DNA may (6a) or may not (6b) need to be uncoated, depending upon the vector used, before it can ultimately be transcribed (7). [Wagstaff, K.M.; Jans, D.A. *Biochem. J.*, **2007**, *406*, 185-202].

1.2 Type of vectors

The major issue that gene therapy is facing, concerns the gene delivery systems, known also as vectors. Most of the vectors used belong to two different categories, namely viral and non-viral vectors.

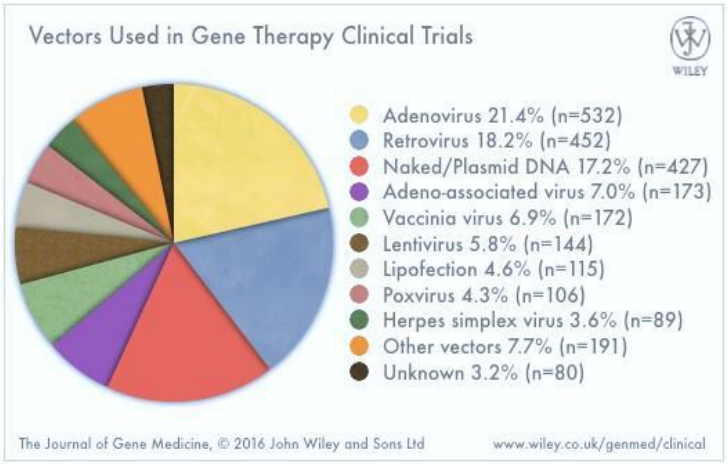

Figure 2. Vectors used in current gene therapy clinical trials [*The journal of Gene Medicine*, **2016**, John Wiley and Sons Ltd, www.wiley.co.uk/genmed/clinical].

1.2.1 Viral vectors

Virus are extensively used as vectors in gene therapy since they have evolved themselves to efficiently gain access to host cells, and facilitate their replication by using the host cellular machineries. They are obtained by introducing a desired gene into the genome of different type of virus, under control of a strong promotor. For gene delivery purposes, they are designed to utilize the viral infection pathway but avoiding the expression of viral genes that could lead to replication and toxicity. This is achieved by deleting or suppressing specific coding region from the viral genome, leaving intact those sequences necessary for functions[13]. After that, viral genome is engineered with

recombinant DNA techniques and transfected in particular cell lines, able to produce the recombinant viral parts (packaging lines). The main advantage of viral vectors is the high transduction while the disadvantages results from the toxicity and immunogenicity. There is also the possibility to produce pathogenic viruses due to the recombination with viruses eventually present into the host, to the risk of insertional mutagenesis and immune response. They can also transport, generally, DNA molecules with limited dimensions and the method is expensive. Currently the studied viruses used in gene therapy are: retrovirus, lentivirus, adenovirus, herpes simplex virus. Each of them presents advantages and disadvantages.

Retroviruses

These viruses were the first to be studied in gene therapy. Their genome is constituted by a single RNA strand containing three essential genes: *gag* coding for the core proteins, *pol* coding for the reverse transcriptase and *env*, coding for the capsid proteins. In addition there are the LTR (Long Terminal Repeat) regions, promoter and enhancer regions and sequences involved with the integration process.

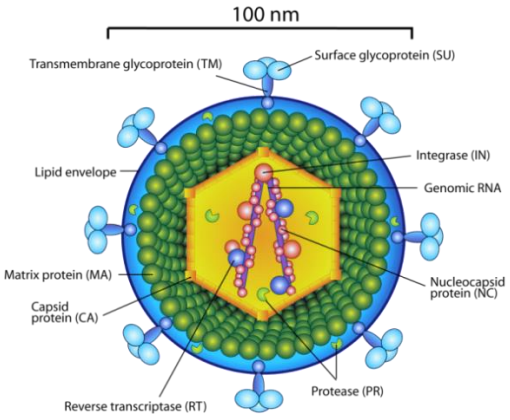

Figure 3. Structure of a retrovirus. [Gifford, R. Retroviral virion structure. https://dx.doi.org/10.6084/m9.figshare.807677.v1, **2013**].

After infection, a reversal transcription process forms a double strand of DNA and is then integrated into the host genome with expression of the viral proteins.

Retroviruses commonly used derived from Murine Leukemia Virus (MLV) that has to be modified: the three essential genes are substituted with the interested gene while the regulatory sequences shall be maintained.

The advantages are:

- ability to transfect efficiently a great variety of cell type;
- integration of the genetic material carried by the vector into the targeted cells genome;
- a little immune response is induced;
- no human pathologies are provoked;
- high transduction efficiency.

The disadvantages are represented by the tumorigenic potential because they can integrate in different places into the host genome; moreover they can be inactivated in vivo, can infect only cells in active replication and are difficult to cultivate.

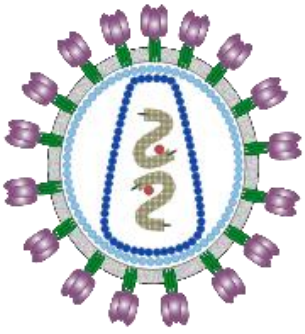

Figure 4. HIV is an example of retrovirus [From: http://www.niaid.nih.gov NIAID, picture of public domain from National Institute of Health and Human Services].

Lentiviruses

Lentiviruses belong to the retrovirus-family but they can infect also non-proliferating cells. This ability make these viruses good candidate to modify the expression of terminally differentiated cells (heart or SNC cells).

The advantages derived by this type of vector are:

- possibility to be administrated in vivo;
- ability to infect both proliferating and resting cells;
- integration of the genetic material carried by the vector into the targeted cells genome.

The disadvantages are the same as for retroviruses.

Adenoviruses

These viruses cause respiratory infections in humans and they present a double strand DNA. Once infected the cell, the adenovirus is not integrated into the genome of the hosting cell, but it duplicates into the nucleus like an episome.

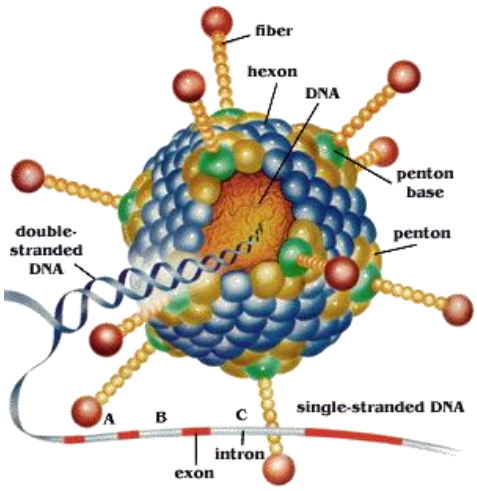

Figure 5. Structure of an adenovirus [Gene Delivery Systems by Andrea Pereyra and Claudia Hereñu, DOI: 10.5772/56869].

The advantages derived by this type of vector are:

- safety because they are not integrated into the host genome;
- easiness of manipulation;
- ability to infect also resting cells;
- ability to carry inserts of high dimensions (36kb).

The disadvantages are related to a high immune response.

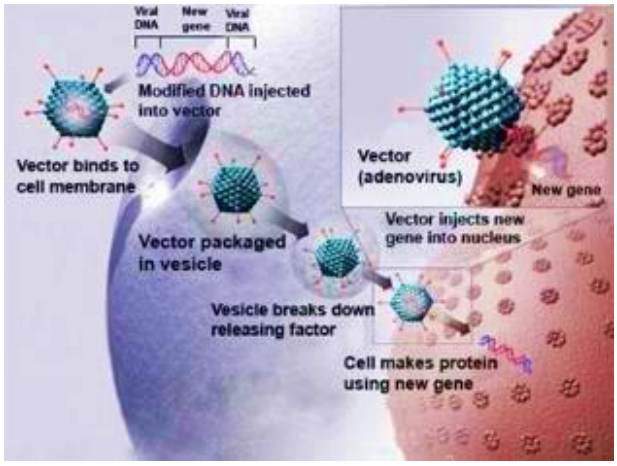

Figure 6. Mechanism of gene delivery mediated by adenovirus vector. [From: http://www.niaid.nih.gov NIAID, picture of public domain from National Institute of Health and Human Services].

Herpes simplex viruses

Thanks to their natural capacity to cause latent infections into neurons, these viruses are used for gene delivery into the CNS (Central Nervous System). The long term expression is obtained by using neuron-specific promotors, activated during the latency period. The genome of Herpes simplex virus is constituted by a DNA double strand containing more than 80 genes, half of which seem not to be essential for cell growth in

cells culture; once eliminated these genes, the insertion of a transgene of a big dimension is possible.

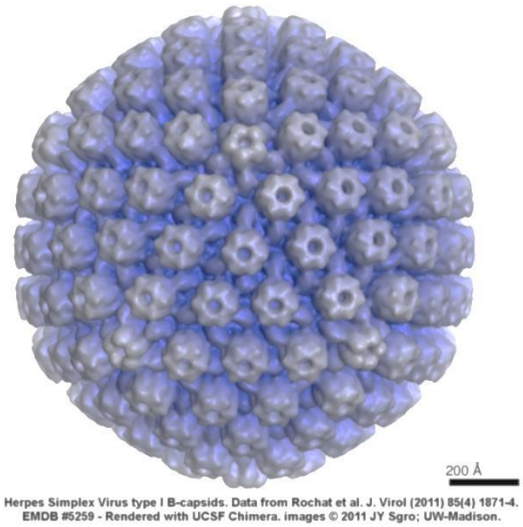

Figure 7. Herpes simplex capsid structure. [Data from Rochart et al., *Virol.*, **2011**, *85*, 1871-1874].

1.2.2 Non-viral vectors

The methodologies adopted to deliver DNA without using a viral vector are: the injection of naked DNA and the transfection using non-viral vectors such as liposomes and cationic polymers. Non-viral vectors are in many cases the preferred system of gene delivery because they show several features of the ideal vector: low immunogenicity and toxicity, easiness to manufacture, stability at room temperature and ease to inject.

Naked DNA

The use of naked DNA is the more simple method to achieve a transfection of genes of big dimensions by injecting the therapeutic gene, linked to a plasmid, directly into the

cell. The disadvantage is represented by the fact that the DNA has to be injected into every single cell. It is clear that this procedure is neither optimal nor efficient.

Liposomes

Liposomes are spherical vesicles formed by a double phospholipid layer. Using cationic liposomes it is possible to form complexes with the DNA that, at neutral pH, presents a negative charge. This complex is then internalized into the cell, mostly by endocytosis. The DNA released into the cytoplasm, enters into the nucleus where it could be expressed.

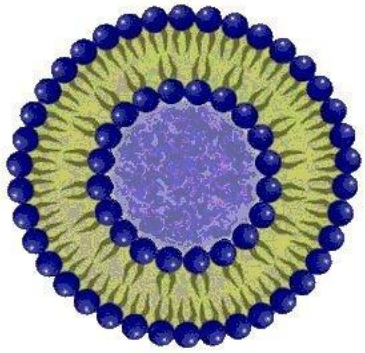

Figure 8. Model of the liposome structure.

Unfortunately this process has a low efficiency because only 0,1% of the DNA conveyed is expressed. To increase this percentage of DNA expression, liposomes can be functionalized with proteins or antibodies in order to increase the efficacy of the procedure minimizing the DNA degradation and facilitating the delivery of this vesicle content.

Cationic polymers

The functional concept is similar to that of liposomes: cationic polymers, in fact, are macromolecules with some positive charges that can interact with negatively charged DNA, causing its condensation. In addition they protect the DNA from chemical and enzymatic aggressions and from ionizing radiations. Like liposomes, these complexes are also internalized into the cell by endocytosis and delivered to the target cells by means of antibodies or other molecules.

1.3 Cationic gemini surfactants

The name "gemini lipid", originally given by Menger and Littau in 1991[14], refers to amphiphilic molecules with two identical simple surfactants linked by a spacer. They consist of at least two hydrophilic polar heads and two hydrophobic tails (Figure 9).

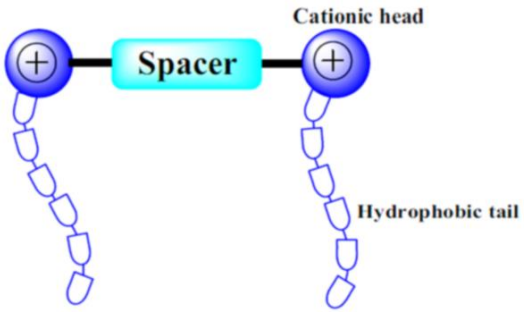

Figure 9. Simplified schematic representation of structure of a cationic gemini surfactant. [Mondal, M.H. et al., *Res. Chem. Intermed*., **2015**, *42*(3), 1913-1928. DOI 10.1007/s11164-015-2125-z].

Cationic lipids constitute the building blocks to compact and encapsulate the DNA into soft nanoparticles, delivered to specific sites by size-dependent passive targeting or by active targeting by means of ligands attached onto their structure to achieve cell surface specificity. Moreover, nanoparticles are able to protect DNA from enzymatic degradation, and their tunable size allows to build nanoparticles large enough to preventing rapid leakage into blood capillaries but small enough for escaping the macrophages of the reticuloendothelial system[15].

In general, due to their structure, gemini lipids binds DNA at lower concentrations if compared to their mono counterparts, leading to lower toxicity. These lipids are capable to condense DNA forming complexes - known as lipoplexes - with smaller size, facilitating the endocytosis of the lipid/DNA complex[15]. The properties of the lipoplexes depend on the aggregate size of the surfactant and the surfactant/DNA charge ratio. It has been also demonstrated that the gene delivery efficiencies of gemini lipids mainly depend on the molecular architectures of the polar head groups, hydrophobic tails, and the nature of backbone as well as spacer[15].

The efficiency of DNA complexation may be improved by addition of helper lipids. This increase the counterion dissociation from the cationic surfactant aggregate, allowing for a more effective interaction of the DNA phosphate groups with the cationic charges[16]. Helper lipids may also have the ability to enhance the lipoplexes stability, they reduce the toxicity of cationic surfactants and also facilitating the fusion with the membrane, thus increasing the transfection efficiency[16].

Neutral lipids, such as the fusogenic zwitterionic phospholipid DOPE [1,2-dioleoyl-sn-glycero-3-phosphoethanolamine-(C18:1,[cis]-9)] is generally included in liposomal formulations as ‘helper lipids’ in order to enhance transfection activity[7]. In fact, DOPE

undergoes protonation and is thought to self-assemble into non-bilayer structures, leading to the disruption of the endosomal bilayer, which results in the rapid release of DNA into the cytoplasm[17-18]. Limitations of cationic lipids include low efficacy owing to poor stability and rapid clearance, as well as the generation of inflammatory or anti-inflammatory responses[19].

The spacer group of gemini surfactants increases the hydrophobicity of the molecule, relative to the monomeric constituent alone, and its length can vary between C2 and C12[20]. Physicochemical properties of gemini surfactants are: high solubilization capacity, unique micelle structure and aggregation behavior, high surface activity[20] and the ability to produce significantly lower tension in comparison to the same molar mass concentration of monomeric surfactants.

Also in this thesis, encouraging results have been obtained in gene delivery by using gemini having two pyridinium groups as polar heads, linked by aliphatic chains of different lengths, in particular when formulated with DOPE. Physicochemical data concerning this new homologous series of gemini surfactants are here collected, with the aim to achieve more information about the interaction of the cationic surfactants with membranes and DNA with the purpose to quantitatively correlate the surfactants structure with their biological activities, particularly with their transfection abilities[21].

1.4 Partially – fluorinated cationic gemini surfactants

Among the peculiar properties of perfluorinated compounds, the most interesting for biomedical applications are the chemical and biological inertness, due to both their high hydrophobic and lipophobic character. These originate mainly from the structure of the fluorine atoms having a larger van der Waals radius and a lower polarizability than the

hydrogen atoms[22-24]. In fact, hydrocarbon chains take the well-known zig-zag structure, while the fluorocarbon chains show a rigid rod-like shape with a period of twist of 13 carbon atoms. In addition, fluorocarbon surfactants are more surface active and stable against acidic, alkaline and oxido-reductive agents and elevated temperatures. These unique properties account for their practical relevance[25]. Several new fluorinated surfactants have been recently synthesized and studied in particular as drug carriers and as gene delivery systems, with very promising results. In fact, they have been proposed to obtain efficient gene expression in those biological fluids containing endogenous surfactants such as, for example, pulmonary surfactants or bile salts, when genes have to be delivered to the respiratory or to the biliar epithelium[26-28]. At the same time, in general, they show low to moderate acute toxicity and low haemolytic activity compared to their hydrogenated analogues[29] and reverse water-in-fluorocarbon emulsions stabilized by a semifluorinated amphiphile have been proposed as drug delivery system for intrapulmonary administration of many drugs (insulin, pain killers, antibiotics, vaccines, etc.)[28].

1.5 Lung surfactant

As previously said, fluorinated surfactants are also proposed as therapeutic surfactants to treat pulmonary diseases determined by the inactivation of the endogenous lung surfactants.

Pulmonary surfactant is a complex mixture of lipids and proteins, synthesized mainly in the lung, which forms a monolayer at the air-alveolus interface.

Epithelial type II cells, present in the alveolar space, synthesize all four surfactant proteins (SP) and surfactant lipids (see next section), which are packaged together in the

lamellar body, a secretory organelle. Following appropriate stimulation, such as birth or a deep breath, the contents of lamellar-body are secreted into the thin aqueous film that covers the alveolar epithelium.

Some surfactant proteins are also synthesized by airway cells but it is not known whether the functions of the surfactant proteins secreted by these cells are similar to those secreted by alveolar cells[30].

The major function of lung surfactant is to lower the surface tension at the alveolar surface to near-zero values during exhalation to facilitate the work of breathing, prevent alveolar collapse[31] at low lung volume and to preserve bronchiolar patency during normal and forced respiration[33]. Lung surfactant has also non-biophysical and immunological functions such as protection of the lungs from microorganisms, infections caused by inhaled particles and injuries [33].

Composition of the lung surfactant

Pulmonary surfactant is approximately composed of 90% lipids and 10% proteins[31] (Figure 10).

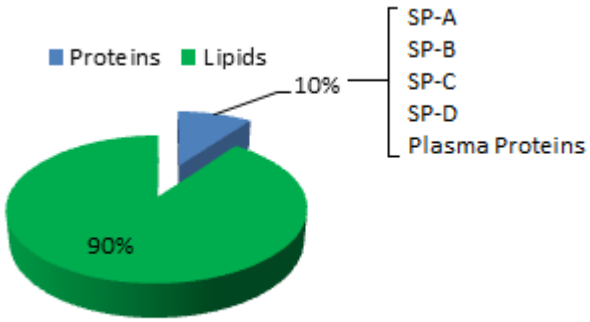

Figure 10. Pulmonary surfactant composition.

The majority of pulmonary surfactant lipids are phospholipids. The lipid monolayer is enriched in dipalmitoylphosphatidylcholine (DPPC), the lipid responsible for generating a near-zero surface tension at the interface during compression[31,32]. This lipid forms a tightly packed monolayer thanks to the two saturated acyl chains, which can generate these low surface tension values without collapsing[31].

The proteins are represented by the four surfactant proteins (SP) SP-A, SP-B, SP-C and SP-D, as well as a large number of other proteins, mostly serum-derived[33]. They can be divided into two groups: SP-B and SP-C are two small hydrophobic proteins, mainly involved in surface activity, while SP-A and SP-D are large hydrophilic proteins (Figure 11). Because of the presence of a collagen-like domain, they are called "collectins"[33].

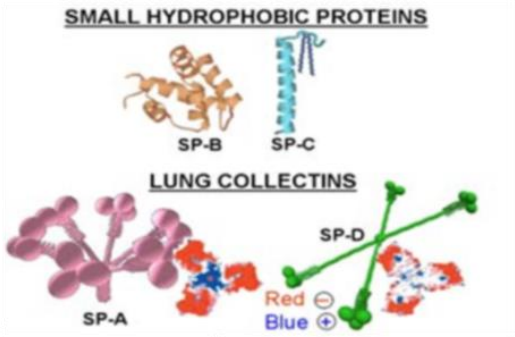

Figure 11. The two groups of surfactant proteins. [From www.ucm.es/info/respira].

Surfactant protein A (**SP-A**) was the first specific protein to be detected. With **SP-D**, it is primarily involved in innate host defence in the alveolar interface[31,33] (Figure 12). They bind and agglutinate pathogens, facilitating the killing of pathogens by alveolar macrophages.

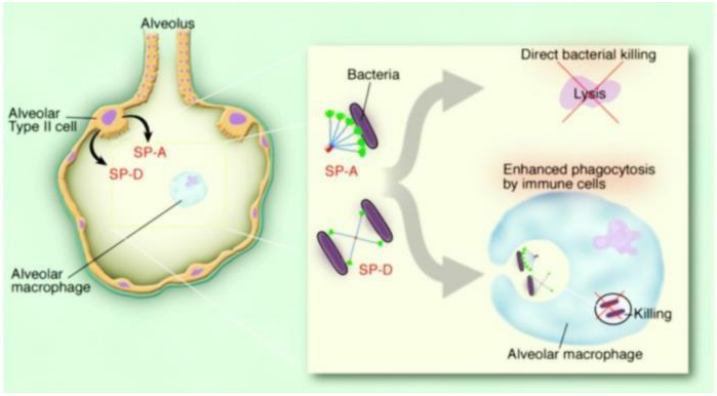

Figure 12. Lung host-defence mechanism. [From Wright, J.R., *The Journal of Clinical Investigation*, **2003**, *15*, http://www.jci.org/articles/view/18650].

The collectins are assembled as trimeric subunits, which multimerize to varying degrees. The active form of SP-A is an octadecamer, formed by six trimers, which forms a bouquet-like structure, while SP-D forms a dodecamer (Figure 13)[31]. SP-A improves surface activity of surfactant, protecting the lung against alveolar collapse.

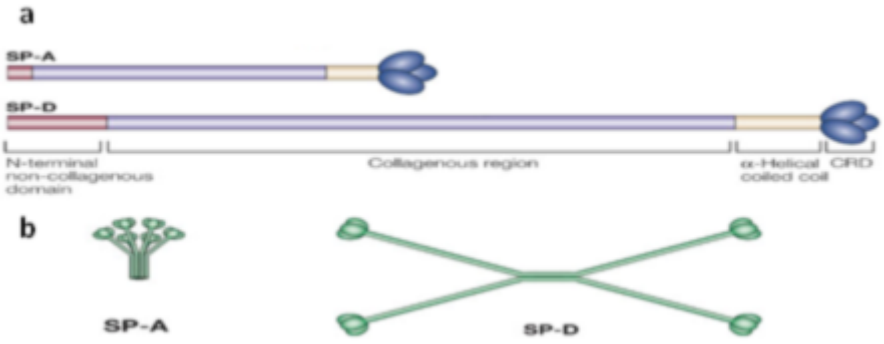

Figure 13. Surfactant protein A (SP-A) and SP-D are members of a family of proteins known as collectins.
a | Collectins have collagen-like amino (N)-terminal regions and C-type (calcium dependent) carbohydrate-recognition domains (CRDs). Collectins consist of structural subunits that are composed of trimeric polypeptide chains, which are identical except for human SP-A.
b | The trimers are assembled into oligomers.
[From Wright, J.R., *Nature Reviews – Immunology*, **2005**, 5, 58-68].

Surfactant protein B (**SP-B**) is an hydrophobic positively charged molecule essential for breathing. It is present in the alveolar space as a dimer, where two SP-B are linked via disulphide bonds. The function of SP-B is to accelerate the formation of a surface active film at the air/water interface, facilitating the re-formation of the layer after compression[33].

Surfactant protein C (**SP-C**) is expressed exclusively by alveolar type II cells. It is an extremely hydrophobic protein mainly involved in the respreading of films from the collapse phase and in the stabilization of the monolayer lipid film and this contribute to film homeostasis[31,34]. In the absence of surfactant, surface tension is extremely high at the end of expiration and the lung tends to collapse. In fact, the presence of surfactants in the fluid film can lower the air/water surface tensions to near-zero values; this ensures that the alveolar space remains open during the whole respiratory cycle for an adequate oxygenation of the blood, and this also reduces the work of breathing. In fact, a well-functioning surfactant keeps the alveoli clear of liquid while maintaining a thin fluid film. A lack of surfactants, on the contrary, leads to the accumulation of oedema fluid in the airspace. The deficiency and/or dysfunction of pulmonary surfactant leads to several severe lung disorders such as Respiratory Distress Syndrome (RDS) and Acute Respiratory Distress Syndrome (ARDS)[35].

Deficiency of lung surfactant in premature infants results in RDS, because their lungs aren't able to make enough surfactant[36], characterized by the alveoli collapse, making hard to the infant to breathe. This leads also to a lack of oxygen that can damage the baby's brain and other organs if proper treatment isn't given on time.

Currently, the clinical treatment for RDS is through surfactant replacement therapy, with the administration of exogenous surfactants, making so important the research in this field.

Dysfunction of lung surfactant is also associated with ARDS that can be caused by direct or indirect lung injury (i.e. aspiration of gastric content, inhaling chemicals, lung transplant, pneumonia, septic shock -infection throughout the body- and trauma) and can affect patients of all ages. This syndrome leads to an accumulation of fluid in alveoli that prevents enough oxygen from passing into the bloodstream. This also makes the lungs heavy and stiff, which decreases the lungs' ability to expand.

During the acute phase, the influx of protein-rich edema fluid into the air spaces, as a consequence of increased permeability of the alveolar–capillary barrier, inactivate the lung surfactants (Figure 14).

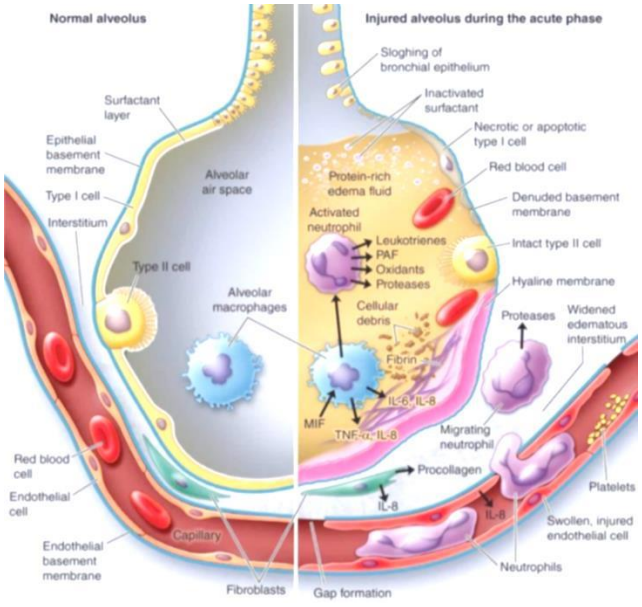

Figure 14. Comparison between normal and injured alveoli. [From Ware, L.B.; Matthay; M.A. Medical progress: the acute respiratory distress syndrome *N. Engl. J. Med.*, **2000**, *342*,1339].

The oxygen administration is not enough to reach an optimum level of oxygen in the blood and surfactant replacement therapy applied to ARDS is less successful than that in RDS. A fundamental understanding of lung surfactant function can lead to a more effective and optimal therapy to treat lung disorders[35].

1.6 Use of the Langmuir–Blodgett trough to study the surfactant monolayer

Cell membrane provides a partially permeable barrier, formed mostly of lipids and proteins that regulate the flux of material in and out of the cell[37].

Membrane lipids are amphiphilic molecules composed by a hydrophilic head group and a hydrophobic tail. In aqueous environment they assemble themselves with the tails interacting with each other in the interior and the heads orientated towards the water molecules. The structure of the cell membrane acts as a barrier to water soluble molecules and can incorporate membrane proteins which carry out many important physiological functions for cell activity.

Because the cell membrane is so complex, preliminary studies, as in the case of Langmuir-Blodgett experiments, are conducted in biomimetic model systems mainly obtained by synthetic or natural phospholipids which form structures with characteristics comparable to these of natural cell membranes.

Langmuir-Blodgett trough

Langmuir Troughs are used for Langmuir film fabrication and characterization, while Langmuir-Blodgett technology enables the deposition of single- or multimolecular layers from a liquid surface onto a solid substrate.

A Langmuir film can be defined as an insoluble spread monolayer (a single-molecule thick film or layer of closely packed atoms or molecules at an interface, Figure 15**a**) of atoms or molecules floating at the liquid-gas interface. Langmuir-Blodgett (LB) films are formed by the deposition of one or several Langmuir films onto a solid surface by vertical dipping of the solid substrate from the air phase into the water sub-phase, or vice versa (Figure 15**b**). The technique is named because of the studies of Irving Langmuir and Katharine Blodgett, researchers at the General Electric Company in the first half of the twentieth century. While Langmuir, during his research, developed several new techniques that are still used to investigate the monomolecular films, Katharine Blodgett refined the method of transferring the monolayer present at the interface, onto solid supports.

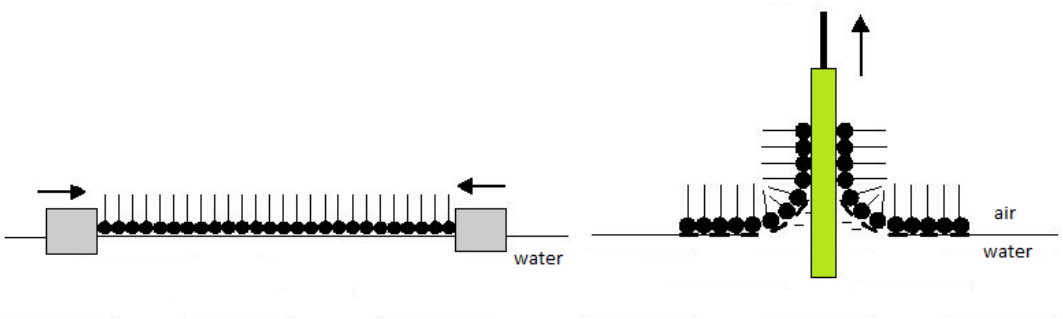

Figure 15. a | Langmuir film and **b** | Langmuir-Blodgett depositions.

Amphiphilic monolayers are the most common Langmuir films able to create a monolayer in a water insoluble solvent. When the amphiphile solution is deposited on the water surface, the solution spreads rapidly to cover the entire available area. A monolayer forms at the air-water interface (the Langmuir film) when the solvent evaporates. The movable barriers, located at the interface, then compress the monolayer until maximum packing density is reached. When molecules possess hydrophobic and

hydrophilic parts, they orientate themselves in a predictable way. When surfactant concentration is less than critical micellar concentration (cmc), the molecules arrange themselves as shown in Figure 16: the exposure the hydrophobic tails to air is favoured over that to water while, since the heads are hydrophilic, their water interaction is more favourable. The overall effect is the reduction in the surface tension of water (or equally, surface energy).

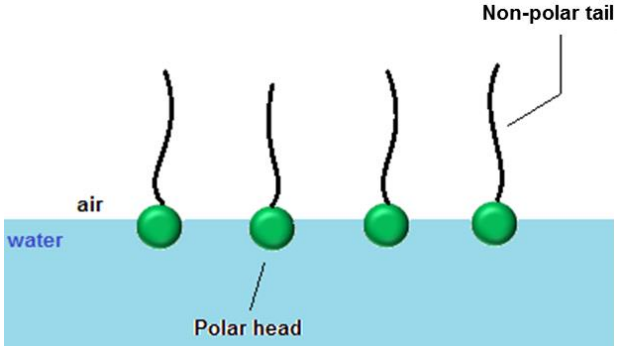

Figure 16. Surfactant molecules arranged on the air–water interface.

It can be assumed that, in the case of concentration lower than cmc, the random motion on the water–air interface of the surfactant molecules is similar to that of ideal-gas molecules enclosed in a container. The corresponding thermodynamic variables for the surfactant system are, surface pressure (π), surface area (A) and number of surfactant molecules (N): the surface pressure, as well as the density of surfactant molecule, increases upon reducing the surface. The surface pressure is obtained by measuring surface tension using the Wilhelmy plate method (Figure 17).

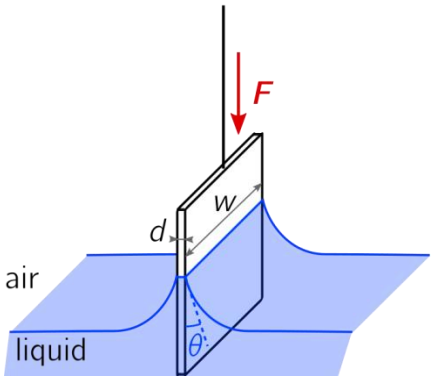

Figure 17. Wilhelmy plate at the air-water interface.
[Image of public domain from en.wikipedia.org].

With this method is determined the force due to surface tension on a plate suspended and partially immersed in the sub-phase. This force is then converted into surface tension (γ, mN/m) with the help of the dimensions of the plate, made often from filter paper, using the Wilhelmy equation:

$$\gamma = \frac{F}{l\cos(\theta)}$$

where l ($2w + 2d$) is the wetted perimeter of the Wilhelmy plate and θ is the contact angle between the liquid phase and the plate.

Surface pressure-area isotherm, is built by measuring the surface pressure at constant temperature, as a function of the available area for each molecule by compressing the film at a constant rate while continuously monitoring the surface pressure.

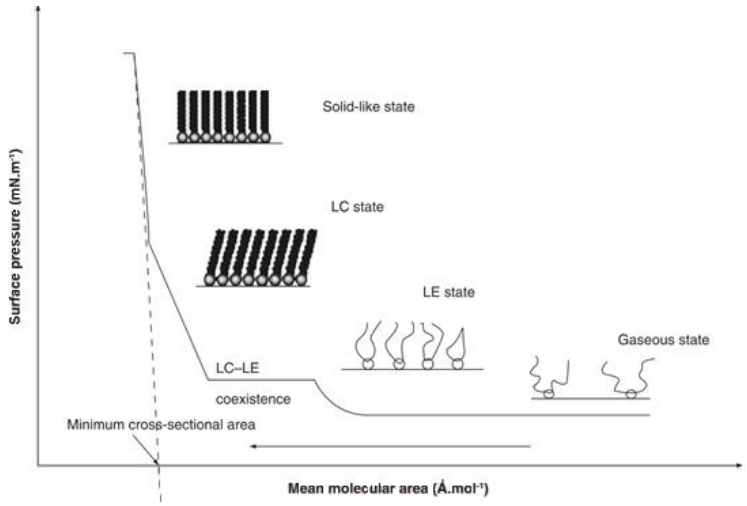

Figure 18. Theoretical π-A isotherm of a Langmuir film and molecules obtained by compression at an air/water interface. LC: Liquid Condensed state; LE: Liquid Expanded phase. Image from Ref.[12].

The phase behavior of the monolayer is mainly determined by the physical and chemical properties of the amphiphile, the sub-phase temperature and the sub-phase composition. A simple terminology used to classify different monolayer phases of fatty acids was proposed by W. D. Harkins in 1952. The monolayers mostly exist in the gaseous state that, on compression, can undergo a phase transition to the liquid-expanded state (LE). Increasing the surface pressure, this phase undergoes a transition to the liquid-condensed state (LC), and at even higher densities finally the solid (S) state is reached (Figure 18). If the monolayer is further compressed after reaching the S state the monolayer will collapse into three-dimensional structures, that causes a rapid decrease in the surface pressure. There are also many other critical points in a π-A-isotherm, such as the molecular area at which an increase in the surface pressure is observed and the surface pressures at which phase transitions occur.

2. EXPERIMENTAL SECTION

2.1 Materials

- *Hydrogenated gemini surfactants*

The bispyridinium cationic gemini surfactants under study were synthesized by the research group I'm working with, as described in Ref.[38] for the dodecyl compounds. The compounds having chloride as a counterion, are named P*m*-*n*, where *m* indicates the number of carbon atoms of the alkyl chain and *n* the spacer length and P stands for bispyridinium. The compounds studied are 1,1'-dihexadecyl-2,2'-trimethylenebispyridinium dichloride (P16-3), 1,1'-dihexadecyl-2,2'-etramethylenebispyridinium dichloride (P16-4), 1,1'-dihexadecyl-2,2'-ctamethylenebispyridinium dichloride (P16-8), and 1,1'-dihexadecyl-2,2'-dodecamethylenebispyridinium dichloride (P16-12). The general structure of these compounds is shown in Figure 19. To check the purity NMR, elemental analysis, and thin-layer chromatography (TLC) on a silica gel plate (Merck) using the BAW eluent (butanol:acetic acid:water = 4:1:5, organic phase), have been employed.

The solutions were prepared by weight using freshly boiled bidistilled water and stored under nitrogen, and their concentrations are expressed as molality, *m* (mol kg^{-1}).

1,2-Dipalmitoyl-sn-glycero-3-phosphatidylcholine (DPPC) was purchased from Sigma-Aldrich, Steinheim, Germany. The lipid purity was greater than 99%.

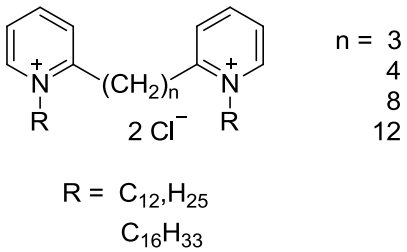

Figure 19. General structure of the hydrogenated P12-*n* and P16-*n* gemini where *n* is the number of carbon atoms in the spacer.

- *Fluorinated gemini surfactants*

The synthesis of the fluorinated compounds is reported in detail in Ref.[39]. In the following the IUPAC names of the compounds studied and in brackets the names in short by which they will be referred in the thesis, are shown: 1,1'-Bis(3,3,4,4,5,5,6,6,7,7,8,8,8-tridecafluorooctyl)-2,2′-trimethylenebispyridinium dichloride (FGP3); 1,1'- Bis(3,3,4,4,5,5,6,6,7,7,8,8,8-tridecafluorooctyl)-2,2′-tetramethylenebispyridinium dichloride (FGP4); 1,1'- Bis(3,3,4,4,5,5,6,6,7,7,8,8,8-tridecafluorooctyl)-2,2′-octamethylenebispyridinium dichloride (FGP8); 1,1'-Bis(3,3,4,4,5,5,6,6,7,7,8,8,8-tridecafluorooctyl)-2,2′-dodecamethylenebispyridinium dichloride (FGP12). The corresponding dimethanesulfonate compounds are named as FGPS*n*. The compounds with chlorides as counterions were obtained by ion exchange, after having synthesized the corresponding ditrifluoromethanesulfonate. Purity was checked by NMR, elemental analysis and TLC: eluent BAW (butanol:acetic acid:water = 4:1:5-organic phase) on silica gel plate (Merck). Their general structure is shown in Figure 20.

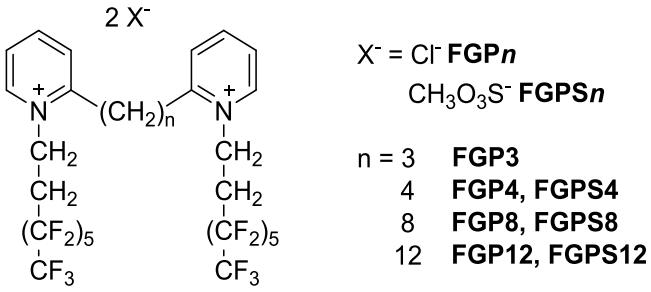

Figure 20. General structure of the fluorinated FGP*n* and FGPS*n* gemini compounds, where *n* is the number of carbon atoms in the spacer.

- *Dimyristoyl-sn-glycero-3-phosphatidylcholine (DMPC) C14:0*

1,2-Dimyristoyl-sn-glycero-3-phosphocholine (DMPC) is a synthetic phospholipid used in liposomes and lipid bilayers for the study of biological membranes, providing new evidence of the penetration of these proteins into the lipid structures.

It is a typical phospholipid forming highly ordered monolayers. The DMPC molecules can be spread, compressed and highly oriented at the air/water interface at various lateral surface pressures to form monolayers of close-packed polar headgroups within the interfacial water having the hydrocarbon chains oriented into the air phase.

DMPC exhibits clear transitions between gel, rippled gel and liquid crystalline phases in water when the lipid sample is pure and it has been widely used as a biomimetic membrane[40].

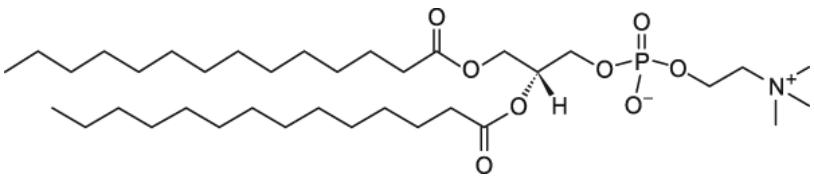

Figure 21. DMPC structure.

- *L-α-1,2-Dipalmitoyl-sn-glycero-3-phosphocholine (DPPC) C16:0*

Dipalmitoylphosphocholine (DPPC) is a fully saturated zwitterionic phospholipid able to pack at different bilayer states corresponding to homogeneous monolayer phases. It is prominent in the lipid bilayer making up the cell membrane and is also a major constituent of lung surfactant. DPPC is also found as a main component of plasma and organelle membranes and represent a large fraction in pulmonary surfactant films.

The relevant monolayer phases are (a) liquid-expanded (LE), which is a low-density fluid where the acyl chains are in a disordered state, (b) liquid-condensed (LC), which is formed upon lateral compression with the acyl chains ordered parallel, and (c) solid (S), where the ordered chains become perpendicular to the monolayer plane in a hexagonal crystalline arrangement. LE is the structural analogue of the bilayer fluid state characteristic of the fluid matrix of biological membranes, and LC is of the gel state typical of lipid rafts enriched in saturated chains.

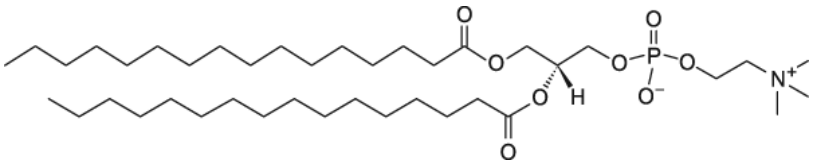

Figure 22. DPPC structure.

- *DNA preparation and storage*

Plasmid DNA was purified through caesium chloride gradient centrifugation.

A stock solution of the plasmid 0.7 μM was prepared in MilliQ water (Millipore Corp., Burlington, MA) and stored at -20° C.

Linearized plasmid DNA (pEGFP-C1) was obtained by cutting with EcoRI restriction enzyme (Roche), column purified (Genomed) and alcohol precipitated. The linearized plasmid DNA pellet was then washed with 70% of ethanol, air dried and dissolved in distilled water at a final concentration of 1 μg/μl.

- *Cell culture*

The human rhabdomyosarcoma cell line RD-4, obtained from David Derse, National Cancer Institute, Frederick, Maryland, is easy to handle and fast growing.

Cells were maintained as a monolayer using growth medium containing 90% Dulbecco's modified Eagle's medium (DMEM), 10% fetal bovine serum (FBS), 2 mM L-glutamine, 100 IU/ml penicillin, 10 μg/ml streptomycin. Cells were subcultured to a fresh culture vessel when growth reached 70-90% confluence (i.e. every 3-5 days) and incubated at 37° C in a humidified atmosphere of 95% air/5% CO_2.

2.2 Methods

2.2.1 Solution thermodynamics

- *Dilution enthalpies measurements*

Enthalpies of dilution were measured by means of the Thermometric TAM (Thermometric) microcalorimeter, equipped with 221 Nano Amplifier, at 298 K, by using the flow mixing cell. The freshly prepared surfactant solutions, kept before injection at the experimental temperature by means of a Heto cryothermostatic bath, were diluted into the "mixing" measuring cell of the microcalorimeter in a ratio 1:1 by using CO_2-free water. The solutions and the water were injected by means of a Gilson peristaltic pump, Minipuls 2, and their flows were determined by weight. For the dilution enthalpies measurements, the solutions were prepared by weight using freshly boiled bi-distilled water, stored under nitrogen, and solution concentrations were expressed as molality, m (mol kg^{-1}).

- *Density and sound velocity measurements*

Density and sound velocity of the solutions as a function of m were obtained by a Paar DSA 5000, an oscillating U-tube meter, able to measure density (±0.000001 g cm^{-3}) and sound velocity (±0.1 m s^{-1}) to the highest accuracy in wide viscosity and temperature ranges. Based on an additional measuring cell made of stainless steel and high resolution electronics, the sound velocity of the filled in sample can be determined accurately. Both measuring cells are temperature controlled using a built-in solid state thermostat and two integrated Pt 100 platinum thermometers (±0.001°C). The instrument was calibrated by water and dry air.

- *Surface tension measurements*

The surface tension, γ, was measured by using a Lauda (TE1C/3) digital tensiometer, equipped with the Du Noüy ring (Pt/Ir alloy (80/20), circumference: 60 ± 0.2 mm, wire diameter 0.4 mm, weight: 1.6 g). Sample temperature was maintained at 25.0 ± 0.1°C by using a circulating water thermostatic bath (ISCO GTR 2000 IIx). The data were corrected according to the Zuidema and Waters method[41]. The instrument was calibrated against double-distilled (and previously deionised) water, equilibrated against atmospheric CO_2, each time measurements were done. Because the dicationic gemini surfactants adsorb onto negatively charged glass surfaces, all glassware was thoroughly soaked with the solution to be measured; soaking solutions were discarded. The fresh solution was aged for several hours before surface tension measurement. Sets of measurements were taken at 15 min intervals until no significant change occurred, using a very slow ring rising velocity. These tactics ensure that the ring is completely wetted.

Standard deviation of the surface tension measurements is less than 0.15 mN/m. The absence of a minimum in the γ vs log c (where c is the concentration expressed in mol/L) plot in the post-cmc region showed that there was very little or no surface active impurity present in the final products.

2.2.2 Structural characterization

- *Atomic Force Microscopy (AFM) imaging*

Plasmid DNA was diluted to a final concentration of 0.5 nM in deposition buffer (4 mM Hepes, 10 mM NaCl, 2 mM $MgCl_2$, pH 7.4) either in the absence or in the presence of P16-*n* or FGP*n* (*n* = 3, 4, 8, and 12) in the same DNA:surfactant ratio used in the transient transfection assay experiments, while DOPE was dissolved in ethanol before addition. The mixture was incubated at room temperature for 5 minutes, then a 20 μl droplet was deposited for one minute onto freshly-cleaved ruby mica (Ted Pella, Redding, CA). The mica disk was rinsed with Milli-Q water and dried with a weak stream of nitrogen.

The dried sample was used for AFM imaging with a Nanoscope IIIA Microscope (Digital Instruments Inc. Santa Barbara, CA) operating in tapping mode. Commercial diving board silicon cantilevers (NSC-15 Micromash Corp., Estonia) were used. Images of 512×512 pixels were collected with a scan size of 2 μm at a scan rate of 3-4 lines per second and were flattened after recording using Nanoscope software.

2.2.3 Biochemical characterization

- *Electrophoresis Mobility Shift Assay (EMSA)*

Binding reactions were performed in a final volume of 14 μl, obtained by adding to 10 μl of 20 mM Tris/HCl pH 8, 1 μl of plasmid (1 μg of pEGFP-C1) and 3 μl of P16-n or FG*n* with *n* = 3, 4, 8, 12 at different final concentrations, ranging from 6.5 to 200 μM. Binding reaction was left to take place at room temperature for 1 hour, 5 μl of 1 g/ml in H_2O of glycerol was added to each reaction mixture and loaded on a TA (40 mM Tris-Acetate) 1% agarose gel. The gel was run for 2.5 hours in TA buffer at 10 V/cm, EDTA was omitted from the buffers because it competes with DNA in the reaction.

- *Transient transfection assay*

Transfections were performed in 6 well plates, when cells were 80% confluent (approximately 3×10^5 cells) on the day of transfection. 3 μg of plasmid, gemini surfactant were added to 1 ml of serum-free medium at final concentration of 15 μM, mixed rapidly and incubated at room temperature for 20 minutes. Each mixture was carefully added to the cells following the aspiration of the culture medium from the cells. Lipoplex formulations were done by adding 1,2-dioleyl-sn-glycero-3-phosphoethanolamine (DOPE) to the plasmid-surfactant mixture at a surfactant:DOPE molar ratio of 1:2 where the surfactant concentration was kept to 15 μM. GenePORTER® transfection reagent, a neutral lipid transfection reagent was used as positive transfection control. Mixture and cells were incubated at 37° C in a humidified atmosphere of 95% air/5% CO_2 for 5 hours. Finally, 1 ml of medium containing 20% of FBS was added to each transfected well and left to incubate for 72 hours.

Transfected cells were observed under fluorescence microscope for EGFP (enhanced green fluorescent protein) expression. Five random fields were examined from each well and each experiment was repeated three times. Statistical differences among treatments were calculated with Student's test and multi factorial ANOVA.

- *MTT proliferation assay*

RD-4 cells were plated on 96-well plates (3000 cells per well) and different concentrations (2.5, 5, 10, 20, and 40 μM) of FGP*n* (*n* = 3, 4, 8, 12) were added. The same experiments were carried out also by adding DOPE at a surfactant:DOPE ratio of 1:2. At 48 hours post treatment, the relative number of metabolically active cells was assessed by reduction of 3-[4,5-dimethylthiazol-2-yl]-2,5-diphenyl tetrazolium bromide (MTT)**.** Briefly, after 48 hours of treatments, 20 μl of MTT (5 mg/ml) were added to the culture for 4 h. Then, after addition of 100 μl of solubilization solution (10% SDS in HCl 0.01 M) cells were incubated at 37 °C overnight. Specific optical density was measured at 540 nm, using 690 nm as reference wavelength in microreader SLT-Lab (Salzburg, Austria). For the proliferation studies, each experiment was repeated three times and each treatment was performed with eight replicates. Statistical differences among treatments were calculated by Student's test and multi factorial ANOVA.

2.2.4 Langmuir – Blodgett study

- *Langmuir–Blodgett trough*

The instruments used were the NIMA Langmuir Blodgett trough (NIMA Technology, Coventry, UK) and the Riegler and Kirstein (Riegler & Kirstein GmbH, Potsdam, Germany) minitrough, the use of which was kindly granted to me by ICS – Institute Charles Sadron (Strasbourg, France), under the supervision of Professor Marie Pierre Krafft, a leading expert in the field of fluorinated materials. This experiments were performed during three months of the mandatory abroad-period for PhD students.

The two instruments were both equipped with two movable barriers and the surface pressure was measured using the Wilhelmy plate method.

The NIMA Langmuir trough was enclosed in a laminar flow cabinet to avoid contamination of the air, while the R&K minitrough was enclosed in a gas-tight box (Figure 23**a** and **b** respectively). This box was flushed either with pure N_2 or with N_2 saturated with a perfluorocarbon (FC): the perfluorohexane (PFH 98+%, Alfa Aesar). In the latter case, N_2 was allowed to bubble at room temperature trough the liquid FC putted into three different vials, the optimal number of vials to obtain a satisfied N_2 saturation, before being flushed into the gas-tight box.

a |

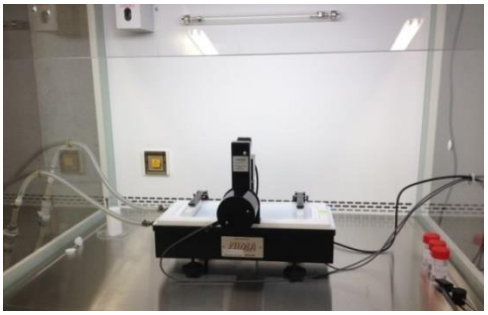

b |

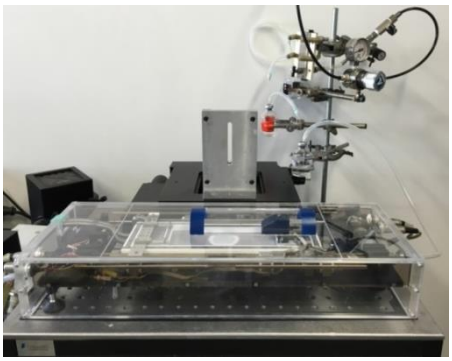

Figure 23. **a** | the NIMA Langmuir-Blodgett trough and **b** | the Riegler & Kirstein mini-trough.

The study was conducted only on FGP*n* gemini surfactants. The samples were prepared in chloroform ($CHCl_3$, Carlo Erba) in order to obtain solution that allows the surfactants staying at the water/air interface. The surface pressure was measured using the Wilhelmy plate method. 25 µL of gemini solution (0,3 mmol L^{-1}) were spread on the water surface and 10 min were allowed for solvent evaporation. Temperature was regulated at ± 0.5 °C and compression speed was kept at 5 cm^2 min^{-1} for all experiments. Each experiment was repeated at least 3 times. Experimental errors were ± 0.5 mN m^{-1} on the surface pressure values and reproducibility on the molecular area values was ± 0.5 $Å^2$.

- *Langmuir-Blodgett Films for the layer deposition and AFM imaging.*

The films were compressed up to the desired surface pressure and then transferred, at constant pressure, onto a silicon wafer previously treated with plasma cleaner, using the Langmuir Blodgett technique (lift speed: 2 mm/min). The transferred films were analysed with a Multimode AFM (NanoScope IV Controler, Digital Instruments, Santa Barbara, CA) working in tapping mode. The cantilever (Olympus) was fitted with a 3-10 nm tip. Several positions were scanned on the wafer for each sample. The error on measurements along the z axis was estimated at ± 0.5 nm.

3. RESULTS

RESULTS

This study started from the investigation of the chemical-physical properties of the gemini compounds.

Simplified models are required to treat and interpret thermodynamic properties of surfactant solutions but in principle, more reliable thermodynamic parameters can be obtained through direct studies.

Solution thermodynamics: binary systems

The fundamental thermodynamic property in a system is nearly always the total property, such as the volume of a system. However, especially in the case of dilute solutions, solute-solvent and solute-solute interactions will cause relatively small changes in the total property and experiments are usually designed to measure directly these small differences. Theoretical models will proceed in the same way; they will usually be derived for the total thermodynamic property and then rearranged to be in the same mathematical form as the expression used to represent the experimental data.

Surfactant system are usually dilute solutions and the most convenient thermodynamic relations in such cases are apparent and partial molar quantities. In binary system composed of n_1 moles of the solvent and n_2 moles of the solute, the partial molar quantities of both components are defined respectively by:

$$Y_1 = \left(\frac{\delta Y}{\delta n_1}\right)_{T,P,n_2} \qquad Y_2 = \left(\frac{\delta Y}{\delta n_2}\right)_{T,P,n_1} \tag{1}$$

where Y is the total property: Gibbs free energy G, enthalpy H, heat capacity at constant pressure C_p, volume V, expansibility E and isothermal compressibility K. For dilute solutions ($n_2 \rightarrow 0$) the interesting function is Y_2 since all the interactions in the system

will then be attributed to a small number of moles. The corresponding Y_1 then tends to the molar quantity Y^*_1.

The partial molar quantities are correlated by Euler's theorem,

$$Y = n_1 Y_1 + n_2 Y_2 \quad (2)$$

and by Gibbs-Duhem relation,

$$n_1 dY_1 + n_2 dY_2 = 0 \quad (3)$$

at constant temperature and pressure. This implies that if one quantity has been measured as a function of concentration, the second can be calculated from the first. This is especially important for colligative properties, which measure the activity of the solvent and from which the activity coefficient of the solute can be derived.

The most convenient concentration scale for experimental measurements on dilute solutions is molality (m = number of moles of solute per kilogram of solvent or 55.51 mol of water). Since the number of moles of solvent is fixed, then

$$Y_2 = \left(\frac{\partial Y}{\partial m}\right)_{T,P} \quad (4)$$

Except in a few cases, partial molar quantities cannot conveniently be measured directly, and experiments are designed to obtain finite differences in the total properties. It is therefore necessary to introduce apparent molar quantities,

$$Y_{2,\phi} = \frac{Y - n_1 Y^*_1}{n_2} = \frac{Y - 55.51 Y^*_1}{m} \quad (5)$$

The partial molar quantities can readily be derived from $Y_{2,\phi}$ using equations (1) and (5),

$$Y_2 = Y_{2,\phi} + m\left(\frac{\partial Y_{2,\phi}}{\partial m}\right)_{T,P} \quad (6)$$

It is convenient to rewrite equation (6) in the form:

$$Y_2 = \frac{d(Y_{2,\phi} m)}{dm} \cong \frac{\Delta(Y_{2,\phi} m)}{\Delta m} \quad (7)$$

for constant temperature and pressure. Therefore, Y_2 can be calculated if $Y_{2,\Phi}$ has been measured at close enough molality intervals. On the other hand, theoretical models can be expressed mathematically directly in term of apparent or partial molar quantities.

Solute-solvent interactions are usually discussed with reference to standard thermodynamic quantities. For all properties except free energies and entropies, the standard state for the solute is infinite dilution (Y_2^θ). It follows directly from Eq. (6) that

$$\lim_{m \to 0} Y_{2,\phi} = Y_2^\theta \quad (8)$$

These standard values depend on the intrinsic contribution of the molecule in addition to the solute-solvent interactions. It is therefore useful, and in some cases essential (e.g.

enthalpies), to eliminate or at least reduce the intrinsic contribution. This is done by subtracting from Y_2^{θ} some reference quantity: gas-phase molar value, molar value of the pure liquid or solid solute, Y_2^*, or some calculated intrinsic value, Y_2(in). For free energies the standard state is the hypothetical ideal 1 *m* solution if the molality scale is used.

Solute-solute interactions are obtained from the concentration dependence of the thermodynamic quantities. Usually, a virial expansion is used for partial or apparent molar quantities. For non-ionic solute,

$$Y_{2\phi,} = Y_2^{\theta} + B_Y m + C_Y m^2 + \cdots \quad (9)$$

The parameters B_Y, C_Y, … are equivalent to second, third and higher virial coefficients. From equation (7) it is straightforward to transform equation (9) into an equivalent form for Y_2. For ionic systems, long-range coulombic interactions are involved which have a more complex concentration dependence. For dilute solutions it is often sufficient to introduce a term A_Y, corresponding to the limiting slope of the Debye-Hückel law and, if necessary, terms in $m^{3/2}$, etc.,

$$Y_{2,\phi} = Y_2^{\theta} + A_Y m^{1/2} + B_Y m + \cdots \quad (10)$$

For aqueous solutions the parameter A_Y has been calculated for various quantities as a function of temperature. If a large concentration range is covered, more extended forms of Debye-Hückel theory may be preferable. Also, if added electrolytes are present, expressions involving ionic strength will be required.[42]

- *Dilution enthalpies measurements apparent and partial molar enthalpies*

The thermodynamic data of the solution of fluorinated surfactants under investigation are given in terms of apparent and partial molar quantities of the solute assuming infinite dilution as the reference state, as usual in solution thermodynamics. Apparent and partial molar quantities were obtained from the experimental data using methods stated in detail in Ref.[42-44].

With reference to the state of infinite dilution, the molar enthalpy of dilution, ΔH_d, is given by:

$$\Delta H_d = L_{\Phi,f} - L_{\Phi,I} \quad (11)$$

where L_Φ is the apparent relative molar enthalpy and the indexes *f* and *i* stand for the final (after dilution) and initial (before dilution) concentrations, respectively[44].

For ionic surfactant in the premicellar region, the apparent relative molar enthalpy can be expressed by means of a polynomial of $m^{½}$. Stopping the serial expansion at the third term we obtain:

$$L_\Phi = A_L m^{½} + B_L m + C_L m^{3/2} \quad (12)$$

where A_L is the limiting Debye-Hückel slope for relative enthalpies accounting for the long range electrostatic solute-solute interactions. Parameters B_L and C_L are obtained from the experimental points in the premicellar region by a least squares curve fitting.

In the micellar region, the apparent molar enthalpies are evaluated by means of equation (11) and, when a value of L_Φ *vs.* *m* not experimentally measured is needed, by graphical interpolation. The partial molar enthalpies L_2 are determined by drawing the best curve for the apparent molar enthalpies *vs.* *m* and then by calculating the partial molar

quantities as $\Delta(mL_\Phi)/\Delta m$ from points interpolated at regular intervals.

The curves of apparent and partial molar enthalpies *vs.* *m* for the compounds under investigation are shown in Figure 24 and 25, respectively for the hydrogenated gemini[44]. It has been measured in a previously work by the research group I'm in, the dilution enthalpies of the didodecyl compounds (P12-*n*) because the dihexadecyl compounds have a cmc too low to allow for an accurate determination in the premicellar region[44]. Figure 26 and 27 also report the apparent and partial molar enthalpies *vs.* *m* for the highly fluorinated analogues with chlorine as counterion[45] while Figures 28 and 29 report the comparison of the same curves of FGP*n* with two different counterions[46].

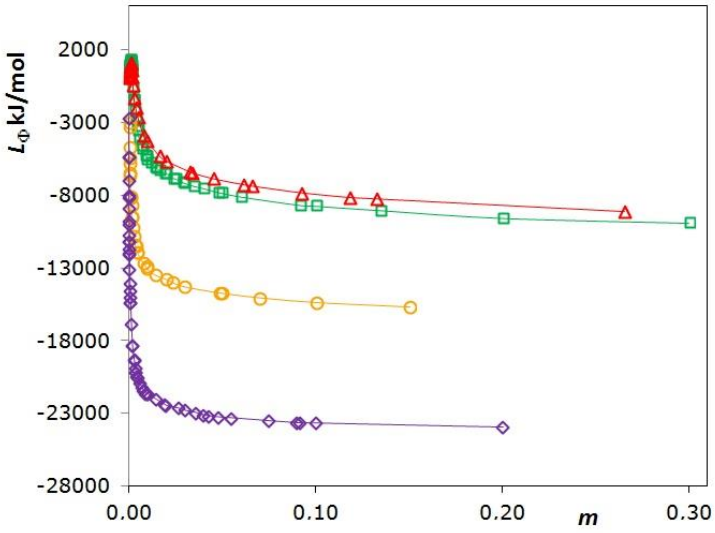

Figure 24. Apparent molar relative enthalpies of P12-3 (empty squares), P12-4 (empty tringles), P12-8 (empty circles), P12-12 (full diamonds) as a function of surfactant molality, *m*. Ref.[44].

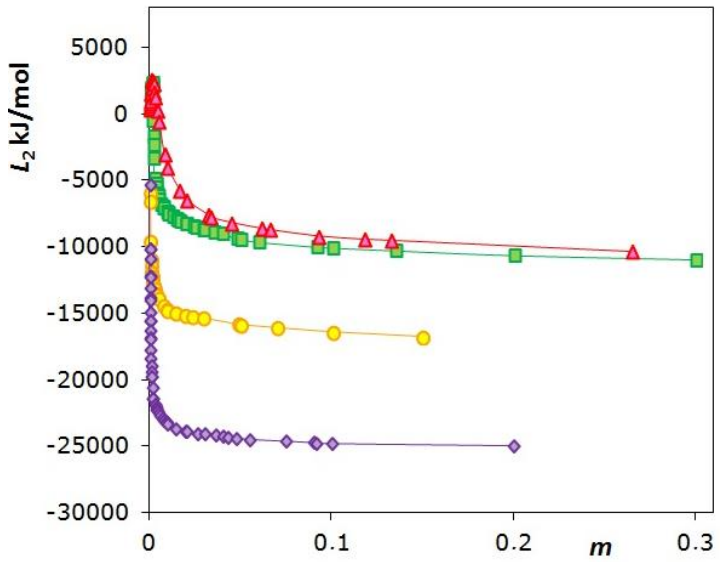

Figure 25. Partial molar relative enthalpies of P12-3 (full squares), P12-4 (full tringles), P12-8 (full circles), P12-12 (full diamonds) as a function of surfactant molality, *m*. Ref.[44].

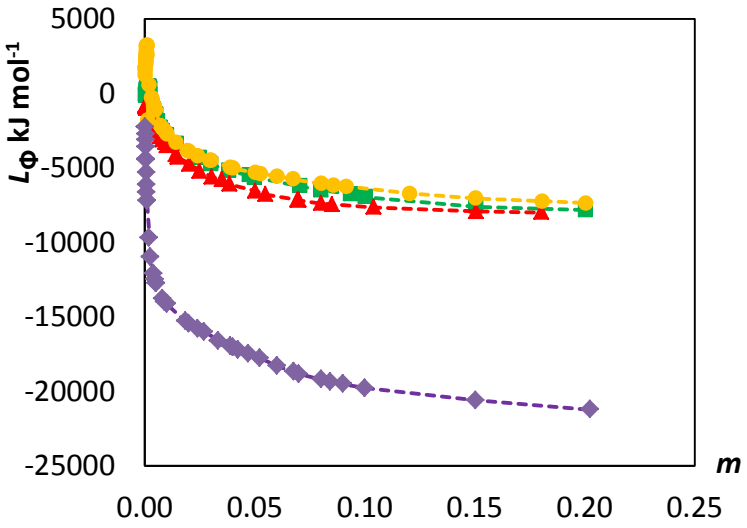

Figure 26. Apparent molar relative enthalpies of FGP3 (full squares), FGP4 (full tringles), FGP8 (full circles), FGP12 (full diamonds) as a function of surfactant molality, *m*. Ref.[45].

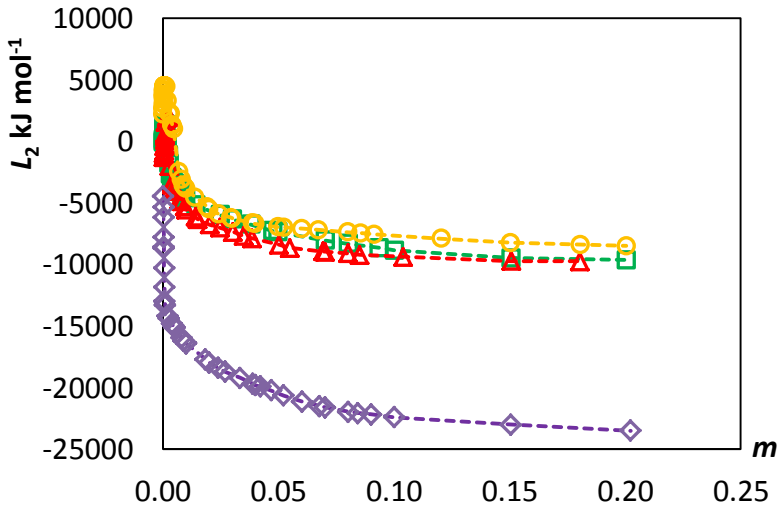

Figure 27. Partial molar relative enthalpies of FGP3 (empty squares), FGP4 (empty tringles), FGP8 (empty circles), FGP12 (empty diamonds) as a function of surfactant molality, *m*. Ref.[45].

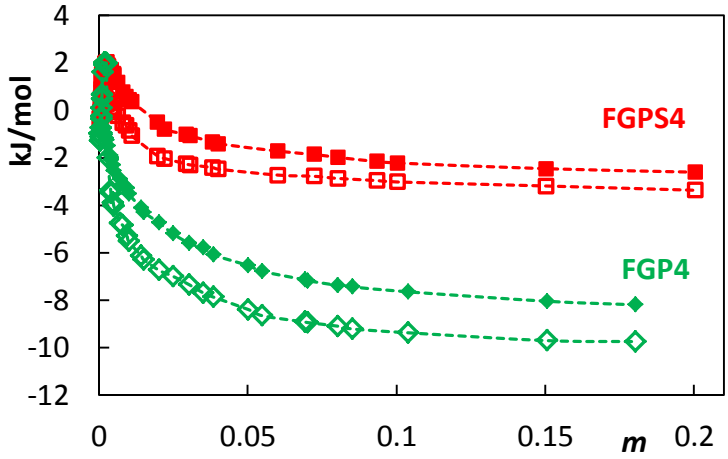

Figure 28. Apparent (full symbols) and partial (empty symbols) molar relative enthalpies of FGP4 (diamonds) and FGPS4 (full squares) as a function of surfactant molality, *m*. Ref.[46].

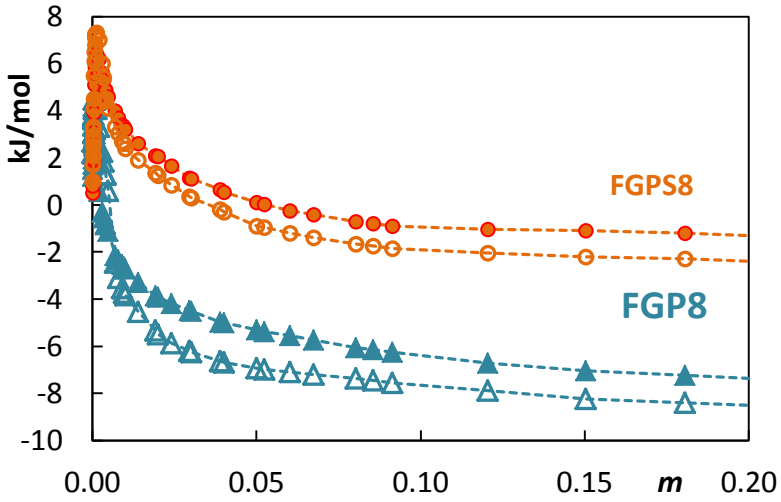

Figure 29. Apparent (full symbols) and partial (empty symbols) molar relative enthalpies of FGP8 (triangles) and FGPS8 (circles) as a function of surfactant molality, *m*. Ref.[46].

Table 1.

Molality (*m*), enthalpies of dilution (ΔH_d), apparent (L_Φ) and partial molar (L_2) enthalpies of the 1,1'-Bis(3,3,4,4,5,5,6,6,7,7,8,8,8-tridecafluorooctyl)-2,2′-trimethylenebispyridinium dichloride (FGP3), in water at 298 K (subscript *i* stands for initial and *f* for final state).

m_i *(mol Kg^{-1})*	m_f *(mol Kg^{-1})*	ΔH_d *(J mol^{-1})*	Φ_{Li} *(J mol^{-1})*	Φ_{Lf} *(J mol^{-1})*	L_{2i} *(J mol^{-1})*	L_{2f} *(J mol^{-1})*
0.00060	0.00030	-162.96	30	-139	594	-96
0.00070	0.00035	-271.95	135	-127	949	-19
0.00080	0.00040	-365.26	262	-107	1358	76
0.00090	0.00045	-433.44	402	-81	1363	187
0.00100	0.00055	-363.45	423	-10	1360	454
0.00156	0.00073	-277.96	458	180	1100	1096
0.00206	0.00103	140.98	299	440	100	1360
0.00255	0.00123	553.73	-89	465	-1100	1350
0.00301	0.00149	1287.72	-680	470	-1800	1100
0.00415	0.00213	1551.94	-1150	450	-3000	100
0.00500	0.00249	1751.61	-1421	300	-3400	-1100
0.00601	0.00298	1600.67	-1880	-680	-3680	-1800
0.00702	0.00345	1560.30	-2310	-850	-4000	-2700
0.00802	0.00396	1520.75	-2520	-1080	-4200	-2950
0.00912	0.00464	1482.00	-2782	-1400	-4450	-3280
0.01006	0.00507	1410.10	-2840	-1430	-4600	-3420
0.03017	0.01451	1375.79	-4765	-3390	-6340	-5200
0.05004	0.02496	1354.16	-5654	-4330	-7380	-5960
0.08030	0.03820	1321.77	-6512	-5190	-8300	-6750
0.10029	0.04764	1378.53	-6968	-5490	-8850	-7280
0.15079	0.07049	1382.97	-7612	-6230	-9480	-8050
0.20054	0.09366	1380.15	-7850	-6770	-9650	-8660

Table 2.

Molality (*m*), enthalpies of dilution (ΔH_d), apparent (L_Φ) and partial molar (L_2) enthalpies of the 1,1'-Bis(3,3,4,4,5,5,6,6,7,7,8,8,8-tridecafluorooctyl)-2,2′-tetramethylenebispyridinium dichloride (FGP4), in water at 298 K (subscript *i* stands for initial and *f* for final state).

m_i *(mol Kg^{-1})*	m_f *(mol Kg^{-1})*	ΔH_d *(J mol^{-1})*	ΦL_i *(J mol^{-1})*	ΦLf *(J mol^{-1})*	L_{2i} *(J mol^{-1})*	L_{2f} *(J mol^{-1})*
0.00060	0.00030	214.82	-999	-820	-1110	-980
0.00070	0.00034	162.68	-996	-842	-755	-1278
0.00080	0.00038	42.70	-943	-895	-375	-1297
0.00090	0.00043	-98.04	-853	-939	104	-1288
0.00100	0.00082	-233.24	-731	-899	659	-250
0.00200	0.00096	-236.37	-1041	-777	2000	457
0.00251	0.00120	157.61	-1254	-796	1990	1600
0.00300	0.00189	964.15	-1489	-1025	-2000	1980
0.00400	0.00189	1506.40	-2090	-960	-3500	1900
0.00501	0.00237	1534.10	-2550	-1190	-4050	1993
0.00802	0.00396	1521.13	-3121	-1900	-4850	-3400
0.01002	0.00480	1517.60	-3527	-2310	-5530	-3900
0.01504	0.00714	1499.83	-4299	-2900	-6300	-4780
0.02025	0.00943	1462.16	-4750	-3287	-6750	-5300
0.03043	0.01416	1391.25	-5611	-4120	-7360	-6140
0.05022	0.02490	1239.40	-6549	-5210	-8400	-7000
0.07017	0.03505	1183.00	-7184	-5801	-8950	-7700
0.08022	0.03858	1112.24	-7382	-6099	-9100	-7880
0.10397	0.05491	1064.54	-7654	-6790	-9380	-8660
0.15067	0.06932	1068.71	-8050	-7150	-9710	-8930
0.18040	0.08526	1070.81	-8200	-7448	-9750	-9220

Table 3.

Molality (m), enthalpies of dilution (ΔH_d), apparent (L_Φ) and partial molar (L_2) enthalpies of the 1,1'-Bis(3,3,4,4,5,5,6,6,7,7,8,8,8-tridecafluorooctyl)-2,2′-octamethylenebispyridinium dichloride (FGP8), in water at 298 K (subscript *i* stands for initial and *f* for final state).

m_i (mol Kg^{-1})	m_f (mol Kg^{-1})	ΔH_d (J mol^{-1})	Φ_{Li} (J mol^{-1})	Φ_{Lf} (J mol^{-1})	L_{2i} (J mol^{-1})	L_{2f} (J mol^{-1})
0.00040	0.00018	-1015	2240	1207	3767	2197
0.00050	0.00023	-1117	2591	1508	4189	2691
0.00060	0.00028	-1123	2882	1744	4465	3060
0.00060	0.00028	-1152	2888	1736	4470	3047
0.00070	0.00033	-1134	3092	1958	4480	3377
0.00080	0.00038	-1038	3217	2179	4482	3686
0.00085	0.00037	-1047	3181	2134	4485	3625
0.00090	0.00041	-924	3218	2294	4487	3837
0.00100	0.00047	-628	2600	2483	4470	4068
0.00200	0.00094	1722	578	3200	3300	4480
0.00301	0.00139	2101	-300	-1800	2250	4465
0.00702	0.00339	1765	-2165	-400	-2450	2240
0.00803	0.00404	1544	-2343	-800	-3100	1300
0.00903	0.00413	1691	-2542	-850	-3550	1280
0.01004	0.00473	1607	-2727	-1120	-3850	1000
0.02004	0.00962	1259	-3909	-2650	-5500	-3730
0.03010	0.01409	1206	-4506	-3300	-6250	-4550
0.04009	0.01927	1156	-5016	-3860	-6700	-5320
0.05009	0.02408	1119	-5319	-4200	-6950	-5890
0.06019	0.02956	1059	-5559	-4500	-7100	-6200
0.08025	0.03890	1083	-6063	-4980	-7370	-6650
0.12055	0.05245	1341	-6721	-5380	-7900	-6980
0.15042	0.06739	1295	-7045	-5750	-8230	-7200
0.18062	0.08564	1514	-7240	-6160	-8400	-7450
0.20050	0.09144	1618	-7370	-6250	-8500	-7550

Table 4.

Molality (m), enthalpies of dilution (ΔH_d), apparent (L_Φ) and partial molar (L_2) enthalpies of the 1,1'-Bis(3,3,4,4,5,5,6,6,7,7,8,8,8-tridecafluorooctyl)-2,2′-dodecamethylenebispyridinium dichloride (FGP12), in water at 298 K (subscript *i* stands for initial and *f* for final state).

m_i (*mol Kg^{-1}*)	m_f (*mol Kg^{-1}*)	ΔH_d (*J mol^{-1}*)	Φ_{Li} (*J mol^{-1}*)	Φ_{Lf} (*J mol^{-1}*)	L_{2i} (*J mol^{-1}*)	L_{2f} (*J mol^{-1}*)
0.00050	0.00025	2235	-4468	-2274	-8682	-4468
0.00060	0.00030	2515	-5302	-2715	-10265	-5322
0.00070	0.00035	3010	-6121	-3143	-11810	-6146
0.00080	0.00040	3078	-6661	-3583	-13000	-7759
0.00100	0.00049	2796	-7212	-4416	-13300	-8583
0.00200	0.00099	2489	-9689	-7200	-14200	-13280
0.00501	0.00250	1736	-12736	-11000	-15100	-14380
0.00801	0.00400	1532	-13800	-12100	-15920	-14800
0.00902	0.00451	1484	-13983	-12500	-16180	-14960
0.01002	0.00511	1406	-14146	-12740	-16380	-15100
0.02004	0.01004	1305	-15445	-14140	-17960	-16400
0.04003	0.01840	1762	-17062	-15300	-19800	-17700
0.05223	0.02406	1974	-17774	-15800	-20640	-18400
0.06016	0.02700	2300	-18300	-16000	-21120	-18700
0.07005	0.03336	2238	-18837	-16600	-21600	-19200
0.08019	0.03881	2308	-19200	-16980	-21960	-19680
0.09005	0.04228	2241	-19500	-17200	-22180	-19920
0.10013	0.04690	2183	-19800	-17460	-22400	-20220
0.15037	0.06779	1934	-20600	-18700	-23000	-21500
0.20241	0.08420	1842	-21222	-19380	-23500	-22060

Table 5.

Molality (m), enthalpies of dilution (ΔH_d), apparent (L_Φ) and partial molar (L_2) enthalpies of the 1,1'-Bis(3,3,4,4,5,5,6,6,7,7,8,8,8-tridecafluorooctyl)-2,2′-tetramethylenebispyridinium-dimethanosulfonate (FGPS4), in water at 298 K (subscript *i* stands for initial and *f* for final state).

m_i (mol Kg^{-1})	m_f (mol Kg^{-1})	ΔH_d (J mol^{-1})	Φ_{Li} (J mol^{-1})	Φ_{Lf} (J mol^{-1})	L_{2i} (J mol^{-1})	L_{2f} (J mol^{-1})
0,00060	0,00030	-52,8	-189	-262	206	-328
0,00070	0,00035	-132,2	-111	-269	516	-284
0,00080	0,00040	-250,3	-8	-267	895	-222
0,00090	0,00044	-400,9	112	-261	1309	-162
0,00100	0,00049	-542,9	266	-245	1522	-62
0,00154	0,00076	-1387,0	1351	-49	1500	748
0,00200	0,00100	-1724,6	1984	260	690	1560
0,00250	0,00125	-1350,8	2039	688	450	1800
0,00300	0,00153	-603,3	1914	1311	340	1546
0,00400	0,00200	122,3	1700	1980	100	690
0,00500	0,00254	573,4	1464	2040	-60	420
0,00625	0,00317	621,4	1179	1850	-220	300
0,00802	0,00392	916,3	774	1690	-520	120
0,00907	0,00465	976,4	574	1550	-640	10
0,01003	0,00496	1070,5	450	1520	-850	-40
0,02203	0,01106	951,3	-800	350	-2030	-1080
0,04009	0,01964	820,2	-1410	-490	-2480	-1920
0,06011	0,02929	721,3	-1721	-1020	-2730	-2260
0,08016	0,30600	703,1	-1983	-1080	-2870	-2300
0,10021	0,03814	680,8	-2220	-1330	-3020	-2410
0,15028	0,07227	701,4	-2461	-1860	-3190	-2780
0,02004	0,09337	707,7	-2607	-2160	-3370	-2960

Table 6.

Molality (m), enthalpies of dilution (ΔH_d), apparent (L_Φ) and partial molar (L_2) enthalpies of the 1,1'-Bis(3,3,4,4,5,5,6,6,7,7,8,8,8-tridecafluorooctyl)-2,2′-octamethylenebispyridinium-dimethanosulfonate (FGPS8), in water at 298 K (subscript *i* stands for initial and *f* for final state).

m_i *(mol Kg^{-1})*	m_f *(mol Kg^{-1})*	ΔH_d *(J mol^{-1})*	Φ_{Li} *(J mol^{-1})*	Φ_{Lf} *(J mol^{-1})*	L_{2i} *(J mol^{-1})*	L_{2f} *(J mol^{-1})*
0,00040	0,00018	-1980	2500	500	3200	1000
0,00050	0,00023	-3140	3900	800	4500	1700
0,00060	0,00028	-3560	4500	1000	5500	2100
0,00070	0,00032	-3320	5100	1700	6100	2500
0,00080	0,00038	-3600	5550	2000	6500	2900
0,00085	0,00037	-3790	5800	1900	6800	2700
0,00090	0,00042	-3420	5900	2500	7100	3300
0,00100	0,00047	-2980	6100	3100	7250	4100
0,00200	0,00094	-180	6200	6000	7000	7200
0,00301	0,00139	850	5600	6400	6000	7300
0,00700	0,00340	1300	4000	5300	3300	5400
0,00803	0,00404	1220	3700	4900	3050	4500
0,00903	0,00413	1420	3400	4850	2700	4400
0,01004	0,00473	1390	3200	4600	2400	4100
0,02004	0,00962	1259	2050	3300	1250	2600
0,03010	0,01409	1520	1100	2600	300	1900
0,04010	0,01927	1560	550	2100	-300	1350
0,05009	0,02410	1630	10	1650	-950	850
0,06019	0,02956	1400	-240	1150	-1200	350
0,08025	0,03892	1260	-610	640	-1650	-200
0,12057	0,05246	1010	-1040	10	-2030	-950
0,15040	0,06740	700	-1100	-410	-2200	-1400
0,18063	0,08562	460	-1250	-800	-2300	-1750
0,20051	0,09143	400	-1300	-910	-2400	-1850

- *Apparent volume and adiabatic compressibility of the fluorinated gemini*

The apparent molar volumes, V_Φ are obtained by the equation:

$$V_\Phi = \frac{M}{d} - \frac{10^3(d-d_o)}{mdd_o} \quad (13)$$

where d is the density of the solution of molality m, M is the molecular weight of the surfactants, and d_o is the density of the solvent.

The obtained trends of V_Φ vs. m are shown in Figure 30. The apparent molar adiabatic compressibility, $K_{s,\Phi}$, is given by[47-50].

$$K_{S,\phi} = \frac{M\beta_S}{d} - \frac{10^3(\beta_{s,o}d-\beta_{s,o}d_o)}{mdd_o} \quad (14)$$

where $\beta_{s,o}$ is the coefficient of adiabatic compressibility of the solvent and β_s is the coefficient of adiabatic compressibility of the solute. Equation (14) is computed from sound velocity, u and density data as

$$\beta_S = 100/(u^2 d) \quad (15)$$

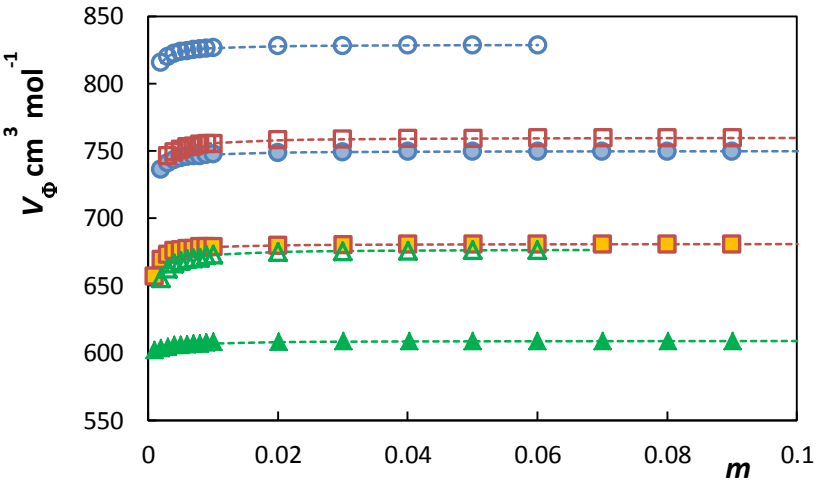

Figure 30. Apparent molar volumes of FGP*n* (full symbols) and FGPS*n* (empty symbols) with n = 4 (triangles), n = 8 (squares) and n = 12 (circles) as a function of surfactant molality, m. Broken lines show the function computed by equation (6). Ref.[46].

In Figures 31 and 32, the apparent molar isoentropic compressibilities as a function of concentration of sulfonates and chlorides, respectively are shown.

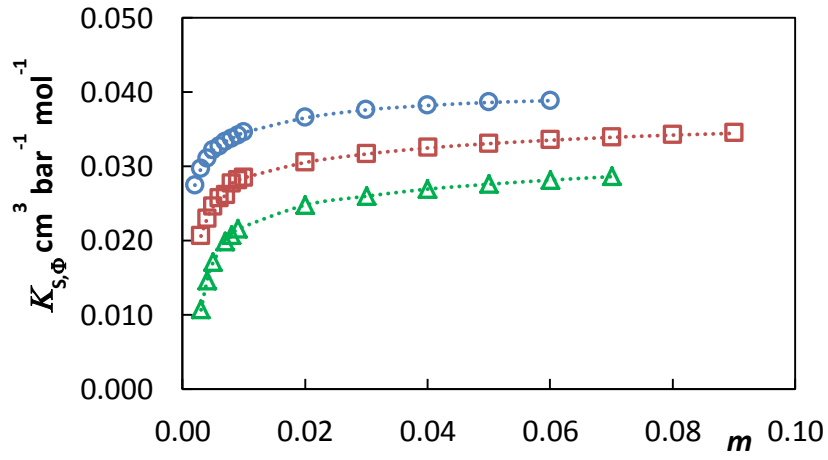

Figure 31. Apparent molar adiabatic compressibilities of FGPS*n* with n = 4 (triangles), n = 8 (squares) and n = 12 (circles) as a function of surfactant molality, m. Broken lines show the function computed by equation (16). Ref.[46].

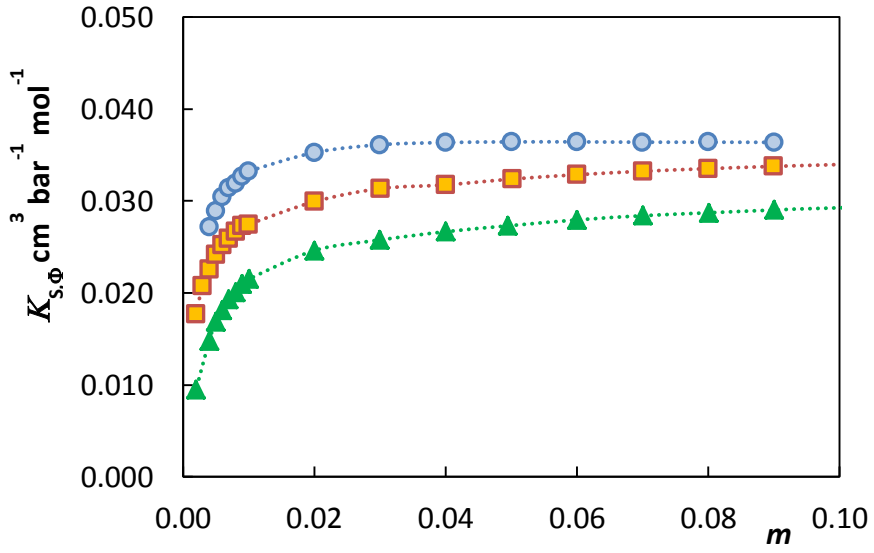

Figure 32. Apparent molar adiabatic compressibilities of FGP*n* with *n* = 4 (triangles), *n* = 8 (squares) and *n* = 12 (circles) as a function of surfactant molality, *m*. Broken lines show the function computed by equation (16). Ref.[46].

Following a pseudo-phase transition model, the trends observed above the cmc can be described by the equation:

$$X_{\Phi} = X_{\Phi,M} - (\text{cmc} \cdot \Delta X_{\Phi}) \cdot (1/m) \qquad (16)$$

where X stands for the property being investigated. The values of $X_{\Phi,M}$, the property in micellar phase, and ΔX_{Φ}, the change in property upon micellization, can be obtained by a least square fit, if the values of cmc are known[21]. Table 7 shows the values thus derived, together with the values of $X_{\Phi,S}$, the value at the cmc, from:

$$X_{\Phi,S} = X_{\Phi,M} - \Delta X_{\Phi} \qquad (17)$$

Table 7.

Cmc by conductivity measurements, apparent molar volume in micellar phase ($V_{\Phi,M}$), change in apparent molar volume upon micellization (ΔV_{mic}), apparent molar volume at the cmc ($V_{\Phi,cmc}$), isoentropic compressibilities in micellar phase ($Ks_{\Phi,M}$), change in isoentropic compressibilities upon micellization (ΔKs_{mic}), isoentropic compressibilities at the cmc ($Ks_{\Phi,cmc}$), change in enthalpy upon micellization (ΔH_{mic}) for compounds under investigation.

	Cmc[a]	$V_{\Phi,M}$	ΔV_{mic}	$V_{\Phi,cmc}$	$Ks_{\Phi,M}$	ΔKs_{mic}	$Ks_{\Phi,cmc}$	ΔH_{mic}
	mM	$cm^3\ mol^{-1}$	$cm^3\ mol^{-1}$	$cm^3\ mol^{-1}$	$bar^{-1}\ cm^3\ mol^{-1}$	$bar^{-1}\ cm^3\ mol^{-1}$	$bar^{-1}\ cm^3\ mol^{-1}$	$kJ\ mol^{-1}$
FGP4	1.86	609	21	588	0.028688	0.031323	-0.002635	-10.5[b]
FGP8	1.29	681	24	657	0.033062	0.034519	-0.001457	-8.9[b]
FGP12	1.10	750	26	724	0.037146	0.037273	-0.000127	-23[b]
FGPS4	1.93	677	22	655	0.028582	0.031290	-0.002708	-4.6
FGPS8	1.40	760	24	736	0.033991	0.034286	-0.0002947	-3.2
FGPS12	1.05	829	26	803	0.038908	0.037020	0.0018880	--

[a] cmc, from conductivity measurements, Ref.[39].
[b] Ref.[46].

Table 8.

Density (d), apparent molar volume (V_Φ), sound velocity (U), coefficient of adiabatic compressibility (β_s) and isentropic compressibilities ($K_{s,\Phi}$) as a function of molality (m) of FGPS4 gemini surfactant in water at 298 K.

m (mol Kg^{-1})	d (g cm^3)	V_Φ (cm^3 mol^{-1})	U (m s^{-1})	10^5 β_s (bar^{-1})	$K_{s,\Phi}$ (cm^3 mol^{-1} bar^{-1})
0.00300	0.998351	662.6	1497.04	4.4694	0.008490
0.00400	0.998776	666.2	1496.74	4.4693	0.013499
0.00500	0.999182	668.2	1496.34	4.4699	0.017111
0.00600	0.999601	669.5	1496.19	4.4689	0.018492
0.00700	1.000020	670.0	1495.84	4.4691	0.019882
0.00800	1.000436	670.8	1495.59	4.4687	0.020660
0.00900	1.000846	672.3	1495.32	4.4685	0.021550
0.01001	1.001264	672.8	1495.07	4.4681	0.022493
0.02001	1.005389	674.7	1492.45	4.4655	0.024788
0.03001	1.009453	675.5	1489.68	4.4640	0.025979
0.04001	1.013469	675.8	1486.83	4.4634	0.026939
0.05002	1.017430	676.2	1483.99	4.4631	0.027593
0.06004	1.021333	676.5	1481.11	4.4633	0.028147
0.07014	1.025241	676.4	1478.20	4.4638	0.028623

Table 9.

Density (d), apparent molar volume (V_Φ), sound velocity (U), coefficient of adiabatic compressibility (β_s) and isentropic compressibilities ($K_{s,\Phi}$) as a function of molality (m) of FGPS8 gemini surfactant in water at 298 K.

m (mol Kg^{-1})	d (g cm^3)	V_Φ (cm^3 mol^{-1})	U (m s^{-1})	10^5 β_s (bar^{-1})	$K_{s,\Phi}$ (cm^3 mol^{-1} bar^{-1})
0.00300	0.998264	746.0	1496.61	4.4724	0.020607
0.00400	0.998657	749.2	1496.36	4.4721	0.022977
0.00500	0.999049	751.1	1496.10	4.4719	0.024595
0.00601	0.999441	752.8	1495.87	4.4715	0.025706
0.00701	0.999832	753.2	1495.60	4.4714	0.026097
0.00801	1.000221	754.6	1495.34	4.4712	0.027642
0.00901	1.000609	755.1	1495.08	4.4710	0.028099
0.01001	1.000998	755.4	1494.82	4.4708	0.028451
0.02004	1.004860	757.9	1492.16	4.4695	0.030525
0.03002	1.008651	758.4	1489.32	4.4697	0.031662
0.04007	1.012399	759.0	1486.42	4.4706	0.032477
0.05007	1.016086	759.2	1483.50	4.4719	0.033065
0.06011	1.019726	759.3	1480.57	4.4736	0.033519
0.07011	1.023320	759.4	1477.72	4.4751	0.033908
0.08006	1.026807	759.5	1474.80	4.4776	0.034209
0.09006	1.030243	759.6	1472.01	4.4796	0.034448
0.10013	1.033695	759.6	1469.30	4.4811	0.034653

Table 10.

Density (d), apparent molar volume (V_Φ), sound velocity (U), coefficient of adiabatic compressibility (β_s) and isentropic compressibilities ($K_{s,\Phi}$) as a function of molality (m) of FGPS12 gemini surfactant in water at 298 K.

m (mol Kg^{-1})	d (g cm^3)	V_Φ (cm^3 mol^{-1})	U (m s^{-1})	10^5 β_s (bar^{-1})	$K_{s,\Phi}$ (cm^3 mol^{-1} bar^{-1})
0.00300	0.998211	819.9	1496.36	4.4741	0.026252
0.00400	0.998590	822.0	1495.97	4.4748	0.029418
0.00500	0.998968	823.8	1495.87	4.4736	0.032144
0.00600	0.999346	824.2	1495.61	4.4735	0.032687
0.00700	0.999724	825.0	1495.32	4.4735	0.033322
0.00800	1.000100	825.7	1495.05	4.4735	0.033693
0.00900	1.000475	826.1	1494.76	4.4735	0.034167
0.01000	1.000852	826.3	1494.47	4.4736	0.034546
0.02004	1.004582	827.8	1491.44	4.4751	0.036521
0.03000	1.008234	828.1	1488.31	4.4777	0.037598
0.04001	1.011831	828.4	1485.19	4.4805	0.038190
0.04998	1.015361	828.5	1482.16	4.4832	0.038598
0.06006	1.018877	828.6	1479.24	4.4854	0.038841

Table 11.

Density (d), apparent molar volume (V_Φ), sound velocity (U), coefficient of adiabatic compressibility (β_s) and isentropic compressibilities ($K_{s,\Phi}$) as a function of molality (m) of FGP4 gemini surfactant in water at 298 K.

m (mol Kg^{-1})	d (g cm^3)	V_Φ (cm^3 mol^{-1})	U (m s^{-1})	10^5 β_s (bar^{-1})	$K_{s,\Phi}$ (cm^3 mol^{-1} bar^{-1})
0.00300	0.998169	602.2	1496.90	4.4711	0.011377
0.00400	0.998538	603.6	1496.64	4.4712	0.014666
0.00500	0.998905	604.7	1496.39	4.4708	0.016594
0.00600	0.999270	605.7	1496.14	4.4709	0.018250
0.00700	0.999637	606.0	1495.92	4.4705	0.019132
0.00800	1.000000	606.5	1495.64	4.4700	0.020092
0.00900	1.000367	606.8	1495.32	4.4702	0.021728
0.01002	1.000738	607.0	1495.11	4.4703	0.021728
0.02007	1.004384	607.9	1492.28	4.4708	0.024807
0.03008	1.007967	608.2	1489.46	4.4717	0.026097
0.04025	1.011562	608.5	1487.02	4.4707	0.025989
0.05005	1.014991	608.6	1484.10	4.4731	0.026738
0.06003	1.018440	608.7	1480.37	4.4805	0.027940
0.07007	1.021869	608.8	1477.38	4.4835	0.028400
0.08010	1.025256	608.8	1474.30	4.4874	0.028715
0.09012	1.028595	608.8	1471.31	4.4910	0.029018
0.10025	1.031938	608.8	1468.28	4.4950	0.029261
0.20089	1.063142	608.9	1440.79	4.5311	0.030652

Table 12.

Density (d), apparent molar volume (V_Φ), sound velocity (U), coefficient of adiabatic compressibility (β_s) and isentropic compressibilities ($K_{s,\Phi}$) as a function of molality (m) of FGP8 gemini surfactant in water at 298 K.

m (mol Kg^{-1})	d (g cm^3)	V_Φ (cm^3 mol^{-1})	U (m s^{-1})	10^5 β_s (bar^{-1})	$K_{s,\Phi}$ (cm^3 mol^{-1} bar^{-1})
0.00200	0.997773	669.2	1496.74	4.4738	0.017700
0.00300	0.998126	673.1	1496.53	4.4735	0.020791
0.00401	0.998479	675.6	1496.29	4.4733	0.022592
0.00501	0.998830	676.3	1496.03	4.4733	0.024141
0.00600	0.999178	677.2	1495.76	4.4734	0.025196
0.00700	0.999531	677.2	1495.50	4.4733	0.025882
0.00800	0.999878	678.5	1495.21	4.4735	0.026656
0.00901	1.000231	678.6	1494.93	4.4736	0.027294
0.01001	1.000580	678.8	1494.65	4.4737	0.027463
0.02000	1.004049	679.5	1491.97	4.4743	0.029919
0.03005	1.007476	680.2	1488.99	4.4769	0.031346
0.04003	1.010864	680.4	1485.76	4.4814	0.031753
0.05016	1.014214	680.5	1482.60	4.4856	0.032385
0.06001	1.017473	680.6	1479.54	4.4898	0.032853
0.07004	1.020686	680.7	1476.47	4.4943	0.033230
0.08002	1.023905	680.7	1473.43	4.4986	0.033515
0.09002	1.027087	680.7	1470.46	4.5028	0.033762
0.10010	1.030205	680.8	1467.56	4.5070	0.033962

Table 13.

Density (d), apparent molar volume (V_Φ), sound velocity (U), coefficient of adiabatic compressibility (β_s) and isentropic compressibilities ($K_{s,\Phi}$) as a function of molality (m) of FGP12 gemini surfactant in water at 298 K.

m (mol Kg^{-1})	d (g cm^3)	V_Φ (cm^3 mol^{-1})	m (mol Kg^{-1})	U (m s^{-1})	10^5 β_s (bar^{-1})	$K_{s,\Phi}$ (cm^3 mol^{-1} bar^{-1})
0.00200	0.997751	736.3	0.00400	1496.46	4.4756	0.027164
0.00300	0.998090	741.1	0.00500	1496.12	4.4761	0.028923
0.00401	0.998430	743.1	0.00600	1495.77	4.4766	0.030412
0.00501	0.998768	744.9	0.00700	1495.43	4.4772	0.031442
0.00601	0.999106	745.5	0.00800	1495.14	4.4774	0.031892
0.00700	0.999441	746.3	0.00900	1494.76	4.4782	0.032685
0.00800	0.999779	746.4	0.01001	1494.45	4.4785	0.033210
0.00900	1.000115	747.2	0.02001	1491.28	4.4961	0.035259
0.01001	1.000455	747.8	0.03003	1488.05	4.5141	0.036111
0.02001	1.003786	748.6	0.04003	1485.00	4.5176	0.036353
0.03002	1.007069	749.1	0.05001	1482.06	4.5207	0.036423
0.04003	1.010295	749.3	0.05998	1479.39	4.5226	0.036425
0.05005	1.013493	749.6	0.07003	1476.76	4.5244	0.036392
0.06006	1.016653	749.5	0.08005	1474.18	4.5261	0.036394
0.06998	1.019714	749.7	0.09000	1471.46	4.5292	0.036374
0.08004	1.022789	749.7	0.10012	1468.83	4.5318	0.036889
0.09003	1.025798	749.7				
0.10029	1.028857	749.7				

- *Surface Tension Measurements*

The surface tension measurements (γ *vs.* log *c*) for both hydrogenated and partially fluorinated compound under investigation are reported in Table 14 and shown in Figure 33 and 34. Several parameters were determined from the γ *vs.* log *c* plots by using the Gibbs adsorption equation (18)[44,52]: (i) the critical micelle concentration (cmc), taken as the concentrations at the point of intersection of the two linear portions of the γ *vs.* log *c* plots; (ii) the maximum surface excess concentration Γ_{max} [mol cm^{-2}]; (iii) the area per molecule at the interface A_{min} [nm^2] from equation (19); (iv) the efficiency in surface tension reduction, measured by C_{20}, i.e. the molar surfactant concentration required to reduce the surface tension of the solvent by 20 mN/m[53]; (v) the effectiveness of the surface tension reduction, measured by the surface tension at the cmc, γ_{cmc}; (vi) the cmc/C_{20} ratio, i.e. the measure of the tendency to form micelles relative to the tendency to adsorb at the air/water interface.

$$\Gamma_{max} = -\frac{1}{2.303nRT}\left(\frac{\partial\gamma}{\partial \log C}\right)_T \qquad (18)$$

$$A_{min} = \frac{10^{16}}{N\Gamma_{max}} \qquad (19)$$

The value of *n* (the number of species whose concentration at the interface changes with *c*) is taken as 2, although for divalent gemini (having 1 surfactant ion and 2 non surfactant counterions) the values of both 2 and 3 have been proposed[44,54]. For gemini surfactants, it was found that one of the two counterions is frequently firmly wedged in

between the two charged head groups, especially when the spacer is quite short[55]. While the use of a different *n* does not affect the general trend for surface areas, the last finding enabled us to use *n* = 2 with some confidence.

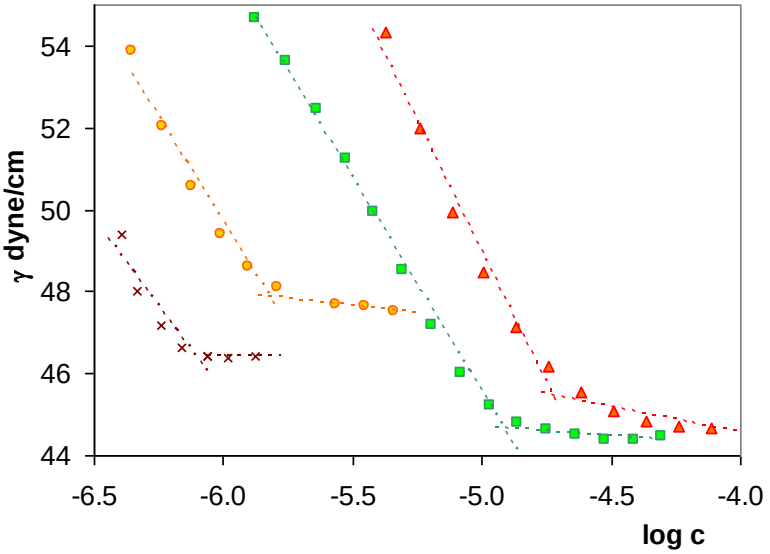

Figure 33. Surface tension (γ) as a function of the logarithm of surfactant concentration (Log C) for the hydrogenated gemini surfactants P16-3 (green); P16-4 (red); P16-8 (orange); P16-12 (purple). Ref.[56].

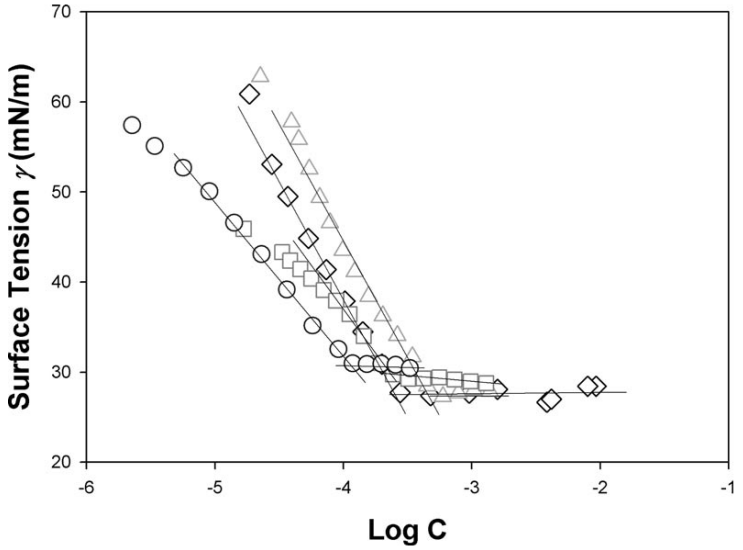

Figure 34. Surface tension (γ) as a function of the logarithm of surfactant concentration (Log C) for the fluorinated gemini surfactant FGP3 (diamonds); FGP4 (triangles); FGP8 (squares); FGP12 (circles). Ref.[39].

Table 14.

Amphiphilic properties of the gemini surfactants under study: both hydrogenated (P16-*n*) and fluorinated (FGP*n*) ones.

Compound	s	cmc[a] [mmol/L]	β[a]	cmc[b] [mmol/L]	γ_{cmc} [dyne/cm]	$\Gamma \cdot 10^{10}$ [mol/cm^2]	A_{min} [Å^2]	pC_{20}	cmc/C_{20}
P16-3	3	0.0851	61	0.012	44.47	0.95	174.72	5.61	4.74
P16-4	4	0.0942	53	0.021	44.74	1.30	146.96	5.24	3.59
P16-8	8	0.0838	49	0.0015	47.61	0.78	211.95	6.29	2.90
P16-12	12	0.0595	56	0.00078	46.42	0.75	221.96	6.76	4.51
FGP3	3	1.82	63	0.28	27.7	2.2	75	4.54	10
FGP4	4	1.76	62	0.50	27.7	2.1	79	4.40	11
FGP8	8	1.22	52	0.25	29.2	1.5	108	5.08	19
FGP12	12	1.04	54	0.12	30.9	1.4	119	5.15	21

[a]Obtained by specific conductivity data following the nonlinear fit method[39,56].
[b]Obtained by surface-tension measurements[39,56].

- *Biological Assays*

The interaction of both P16-*n* and FGP*n*, with *n* = 3, 4, 8, and 12, with plasmid DNA pEGFP-C1 (Clontech) was monitored by agarose gel electrophoresis mobility shift assay (EMSA).

Referring to P16-*n*, reported in Figure 35, the shift activity was observed for all the compounds investigated, able to modify the mobility of DNA at the lowest concentration tested (25 μM).

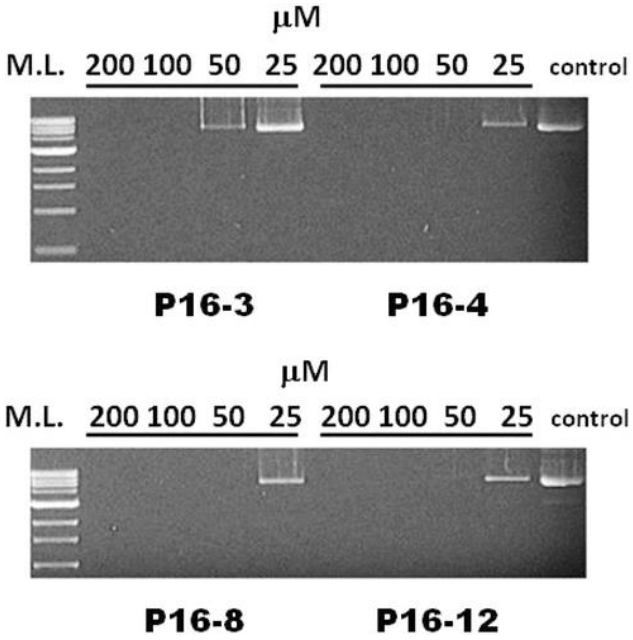

Figure 35. EMSA experiments showing complexation of P16-*n* with circular plasmid pEGFP-C1. Shifting is observable as a function of the concentration (μM). Negative control: plasmid alone, which is completely unshifted. Ref.[66].

Also compounds FGP*n*, Figure 36, are all able to modify the mobility of DNA but starting at a concentration of 100 μM, corresponding to a N/P ratio of 1/1.

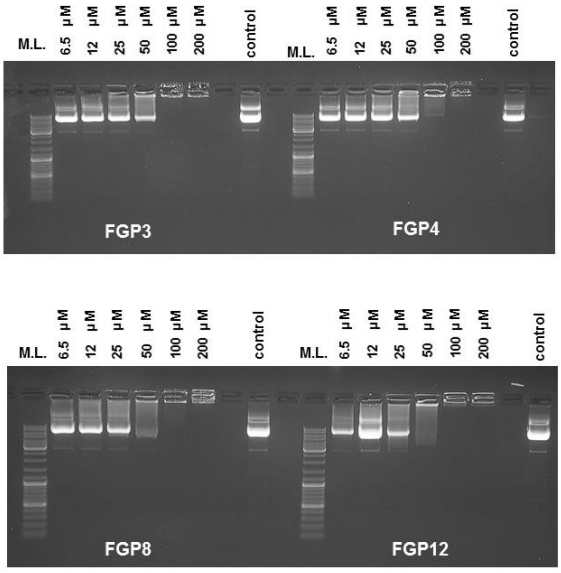

Figure 36. EMSA experiments showing complexation of FGP*n* with circular plasmid pEGFP-C1. Shifting is observable as a function of concentration (μM), at N/P ratios 16/1 (6.5 μM); 8/1 (12 μM); 4/1 (25 μM); 2/1 (50 μM); 1/1 (100 μM); 1/2 (200 μM). Negative control: plasmid alone, which is completely unshifted. Ref.[45].

The cytotoxicity of these fluorinated molecules was tested by an MTT proliferation assay to explore the possibility of exploiting their interaction with DNA to deliver DNA plasmid constructs inside the cells. Given that cytotoxicity has a strong impact in cell transfection, it is necessary to determine the concentration producing the best compromise between cell viability and transfection efficiency for each compound. The results are shown in Figure 37. In general, the cytotoxicity increases with the length of the spacer and, for spacers 3 and 4, this also occurs in presence of DOPE.

At concentrations lower than those selected, cell viability was comparable or higher, but the percentage of transfected cells was lower while, at higher concentrations, the cytotoxicity was too high.

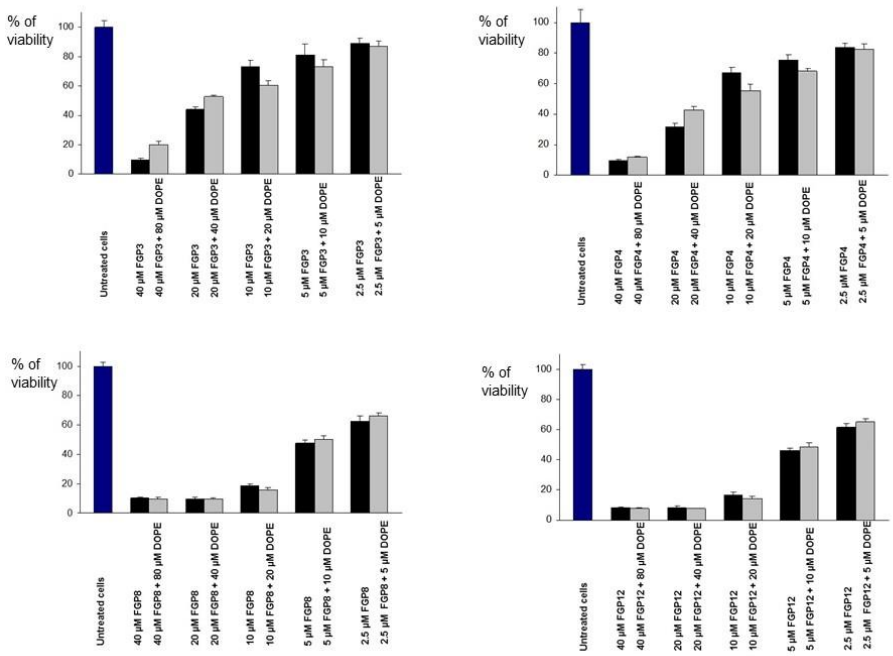

Figure 37. Effects of FGP*n* with *n* =3, 4, 8, and 12 on RD-4 cell line proliferation measured by MTT test after 48 h of incubation. Values are the mean ±S.D. of three independent experiments (n = 8 per treatment, p<0.05). Ref.[45].

Finally, the ability of all hydrogenated and highly fluorinated compounds under investigation, was tested to deliver DNA inside the cells by a transient transfection assay. These experiments were performed with a plasmid carrying an EGFP expression cassette under the control of the Cytomegalovirus (CMV) immediate early promoter (pEGFP-C1, Clontech) to monitor EGFP expression under a fluorescence microscope[45,66]. RD-4 cells were chosen among a large panel of several cell lines because they are a good compromise between difficulty to transfect cells and easiest to transfect cells with traditional methods (electroporation, lypofection, and calcium phosphate precipitation). Moreover, they are easy to handle, fast to grow and are derived from a malignant human cancer.

For the hydrogenated gemini under study, P16-4 was the only one among them able to deliver DNA inside the cells, as shown by EGFP expression, albeit at an efficiency lower than that obtained with a standard commercial transfection reagent (GenePORTER, Gene Therapy System), used as a positive transfection control. It appears that DOPE enhances the transfection activity of cationic formulations through the stabilization of the DNA/ lipid complex[57,58] and facilitates the transfer of DNA in the context of endosomal escape, owing to its fusogenic property. Previous studies have demonstrated that DOPE significantly affects the polymorphic features of lipoplexes promoting transition from a lamellar to a hexagonal phase, thus facilitating endosomal escape[59].

Furthermore it has been tested the in vitro transfection efficiency of P16-*n* formulated with DOPE at different P16-*n*:DOPE molar ratios (1:1, 1:2, and 2:1). The concentration of P16-*n* was fixed at 15 μM. Addition of DOPE increases the transfection efficiency of P16-4 and P16-8 a little, but it is ineffective with P16-3 and P16-12. In particular, P16-4 shows, when formulated with DOPE, a transfection ability comparable with that of the standard commercial transfection reagent (Figure 38). On the contrary, the absence of transfection is observed only for the DOPE transfection control.

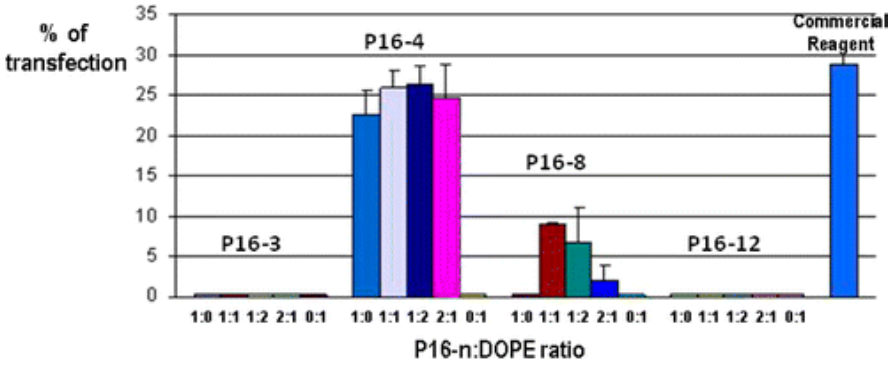

Figure 38. Transfection of RD-4 cells with P16-*n* without and with DOPE in different molar ratios, only DOPE, and the positive control of the commercial GenePORTER standard transfection reagent. Ref.[66].

The fluorinated counterpart FGP*n*, when used without helper lipid, were not able to deliver DNA inside RD-4 cells. Addition of DOPE increased the transfection efficiency of FGP3, FGP4 and FGP8, but it was ineffective with FGP12 (Figure 39). In particular, FGP8 is the only one able to vehicle DNA inside the cells at an efficiency comparable with that obtained with the standard commercial transfection reagent. FGP12 is unable to deliver DNA and, when formulated with DOPE, only 1% of the viable cells give rise to EGFP expression. It has been demonstrated that, when used alone, DOPE is unable to transfect cells[21].

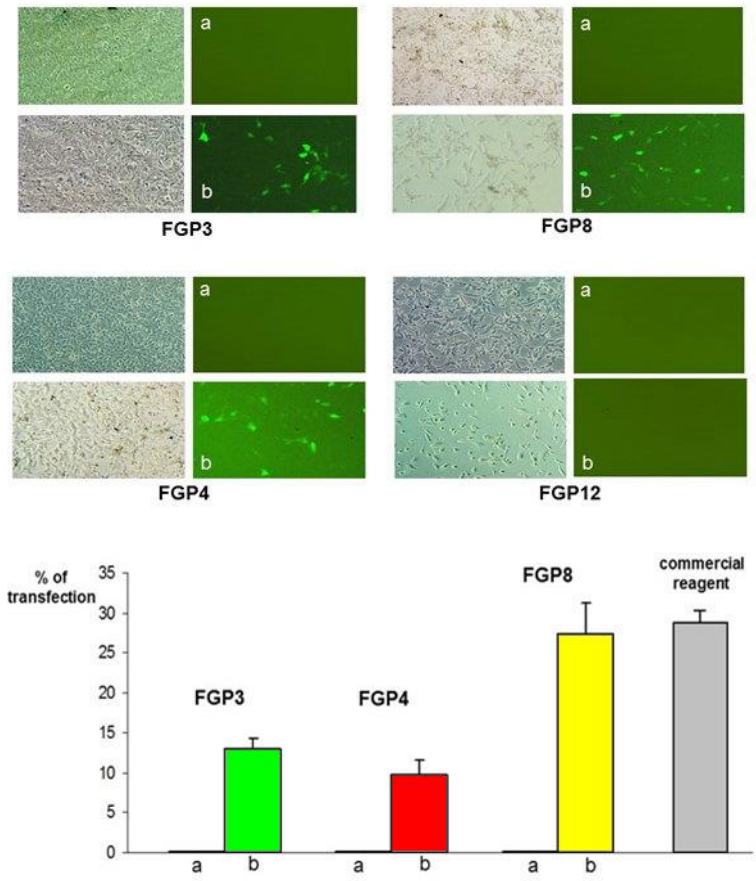

Figure 39. Transfection of RD-4 cells by FGP*n*. For each surfactant, on the left, phase contrast and, on the right, fluorescence microscope observation of RD-4 transfected cells (as shown by green cells expressing EGFP) are shown. Pictures marked by a) refers to experiments done only with the surfactants and by b) with surfactant:DOPE ratio 1:2. Down below: efficiency of transfection obtained by FGP*n* and positive control by a commercial reagent. Five random fields were examined from each well and each experiment was repeated three times. Statistical differences among treatments were calculated with Student's test and multi factorial ANOVA. Ref.[45].

- *AFM Experiments*

The morphology of the structural changes induced in DNA by the compounds under investigation was studied by AFM[60–63], a technique successfully used to study the interaction of synthetic ligands[64], proteins[65] and cationic surfactants[66] with DNA. AFM experiments were performed on air in tapping mode using circular DNA. It was shown that, when deposited onto mica for in air imaging, the DNA molecules are

transported to the surface solely by diffusion and are equilibrated onto the surfaces as in an ideal two-dimensional solution so that the images obtained can be considered representative of the structures present in solution[67]. First, the plasmid DNA alone, deposited onto freshly cleaved mica, was imaged (Figure 40**a** e Figure 41**a**). Single plasmids and concatamers are observed in their plectonemic form with several supercoils, which cause the double helix to cross itself a few times. In spite of the topological constraint, plectonemes appear well extended all over the mica surface.

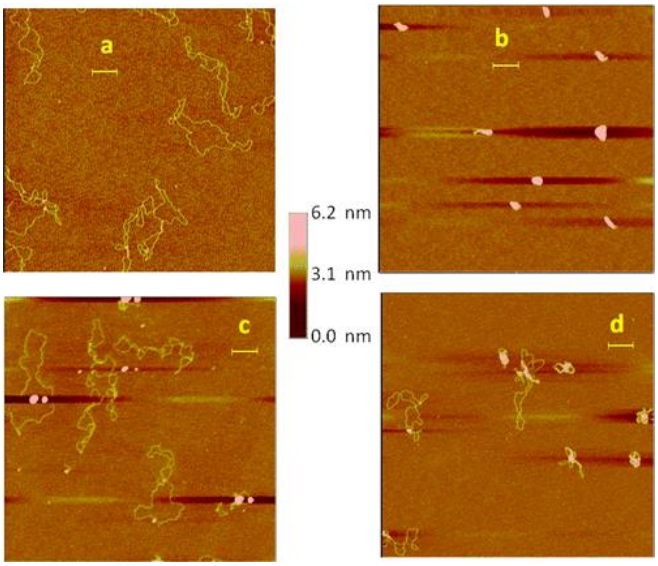

Figure 40. AFM images showing the effect induced on DNA plasmid by incubation with P16-*n* (*n* = 4, 8, 12). Each image represents a 2 × 2 μm scan (scale bar 0.2 μm). All images were obtained with supercoiled 0.5 nM pEGFP-C1 plasmid deposited onto mica and with the microscope operating in tapping mode in air. **a** | DNA plasmid alone. Plasmid incubated with **b** | 2 nM P16-4, **c** | 2 nM P16-8, and **d** | 2 nM P16-12. The chromatic bar inside the Figure refers to the thickness of the particles. Ref.[66].

Parts **b**–**d** of Figure 40 show the plasmid DNA after incubation with the hydrogenated gemini P16-*n* with *n* = 4, 8, and 12 respectively. According to the EMSA results, only P16-4 is able to condense all DNA into nearly spherical nanoparticles less than 0.1 μm

in diameter. After addition of P16-8 (Figure 40**c**) only part of the DNA condenses into nanoparticles homogeneous neither in size nor in shape. In the case of P16-12, the AFM images show that partially condensed structures, if any, are formed, looking like bows (Figure 40**d**). P16-3 (not shown), interacting with DNA as well, is unable to condense the DNA into nanoparticles, but only reduces the extension of the loops formed by plasmid DNA by overlapping of the opposite sides.

The plasmid DNA, after incubation with 5 µM of partially fluorinated FGP*n*, with *n* = 3, 4, 8, and 12, is shown in Figure 41**b**–**e**, respectively.

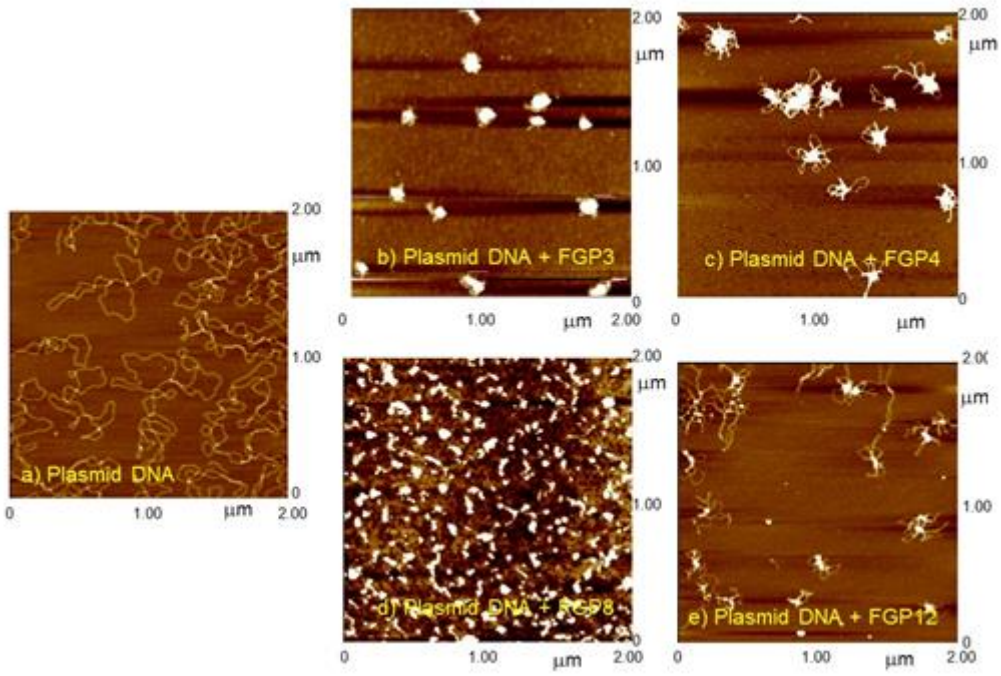

Figure 41. AFM images showing the effect induced on DNA plasmid by incubation with FGP*n*. Each image represents a 2 x 2 µm scan. All images were obtained with supercoiled 0.5 nM pEGFP-C1 plasmid deposited onto mica and with the microscope operating in tapping mode in air at the same N/P ratio as transfection. Ref.[45].

Only FGP8 (Figure 41**d**) seems to be able to condense all DNA into small near spherical nanoparticles. FGP3 (Figure 41**b**) gives rise to larger and less homogeneous

DNA nanoparticles. Incubation with FGP4 results in an incomplete condensation of DNA in distinct structures (Figure 41**c**). AFM images of DNA incubated with FGP12 show that DNA is only partially condensed and the different structures, which resemble bows, are interconnected (Figure 41**e**).

4. DISCUSSION

Thermodynamic properties

The curves of the apparent and partial molar enthalpies as a function of *m* show the typical shape for ionic surfactants: after increasing in the premicellar region, they tend to level off at concentrations above the cmc, where they are almost parallel[44,45,66]. The lowering of the curves in the micellar region is attributed to the electrostatic interactions in micellar solutions, strongly dependent on the counterion radius and polarizability.

In the field of solution thermodynamics, it is useful to express the properties of different molecules using a group contribution approach, i.e. to extract from the experimental data the effect of each brick constituting the molecule[44, 68-70]. This approach has the advantage that the different properties of a new molecule can be evaluated theoretically with a good approximation by adding the contribution of each group. Moreover, if computed and calculated data are in strong disagreement, this could be an indication that the behavior of the molecule in solution has changed. By means of direct methods, we obtained the apparent and partial molar enthalpies at 298 K of the aqueous solutions of the homologous series of the protiated cationic gemini surfactants 1,1'-didodecyl-2,2'-alkylenebispyridinium dichloride[44] and dimethanesulfonate[68]. These data show a very peculiar behavior as a function of the spacer length not allowing for the determination of a CH_2 group contribution when this group is added to the spacer. The deviation of the properties from those theoretically predicted, suggests that something new happens in solutions, such as a phase transition or a change in conformation of the molecule. Our hypothesis is that when the spacer reaches a particular size, the conformational freedom allows the molecule to fold like a book, due to stacking interactions between the two pyridinium rings. When the spacer is too short (2 or 3 carbon atoms), this conformation becomes difficult due to the lack of enough

conformational freedom and it is not possible also when the spacer is too long because the pyridinium rings are too far apart. Comparing the trends of chlorides and methansulfonates we could demonstrate that the counterion plays a crucial role with respect to the energetics of micellar solution, also for dipyridinium gemini surfactants; nevertheless the group contribution additivity for the counterion is respected, independently on the spacer length[68]. This means that the peculiar behavior above described is independent on the counterion. Moreover, owing the lack of data in the literature for partially fluorinated gemini compounds, we have measured the dilution enthalpies of the highly fluorinated analogs and derived the apparent and partial molar enthalpies as a function of *m* (Figures 26 and 27). For a meaningful comparison of the trends of thermodynamic properties in solution of hydrogenate and highly fluorinated gemini pyridinium compounds, we must consider that the hydrophobicity of a $-CF_2-$ group is approximately 1.5 times greater than the $-CH_2-$ group, as shown by the values of the respective cmc[71]. Therefore, we have synthesized the corresponding octyl compounds with the last six carbon atoms fluorinated, which were compared with the 1,1'-didodecyl-2,2'-alkylenebispyridinium chlorides[44].

The trends of the highly fluorinated compounds under investigation, show a very peculiar behavior as well. In fact, the effect of the addition of a $-CH_2-$ to the spacer does not give rise to a monotonic change in the values of the enthalpies in the micellar region, hindering the evaluation of the $-CH_2-$ group contribution. In fact, the trends are very close for the spacers with 3 and 4 carbon atoms, but the curve of FGP4 is still lower than that of FGP3. This means that the addition of a methylene group to the shorter spacer slightly increases the hydrophobicity of the whole molecule. The inversion of the expected trend appears with the eight methylene long spacer. In fact,

FGP8 shows the highest value of apparent and partial molar enthalpies in the plateau region (Figure 42).

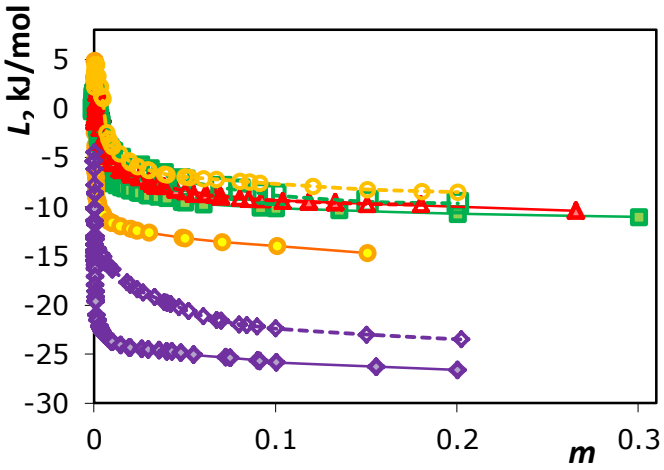

Figure 42. Comparison of partial molar relative enthalpies of hydrogenated gemini surfactants 12-Py(2)-*n*-(2)Py-12 Cl (full symbols) and fluorinated FGP*n* (empty symbols) with n = 3 (squares), n = 4 (tringles); n = 8 (circles); n = 12 (diamonds) as a function of surfactant molality, m. Ref.[45].

The substitution of methanesulfonate by the chloride causes the lowering of the enthalpy curves of partially fluorinated compounds in micellar region of an amount of about 6.1 kJ mol^{-1}, the same value found for the protiated analogues[68], confirming the validity of the group contribution approach for the counterion of the gemini fluorinated surfactants, too. The enthalpy change upon micellization, ΔH_{mic}, results -4.6 kJ mol^{-1} and -3.2 kJ mol^{-1}, for FGPS4 and FGPS8, respectively and was obtained by extrapolating at the cmc the trends of the partial molar properties before and after cmc.

The value of micellization enthalpy is lower by about 5.7 kJ mol^{-1} if the methanesulfonate counterion is replaced by the chloride one, the same value found in the case of protiated analogues[68] confirming the group contribution additivity for the counterion.

DISCUSSION

To reach a complete view of their solution thermodynamics and to gain information about the structure of the hydration sphere of the molecules, we carried out the measurements of the apparent molar volumes and adiabatic compressibilities vs. *m*, never reported before in the literature for these systems. In fact, because volumetric properties (volumes and compressibility) are reflective of the solute-solvent interactions, when micelle formation begins, a great change in these interactions occurs. In Figure 34, the apparent molar volumes of the compounds under study are shown. Volumes of fluorinated surfactants in solution have not been exhaustively studied in literature and, in particular, changes in volumes upon micellization are sometimes in disagreement[69-71]. Tamaki et al. have studied some thermodynamic properties of sodium perfluoroalkanoates and lithium perfluoro-1-alkanesulfonates[72,73]. In particular, they have done an accurate study of volumetric properties of these compounds below the cmc[74]. They obtained a group contribution of 22.63 $cm^3\ mol^{-1}\ CF_2^{-1}$ for the infinite dilution value, in good agreement with the value obtained by us for a homologous series of monomeric partially fluorinated pyridinium chlorides, despite the difference in the charge on the polar head[72]. Some time ago, the research group I'm working with, had the opportunity to study solution thermodynamics of highly fluorinated monomeric surfactants, with chloride as counterion, having a fluorinated alkyl chain (with 4, 6, and 8 fluorinated carbon atoms) bound to the positive nitrogen of the pyridinium ring through a hydrogenated dimethylenic moiety, as the surfactants in this study[70]. For the compound with six fluorinated carbon atoms, considered as the monomer from which our gemini surfactants were built up, we obtained a volume in micellar phase, V_{Φ},m = 281.6 $cm^3\ mol^{-1}$. Using the generally accepted value of 16 $cm^3\ mol^{-1}$ for the CH_2 group[71], we tried to evaluate V_{Φ},m for our dichloride gemini surfactants by the group

contribution approach. They resulted 625, 689 and 753 cm^3 mol^{-1} for n = 4, 8, 12, respectively. These values are greater than the experimental ones (see Table 13) and the difference decreases with the increasing of the spacer length. This means that the presence of the hydrogenated spacer changes the interactions inside the micelles. We have to outline that, because of the very low values of the cmcs, we were not able to measure volumetric properties near and below the cmc. Therefore, the values of V_{Φ},s, the volume at the cmc, and the change in volume upon micellization, ΔV_{mic} have been obtained by a least square fitting, using equation (16). Results are reported in Table 13. These values are strictly dependent on the values of the cmc of the gemini surfactants under investigation. The cmc values of the gemini surfactants is still an open question in the literature. We have shown how the cmc determined by surface tension measurement is even lower by one order of magnitude than that obtained via conductometric measurements, probably owing the formation of small premicellar aggregates, not surface active[39]. If the volumetric parameters obtained from the conductometric value of the cmc are plotted vs. the number of carbon atoms of the spacer (Figure 43), a nice linear relationships can be obtained in the limit of the experimental error.

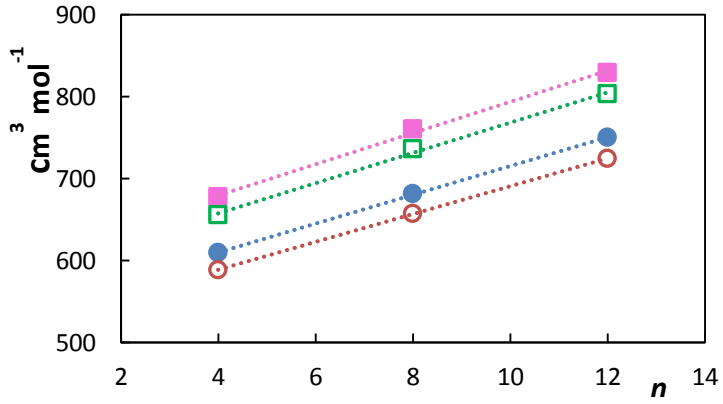

Figure 43. $V_{\Phi,M}$ (full symbols) and $V_{\Phi,S}$ (empty symbols) vs the number, *n*, of carbon atoms in the spacer for FGP*n* (circles) and FGPS*n* (squares). Ref.[45].

DISCUSSION

The group contribution of the CH_2 group in the spacer can be derived from the slope. For the dichlorides it results 17 $cm^3\ mol^{-1}\ CH_2^{-1}$ and 17.5 $cm^3\ mol^{-1}\ CH_2^{-1}$ for $V_{\Phi,S}$ and $V_{\Phi,M}$, respectively, and a little greater for the dimethanesulfonates. In both cases, the group contribution to the change in volume upon micellization results 0.5 $cm^3\ mol^{-1}\ CH_2^{-1}$, a value lower than that generally accepted when the CH_2 group is added to the hydrophobic tail of the traditional hydrogenated surfactants[71], confirming the data proposed in the literature[74]. In the same way, using equations (16) and (17), we have processed the apparent molar adiabatic compressibility data (Figures 30 and 31). They show trends vs. m similar to those of volumes with a sharp increase at the cmc till a plateau value in the micellar region. The values of the apparent molar adiabatic compressibility in the micellar state ($K_{S,\Phi,M}$) are high and positive, because when micelles are formed, the stiff cavity formed by water molecules and surrounding the hydrophobic moiety of the molecule is destroyed and the electrostriction is reduced by the counterion binding to the micelle. The molar compressibility in micellar phase for the highly fluorinated surfactants under investigation is much higher than for gemini hydrogenated surfactants and increases with the spacer length in a linear way. A group contribution for the methylene group in the spacer equal to $+1.2 \times 10^{-3}\ cm^3\ bar^{-1}\ mol^{-1}$, independent from the counterions obtained. We have found, for a homologous series of gemini surfactants, double amphiphilic betaine ester derivatives[21], a group contribution for the CH_2 added to the hydrophobic tails, equal to $+0.94 \times 10^{-3}\ cm^3\ bar^{-1}\ mol^{-1}$. This value is very close to that reported in Ref.[74] ($0.97 \times 10^{-3}\ cm^3\ bar^{-1}\ mol^{-1}$), and to that obtained for some propanediyl-α,-ω-bis(dimethylalkylammonium bromide) gemini surfactants ($1.15 \times 10^{-3}\ cm^3\ bar^{-1}\ mol^{-1}$)[44]. This means that the effect of the methylene group on the isoentropic molar compressibility is the same, no matter if it is added to

the tail or to the spacer of the gemini surfactant. As said above, the values of $Ks_{,\Phi,S}$ were obtained from equation (17), because the cmcs of the fluorinated compounds are too low to allow accurate measurements below the cmc. The group contribution for each CH_2 group of $+5 \times 10^{-4}$ cm^3 bar^{-1} mol^{-1} is obtained, regardless of the counterion. It is generally accepted that the group contribution to the molar compressibility of the CH_2, when added to the hydrophobic tail, is negative and quite small at room temperature, due to the balance between the negative contribution of the increased density of water molecules around the cavity and the positive contribution of the cavity itself[21,46]. The CH_2 group, when added to spacer, plays a minor role in the total hydrophobicity of the molecule, as suggested from the trend of the cmc with the lengthening of the spacer. For the change in molar isoentropic compressibility upon micellization a CH_2 group contribution of $+8\times10^{-4}$ cm^3 bar^{-1} mol^{-1} is obtained, which is not affected by the counterion.

Biological properties

The use in gene therapy of *gemini* surfactants as non-viral vectors, has been proposed based on the possibility of taking advantage of their multiple cationic charge, necessary for binding and compacting DNA and of their superior surface activity[75-79]. DNA nanoparticles, in fact, are generally composed by specific cationic lipids to ensure efficient DNA condensation and cellular uptake of the complexes and by helper lipids such as dioleoylphosphatidylethanolamine (DOPE)[77].

Taking into account the above observations, we designed and characterized new *gemini* compounds having, as polar head, two pyridinium groups, bridged together by an aliphatic chain, assuming that the presence of two aromatic pyridinium rings could

enhance the interaction with DNA and that their ability of compacting and encapsulating DNA into nanoparticles could readily internalize it by cells. Moreover, the corresponding highly fluorinated gemini compounds have been synthesized and studied in the same experimental conditions of their hydrogenated counterparts to shed light on the effect of fluorination on biological properties of these dicationic surfactants.

As far as the hydrogenated compounds are considered, we measured the dilution enthalpies of the didodecyl compounds because the diexadecyl compounds have a too low cmc not allowing for an accurate determination in the premicellar region[44,68]. They show a very peculiar behavior as a function of the spacer length, never found before in literature, not allowing for the determination of a $–CH_2–$ group contribution when this group is added to the spacer. In fact, the curve of compound P16-4 lies under those of the compound P16-3 (with three carbon atoms spacer), and not below the latter as expected. This behavior, not affected by the counterion, suggests that something happens in the structure of the molecule in solution when the spacer is four carbon atoms long[44]. We interpreted this surprising behavior as evidence of a conformation change of the molecule caused by stacking interactions between the two pyridinium rings, mediated by the counterion and appearing at an optimum length of the spacer. It is interesting to understand if this different behavior outlined by the trend of apparent and partial molar enthalpies vs. concentration, affects also the biological properties of the surfactants. This has been done by studying their gene delivery ability. We expect that the compounds under investigations have to interact with the DNA, owing their double positive charges carried by their heterocyclic polar heads. Moreover, the aromatic nature of the polar heads could give rise to stacking interaction with DNA bases by intercalation.

DISCUSSION

For gene delivery studies we chose to use the compounds with alkyl chain of 16 carbon atoms, according with our previous experience on this subject[21]. It is reported that the biological activity of cationic surfactants increases with the chain length up to a critical point[80] and, with reference to the homologous series of alkanediyl-α,ω-bis(dimethylalkylammonium bromide), the term with two alkyl chains of 16 carbon atoms is generally the most biologically active[81].

The results of biological assays show that the compounds here studied are all able to interact specifically with the DNA, completely shifted at concentration above 50 μM. This is particularly true for P16-4 and P16-8, doing so at halved concentration. It is very surprising to compare the DNA condensation ability of the compounds under study. In fact, as shown in Figures 38 and 40, the addition of one methylene group in the spacer is sufficient to transform a compound unable to efficiently compact the DNA to a compound able to transform plasmid DNA in nanoparticles giving rise to transfection. Without thermodynamic data, it would be very difficult to understand this sudden change in behavior. Thermodynamic data suggest a change of the molecule's conformation when the spacer reaches a certain lenght. The molecule in solution doubles up, like a book, due to stacking interactions between the two pyridinium rings and to the hydrophobic interactions of the alkyl chains, independently on the counterion[44,68]. This arrangement is possible neither when the spacer is too short (2 or 3 carbon atoms), because of the lack of enough conformational freedom, nor when the spacer is too long, because the pyridinium rings are too far apart. In this way, P16-4 behaves like molecular tongs, able to grip the aromatic bases of the DNA or phosphate groups. The distance between two nucleotide residues of DNA is 0.34 nm: if the phosphate groups substitute the counterions between two aromatic rings, reducing the

electrostatic repulsion, the molecule could assume the stacked conformation suggested by thermodynamic data, with a medium distance between pyridinium rings much lower than that calculated in vacuum (0.81 nm) for the dications. Then, the hydrophobic interactions between the chains of the surfactants can cause the efficient formation of nanoparticles. When the length of the spacer increases, this arrangement becomes more difficult and the pyridinium rings are prone to interact with DNA sites far from each other. This explanation is supported also by AFM images. P16-8 is still able to form some less compact nanoparticles and to give rise to a little transfection, while the compound with spacer 12 carbon atoms long is not. In fact, the latter probably assumes an extended conformation in solution with the pyridinium ring far apart, moreover the hydrophobic interactions in solution could involve the spacer, and the positive polar heads interact with DNA bridging remote bases and so giving rise to bows, as shown in Figure 40**d**. In this way the structures formed are not enough compact to be able to penetrate in the cellular membrane, the first step of transfection. The coformulation with DOPE does not change considerably the gene delivery ability of the compounds.

EMSA data (Figure 36) of highly fluorinated analogs show that all the compounds under study are able to compact DNA starting from a N/P = 1/1 ratio, and so they can be used to obtain DNA nanoparticles. The interaction with DNA seems not hindered by the presence of fluorinated moieties, which are bound to the positive nitrogen through two $-CH_2-CH_2-$ groups (Figure 20), so that the positive charges interacting with the phosphate groups of DNA are in a hydrogenated environment. Results of the gene delivery experiments on RD-4 cells, the same cells used with the hydrogenated analogues, are reported in Figure 39 and in comparison with the hydrogenated analogues in Figure 44.

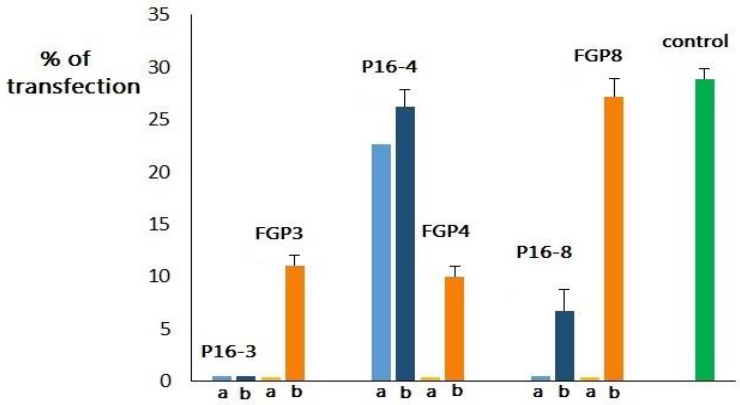

Figure 44. Comparison of the gene delivery ability between between partially fluorinated gemini surfactants FGP*n* in orange and hydrogenated gemini surfactants P16-*n* in blue: a) experiments done with only the surfactants (light colours) and by b) with surfactant:DOPE ratio 1:2 (dark colours). In green, positive control by the commercial reagent GenePORTER. Ref.[45].

In Figure 39 is clearly shown that DNA nanoparticles obtained by using the compounds under study alone are unable to deliver gene inside the cells. The situation changes if transfection experiments are carried out in presence of the helper lipid DOPE. This lipid enhances the transfection activity of cationic formulations through the stabilisation of DNA/lipid complex[57,58] and facilitates the transfer of DNA in the context of endosomal escape, owing to its fusogenic property and significantly affecting the polymorphic features of lipoplexes[59]. In presence of DOPE all the compounds, with the exception of FGP12, are able to deliver genes inside the cells, with an efficiency increasing in the order FGP4< FGP3<< FGP8, the last one giving rise to a transfection efficiency comparable to that of the commercial reference agent. This behavior could suggest that the fusogenic activity of DOPE helps to overcome the repulsion between the fluorinated DNA nanoparticles and the hydrogenated phospholipids constituting the cell membrane. The non-monotonic dependence on the spacer length is explained by two experimental facts: a) the trends of apparent and partial molar enthalpies vs. *m*; b) the AFM images.

The AFM images suggest that FGP8 (Figure 41**d**) is able to give rise to small, compact, and quite uniform DNA nanoparticles. DNA condensation by FGP3 gives rise to near spherical particles, greater than obtained with FGP8 but more compact than those made by FGP4. Nanoparticles obtained with FGP3 are able (Figure 44) to transfect about 12% of RD-4 cells when coformulated with the helper lipid. The fluorinated surfactant results more efficient in compacting DNA with respect to the hydrogenated one and give rise to smaller and more compact DNA nanoparticles. In fact, in Figure 44, it is interesting to note that the hydrogenated analogue P16-3 do not give rise to transfection neither without nor with DOPE. This finding is explained by the AFM results compared in Figure 45**a** and **b**. In Figure 45**c** and **d**, are also compared the DNA nanoparticles formed by P16-4 and FGP8, the most active in gene delivery of the two classes of compounds: both are able to completely compact DNA, but the objects obtained by FGP8 are smaller and uniform.

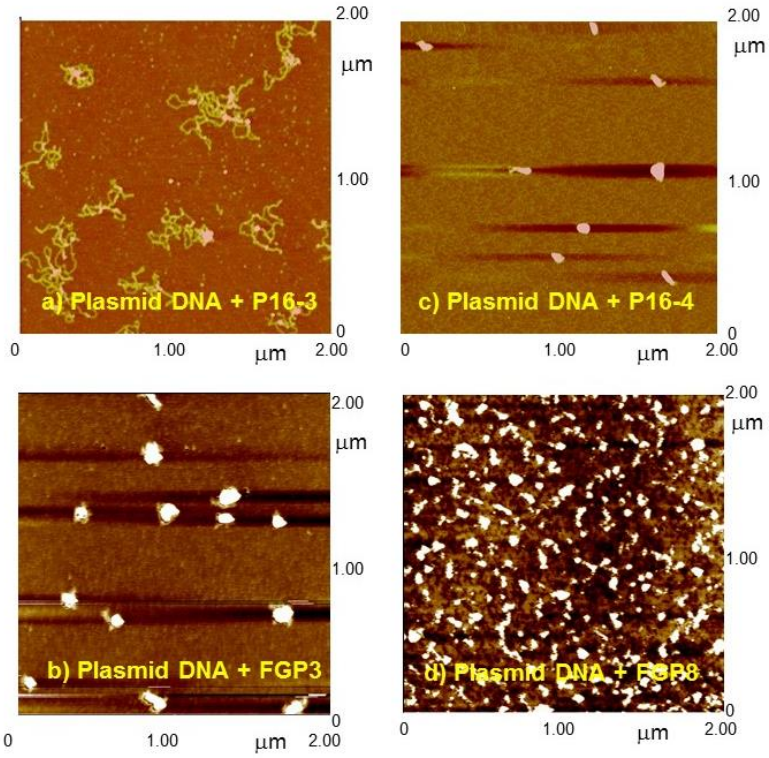

Figure 45. Comparison of AFM images of the structures obtained by the interaction of plasmid DNA with **a** | hydrogenated gemini P16-3; **b** | fluorinated FGP3; **c** | hydrogenated gemini P16-4 and **d** | fluorinated FGP4. Ref.[45].

According with the results we have suggested of the hydrogenated analogues that the compound with spacer formed by four carbon atoms is able to behave like a molecular tongs able to grip basic group near each other, thus allowing the formation of compact and near spherical DNA particles[66].

If the hydrophobic chain is modified by partial fluorination, a greater length of the spacer is needed for the molecular tongs formation, in perfect agreement with the trends shown by the curves of the apparent and partial molar enthalpies *vs. m* (Figures 26 and 27). This means that the conformation change in solution, determining the greatest gene delivery ability at a fixed spacer length, is principally due to the electronic structure of the pyridinium head groups. If the molecule is folded up in half so that the pyridinium

rings with their positive charge can face each other, they can bind the neighboring negatively charged groups of the DNA. Then, the interactions between the tails of the surfactants cause the efficient formation of nanoparticles. When the length of the spacer increases, this arrangement becomes more difficult and the positive pyridinium rings interact with negative DNA sites far from each other so giving rise to bows not suited for gene delivery, as shown in Figure 41**e**. In FGP3, the charged nitrogens are still enough near to give rise to nanoparticles, greater than with FGP8 and less efficient in transfection. FGP4, unlike of the corresponding hydrogenated, has still a spacer too short for an efficient conformational change, giving rise to a structures not compact enough.

Langmuir-Blodgett trough

FGP*n* were also preliminary tested using the Langmiur-Blodgett trough at different temperatures at the water-air and water-perfluorohexane (PFH) interfaces[80].

This study was performed during my period abroad at the Institut Charles Sadron (CNRS, University of Strasbourg), under the supervision of Professor Marie Pierre Krafft. The results obtained show that, at the water-air interface, FGP4 monolayer is not stable and it was not possible to record the isotherm for this compound (data not shown). On the other hand, FGP8 and FGP12 show a phase transition-like behavior at 25 °C, represented by the plateau region between 60 and 140 $Å^2$ (Figures 46 and 48).

Compound FGP12 present this plateau region also when the isotherm was recorded at 15, 35 and 45 °C.

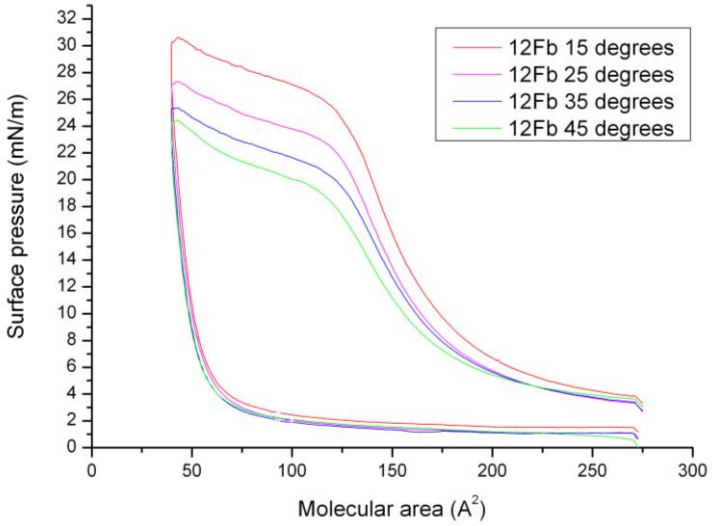

Figure 46. Compression-expansion isotherms of FGP12 (12Fb in the picture) at the water-air interface at different temperatures.

It could be observed that the compression–expansion curves decrease while decreasing the temperature and increase when the temperature is increased. The deposition of the monolayer at a pressure value of 25 mN/m, a pressure value in the plateau region, onto silicon wafer was used for an AFM investigation (Figure 47). The images obtained show that there is already a multilayer formation with particles of about 30 nm in diameter. This is correct accordingly with the observation that fluorinated surfactants give rise to micelles that are smaller than that of their hydrogenated counterpart.

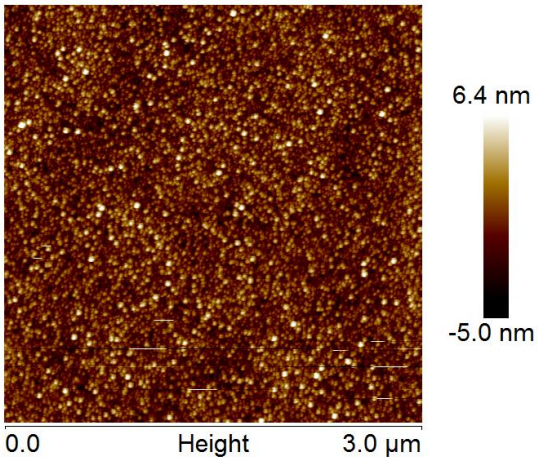

Figure 47. AFM image of FGP12 obtained with a deposition in the Langmuir-Blodgett trough at 25 mN/m.

Compound FGP8 presents a difference in the shape of the plateau region (Figure 48). The curves decrease of about 2 mN/m with a reduction and then the disappearing of the phase-transition while increasing the temperature. AFM image of this compound respect to that of FGP12 taken in the same isotherm position – in the plateau region-, give rise to smaller micelles of about 15 nm in diameter, accordingly to the reduced spacer (not shown).

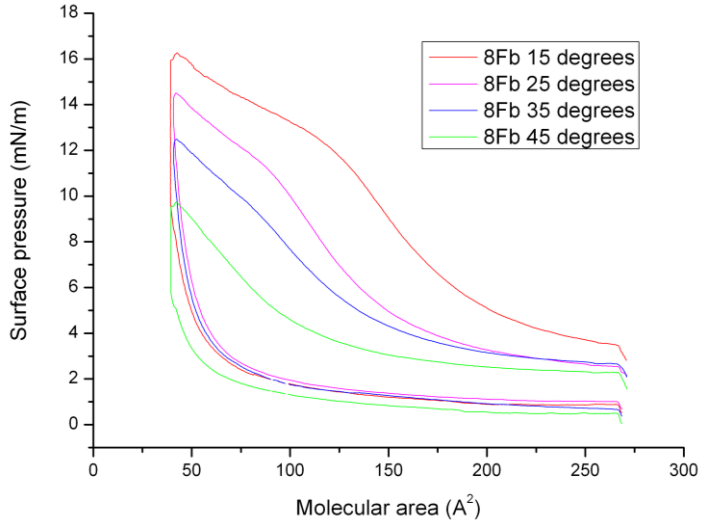

Figure 48. Compression-expansion isotherms of FGP8 (8Fb in the picture) at the water-air interface at different temperatures.

It is likely that gemini molecules arrange themselves at the water/air interface with the hydrophilic "head" in the water phase and the hydrophobic tails extended into the air. At the beginning the spacer is completely stretched out and, as the pressure increase, it starts to bend itself toward the air, as reported in Figure 49 below.

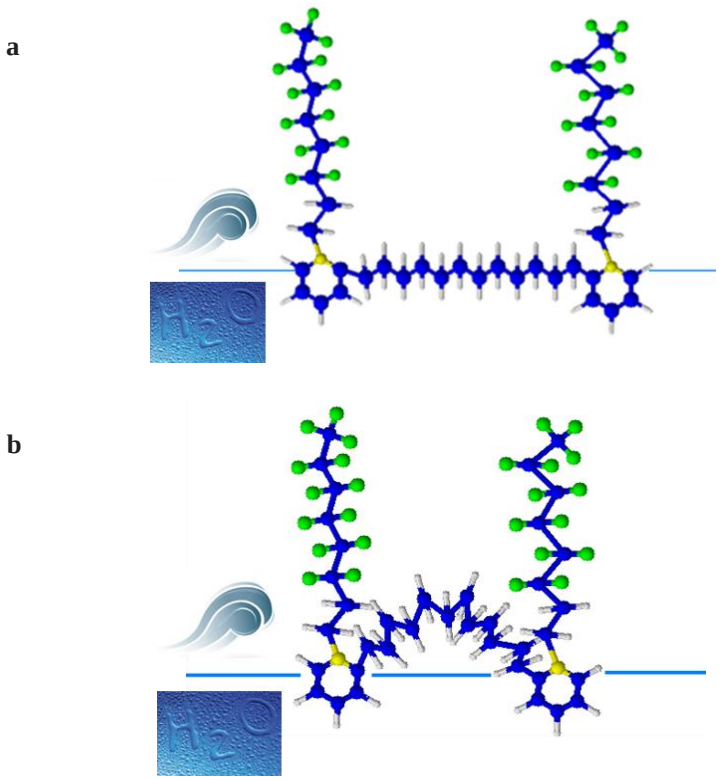

Figure 49. Hypothesized disposition of the molecule **a** | before and **b** | after compression at the water/air interface.

Of course, in the case of FGP8, the compressed structure is more tight than FGP12, due to the shorter spacer. This behavior was also tested at the interface between water and a N_2 flux saturated with perfluorohexane (PFH), obtained allowing the N_2 to bubble through three different vials filled with PFH solution.

The behavior of the curves for compound FGP12 at water-PFH interface are more or less the same of that obtained at the water-air interface, with an increase of the transition phase of roughly 3 mN/m for each isotherm for all the temperatures tested (Figure 50). In both cases, the molecular area reached is near to 56 $Å^2$, accordingly to the fact that the area covered by a single fluorinated chain is of ~ 30 $Å^2$.

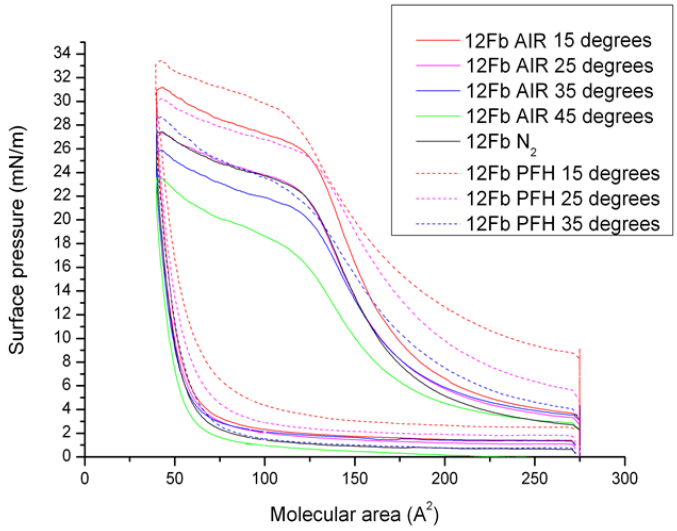

Figure 50. Superimposition of the compression-expansion isotherms of FGP12 (12Fb in the picture) at the water-air and at the water-PFH interfaces at different temperatures.

Also in the case of FGP8 the appearance of the plateau region, for all curves, is shifted at higher pressure values, with an increment of about 5-6 mN/m. At the water/air interface, this transition-like region disappeared from 35° C and above. It is worth noting that, in the presence of PFH, the plateau reappears at 35° C though is still not visible at 45° C (Figure 51).

The results obtained with PFH may be due to the insertion of the perfluoroalkane molecules into the surfactant monolayer spread onto the water surface, making the surfactant compression "delayed".

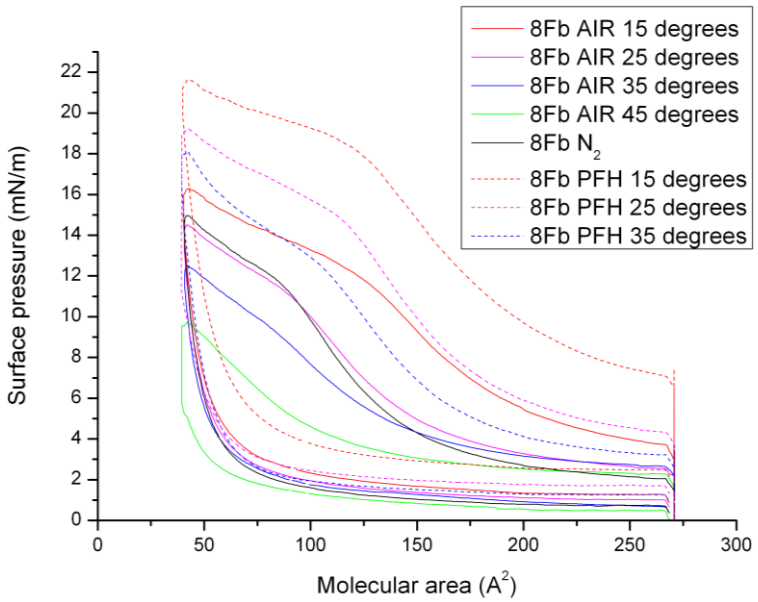

Figure 51. Superimposition of the compression-expansion isotherms of FGP8 (8Fb in the picture) at the water-air and at the water-PFH interfaces at different temperatures.

As previously said, a particular aspects of these kind of surfactants is their possible use as vectors to treat, for example, respiratory diseases such as cystic fibrosis. Fluorinated cationic lipids have been, in fact, proposed to obtain efficient gene expression in those biological fluids containing surfactants as pulmonary surfactants or bile salts when genes have to be delivered to the respiratory or biliary epithelium[66,75]. Theoretically speaking, fluorinated compounds are not dissolved by endogenous surfactants, preserving the loaded genetic material from degradation. At the same time, partially

fluorinated surfactants generally show low to moderate acute toxicity and low haemolytic activity compared to their hydrogenated analogues[81,82].

For this reason, during my stay in Strasbourg, I also started to investigate how the partially fluorinated surfactants under study insert themselves into a DPPC monolayer using the Langmuir-Blodgett trough (data not shown). This also because Professor Krafft has already conducted Langmuir studies[83] with a commercially available surfactants such as Curosurf (Chiesi Pharmaceutics) studying its interaction with a DPPC monolayer, also in the presence of fluorocarbon gases. The study needs further investigations.

5. CONCLUSIONS

CONCLUSIONS

The results here presented show that pyridinium *gemini* surfactant could be a valuable tool for gene delivery purposes. Their transfection activity and the structure of the DNA nanoparticles, as studied by AFM, are strictly related to their structure in solution, dependent on the spacer length and highlighted by the trends of the apparent and partial molar enthalpies *vs.* molality.

For the hydrogenated gemini surfactants, the compound with spacer formed by four carbon atoms, and, for the highly fluorinated ones, the compound with spacer formed by eight carbon atoms (FGP8), both showing unexpected enthalpic properties vs. concentration, gives rise to a transfection activity comparable to that of the commercial reagent, when formulated with DOPE.

We suggest that both the most efficient compounds behave like molecular tongs able to grip basic group near each other. The partial fluorination of the hydrophobic chains requires a greater length of the spacer for the folding of the molecule compared to the hydrogenated analogues. The reason lies both in the greater steric hindrance and rigidity of the fluorinated moiety, and in the repulsion between the hydrogenated and the fluorinated lipophobic tails. The compounds with the longest spacer give rise to loosely condensed structure by forming a sort of bows, not able to give rise to transfection notwithstanding the double positive charge of the molecule. The comparison with the hydrogenated analogues of FGP3, FGP4 and FGP8, reveals a greater ability of the partially fluorinated compounds to compact DNA. Solution thermodynamic studies, reported in the literature for the first time about this class of compounds, result in a very sensitive probe of the behavior of the molecule in solution, making “old” methods very useful for understanding “new” applications at molecular level.

CONCLUSIONS

The obtained results urge us to evaluate the effect of the length of the fluorinated chains in order to optimize the gene delivery ability and to study in deep of the toxicity and transfection ability on pulmonary cells of this class of compounds. In fact, it is accepted that fluorinated cationic lipids could be a sound option for efficient gene expression in biological fluids containing hydrogenated interfering surfactants, *e.g.* when genes have to be delivered to the respiratory or to the biliary epithelium[27,28,83-85]. This is an essential requirement, for instance, in the treatment of cystic fibrosis and cystic fibrosis-associated diseases[26]. Moreover, in many pulmonary conditions lung surfactants can be inactivated by serum proteins as a consequence of acute lung injury, giving rise to potentially serious consequences, as the acute respiratory distress syndrome[86]. Then the use of our fluorinated surfactants also in this field warrants further investigation.

6. REFERENCES

REFERENCES

[1] Strachan, T.; Read, A.P. Human molecular genetics. *Wiley-Liss*, Newyork., **1999**.

[2] Gloves, D.J.; Lipps, H.J. Towards safe non viral therapeutic gene expression in humans. *Nat Rev Genetics*., **2005**, *6*, 299-310.

[3] Ginn, S.L.; Alexander, I.E.; Edelstein, M.L.; Abedi, M.R.; Wixon, J. Gene therapy clinical trials worldwide to 2012 — an update. *J. Gene Med.*, **2013**, *15*, 65–77.

[4] Pack, D.W.; Hoffman, A.S.; Pun, S.; Stayton, P.S. Design and development of polymers for gene delivery. *Nature Rev. Drug Discov.*, **2005**, *4*, 581–593.

[5] Mintzer, M.A.; Simanek, E. E. Nonviral vectors for gene delivery. *Chem. Rev.*, **2009**, *109*, 259–302.

[6] Kawabata, K.; Takakura, Y.; Hashida, M. The fate of plasmid DNA after intravenous injection in mice: involvement of scavenger receptors in its hepatic uptake. *Pharm. Res.*, **1995**, *12*, 825–830.

[7] Li, W.; Szoka, F.C.Jr. Lipid-based nanoparticles for nucleic acid delivery. *Pharm. Res.*, **2007**, *24*, 438–449.

[8] Wiethoff, C.M.; Middaugh, C.R. Barriers to nonviral gene delivery. *J. Pharm. Sci.*, **2003**, *92*, 203–217.

[9] Morille, M.; Passirani, C.; Vonarbourg, A.; Clavreul, A.; Benoit, J.P. Progress in developing cationic vectors for non-viral systemic gene therapy against cancer. *Biomaterials*, **2008**, *29*, 3477–3496.

[10] Wasungu, L.; Hoekstra, D. Cationic lipids, lipoplexes and intracellular delivery of genes. *J. Control. Release*, **2006**, *116*, 255–264.

[11] Hao Yi; Kanasty, R.L.; Eltoukhy, A.A.; Vegas, A.J.; Dorkin, J.R.; Anderson, D.G. Non-viral vectors for gene-based therapy. *Nature Reviews Genetics*, **2014**, *15*, 541–555.

[12] Ahmed, T.; Kamel, A.O.; Wettig, S.D. Interactions between DNA and gemini surfactant: impact on gene therapy: part I, *Nanomedicine*, **2016**, *11*, 289-306.

[13] Thomas, C.E.; Ehrhardt, A.; Kay, M.A. Progress and problems with the use of viral vectors for gene therapy. *Nat. Rev. Genet*., **2003**, *4*, 346-358.

[14] Menger, F.M.; Littau, C.A. Gemini surfactants: a new class of self-assembling molecules. *J. Am. Chem. Soc*., **1993**, *115*, 10083–10090.

[15] Yi-Mei Zhang et al. Cationic gemini lipids with cyclen headgroups:interaction with DNA and gene delivery abilities. *RSC Adv*., **2014**, *4*, 44261.

[16] Sandra, G.; Silva, I.S.; Oliveira, M. et al. Serine-based gemini surfactants with different spacer linkages: from self-assembly to DNA compaction. *Soft Matter*, **2014**, *10*, 9352-9361.

[17] Zhang, S.; Xu, Y.; Wang, B.; Qiao, W.; Liu D.; Li, Z. Cationic compounds used in lipoplexes and polyplexes forgene delivery. *J. Controlled Release*, **2004**, *100*, 165–180.

[18] Pedroso De Lima, M.C.; Simoes, S.; Pires, P.; Faneca H.; Düzgünes¸ N. Cationic lipid-DNA complexes in gene delivery: from biophysics to biological applications. *Adv. Drug Delivery Rev*., **2001**, *47*, 277–294.

[19] Lonez, C.; Vandenbranden, M.; Ruysschaert, J.M. Cationic liposomal lipids: from gene carriers to cell signaling. *Prog. Lipid Res.*, **2008**, *47*, 340–347.

[20] Muhammad, S.K. A Review of Gemini Surfactants: Potential Application in Enhanced Oil Recovery. *J. Surfact. Deterg*., **2016**, *19*, 223-236.

[21] Fisicaro, E.; Compari, C.; Duce, E.; Donofrio, G.; Różycka- Roszak, B.; Woźniak, E. Biologically Active Bisquaternary Ammonium Chlorides: Physico-Chemical Properties of Long Chain Amphiphiles and Their Evaluation as Non-Viral Vectors for Gene Delivery. *Biochim. Biophys. Acta, Gen. Subj.*, **2005**, *1722*, 224−233.

[22] Krafft, M.P.; Riess, J.G. Chemistry, Physical Chemistry, and Uses of Molecular Fluorocarbon-Hydrocarbon Dibloks, Triblocks, and Related Compounds-Unique "Apolar" Components for Self-Assembled Colloids and Interface. *Engineering. Chem. Rev.*, **2009**, *109*, 1714-1792.

[23] Krafft, M.P.; Riess, J.G. Perfluorocarbons: Life Science and Biomedical Uses. *J. Polym. Sci. Pol. Chem.*, **2007**, *45*, 1185-1198.

[24] Krafft, M.P.; Riess, J.G. Selected Physicochemical Aspects of Poly- and Perfluoroalkylated Substances Relevant to Performance, Environment and Sustainability- Part One. *Chemosphere*, **2015**, *129*, 4-19.

[25] Riess, J.G. Higly Fluorinated Amphiphilic Molecules and Self-Assemblies with Biomedical Potential. *Curr. Opin. Colloid In*., **2009**, *14*, 294-304.

[26] Boulanger, C.; Di Giorgio, C.; Gaucheron, J.; Vierling, P. Transfection with fluorinated lipoplexes based on new fluorinated cationic lipids and in the presence of a bile salt surfactant. *Bioconjugate Chemistry*, **2004**, *15*, 901-908.

[27] Gaucheron, J.; Santaella, C.; Vierling, P. Improved in Vitro Gene Transfer Mediated by Fluorinated Lipoplexes in the Presence of a Bile Salt Surfactants. *J. Gen. Med.*, **2001**, *3*, 338-344.

[28] Courrier, H.M.; Pons, F.; Lessinger, J.M.; Frossard, N.; Krafft, M.P.; Vandamme, Th.F. In Vivo Evaluation of a Reverse Water-in-fluorocarbon Emulsion Stabilized with a Semifluorinated Amphiphile as a Drug Delivery System through the Pulmonary Route. *International Journal of Pharmaceutics*, **2004**, *282*, 131-140.

[29] Li, X.; Turanek, J.; Knoetigova, P.; Kudlackova, H.; Masek, J.; Pennington, D. B.; Rankin, S.E.; Knutson, B.L.; Lehmler, H.J. Synthesis and Biocompatibility Evaluation of Fluorinated, Single-tailed Glucopyranoside Surfactants. *New Journal of Chemistry*, **2008**, *32*, 2169-2179. Erratum in New Journal of Chemistry, **2009**, *33*, 2491-2493.

[30] Augusto, L.A. et al. Interaction of pulmonary surfactant protein C with CD14 and lipopolysaccharide. *Infect. Immun.*, **2003**, *71*, 61–67.

[31] Veldhuizen, E.J.A.; Haagsman, H.P. Role of pulmonary surfactant components in surface film formation and dynamics. *Biochimica et Biophysica Acta*, **2000**, *1467*, 255-270.

[32] Goerke, J.; Gonzales, J. Temperature dependence of dipalmitoyl phosphatidylcholine monolayer stability. *J. Appl. Physiol*., **1981**, *51*, 1108-1114.

[33] Griese, M. Pulmonary surfactant in health and human lung diseases: state of the art. *Eur. Respir. J*., **1999**, *13*, 1455-1476.

[34] Weaver, T.E.; Whitsett, J.A. Function and regulation of expression of pulmonary surfactant-associated proteins. *Biochem. J*., **1991**, *273*, 249-264.

[35] Notter, R.H. Lung Surfactants: Basic Science and Clinical Applications; *Marcel Dekker: New York*, **2000**.

[36] Avery, M.E.; Mead, J. Surface properties in relation to atelectasis and hyaline membrane disease. *Am. J. Dis. Child*., **1959**, *97*, 517-523.

[37] Lipowsky, R.; Sackmann, E. Structure and dynamics of membranes: from cells to vesicles. *Handbook of Biological Physics vol 1 (Amsterdam: Elsevier)*, **1995**.

[38] Quagliotto, P.; Viscardi, G.; Barolo, C.; Barni, E.; Bellinvia, S.; Fisicaro, E.; Compari, C. Gemini Pyridinium Surfactants: Synthesis and Conductimetric Study of a Novel Class of Amphiphiles. *J. Org. Chem*., **2003**, *68*, 7651−7660.

[39] Quagliotto, P; Barolo, C.; Barbero, N.; Barni, E.; Compari, C.; Fisicaro, E.; Viscardi, G. Synthesis and Characterization of Highly Fluorinated Gemini Pyridinium Surfactants. *Eur. J. Org. Chem*., **2009**, *19*, 3167-3177.

[40] Wanderlingh, U.; D'Angelo, G.; Conti Nibali, V.; Gonzalez, M.; Crupi, C.; Mondelli, C. Influence of gramicidin on the dynamics of DMPC studied by incoherent elastic neutron scattering, *J. Phys.: Condens. Matter*, **2008**, *20*, 104214.

[41] Zuidema, H.H.; Waters, G.W. Ring method for the determination of interfacial tension. *Ind. Eng. Chem. Anal. Ed.*, **1941**, *13*, 312-313.

[42] Desnoyers, J.E.; Perron, G. in: Surfactant Solutions - New Methods of Investigation, Ed. R. Zana, *Marcel Dekker, Inc., New York*, **1987**.

[43] Fisicaro, E.; Compari, C.; Duce, E.; Contestabili, C.; Quagliotto, P.; Viscardi, G. First evaluation of Thermodynamic Properties for Spheres to Elongated Micelles Transition of Some Propanediyl-α,ω-bis(dimethylalkylammonium bromide) Surfactants in Aqueous Solutions. *J. Phys. Chem. B*, **2005**, *109*, 1744-1749.

[44] Fisicaro, E.; Compari, C.; Bacciottini, F.; Barbero, N.; Viscardi, G.; Quagliotto, P.L. Is the Counterion Responsible for the Unusual Thermodynamic Behavior of the Aqueous Solutions of Gemini Bispyridinium Surfactants? *Colloids and Surfaces, A: Physicochemical and Engineering Aspects*, **2014**, *443*, 249-254.

[45] Fisicaro, E.; Compari, C.; Bacciottini, F.; Contardi, L.; Pongiluppi, E.; Barbero, N.; Viscardi, G.; Quagliotto, P.; Donofrio, G.; Krafft, M.P. Nonviral gene-delivery by highly fluorinated gemini bispyridinium surfactant-based DNA nanoparticles. *J. Coll. Interf. Sci.*, **2017**, *487*, 182-191.

[46] Fisicaro, E.; Contardi, L.; Compari, C.; Bacciottini, F.; Pongiluppi, E.; Viscardi, G.; Barbero, N.; Quagliotto, P.; Róztcka-Roszak, B. Solution thermodynamics of highly fluorinated gemini bispyridinium surfactants for biomedical

applications, *Colloids and Surfaces A: Physicochem. Eng. Aspects*, **2016**, *507*, 236–242.

[47] Wetting, S.D.; Verrall, R.E. Thermodynamic studies of aqueous m-s-m geminisurfactant systems. *J. Colloid Interface Sci*., **2001**, *235*, 310–316.

[48] De Lisi, R.; Milioto, S.; Verrall, R.E. Partial molar volumes and compressibilities of alkyltrimethylammonium bromides. *J. Solut. Chem*., **1990**, *19*, 665–692.

[49] Iqbal, M.; Verrall, R.E. Partial molar volumes and adiabatic compressibilities of glycyl peptides at 25° C. *J. Phys. Chem*., **1987**, *91*, 967–971.

[50] Chalikian, T.V.; Sarvazyan, A.P.; Breslauer, K. Partial molar volumes, expansibilities and compressibilities of α, ω-aminocarboxylic acids in aqueous solutions between 18 and 55° C. *J. Phys. Chem*., **1993**, *97*, 13017–13026.

[51] Lewis, G.N.; Randall, M. Thermodynamics, *Mc Graw-Hill, New York*, **1961**.

[52] Pérez, L.; Pinazo, A.; Rosen, M.J.; Infante, M.R. Surface activity properties at equilibrium of novel gemini cationic amphiphilic compounds from arginine, Bis(Args). *Langmuir*, **1998**, *14*, 2307-2315.

[53] Rosen, M.J. Surfactants and Interfacial Phenomena*;* second ed. *John Wiley & Sons: New York*, **1989**.

[54] Tsubone, K.; Arakawa, Y.; Rosen, M.J. Structural Effects on Surface and Micellar Properties of Alkanediyl-α,ω–bis(sodium N-acyl-β-alaninate) Gemini Surfactants. *J. Colloid Interface Sci.*, **2003**, *262*, 516-524.

[55] Li, Z.X.; Dong, C.C.; Thomas, R.K. Neutron reflectivity studies of the surface excess of gemini surfactants at the air water interface. *Langmuir*, **1999**, *15*, 4392-4396.

[56] Barbero, N.; Magistris, C.; Quagliotto, P.; Bonandini, L.; Barolo, C.; Buscaino, R.; Compari, C.; Contardi, L.; Fisicaro, E.; Viscardi, G. Synthesis and Physico-Chemical Characterization of Long Alkyl Chain Gemini Pyridinium Surfactants for Gene Delivery. *ChemPlusChem*, **2015**, *80*, 952-962.

[57] Liu, F.; Yang, J.; Huang, L.; Liu, D. Effect of Non-Ionic Surfactants on the Formation of DNA/Emulsion Complexes and Emulsion-Mediated Gene Transfer. *Pharm. Res*., **1996**, *13*, 1642−1646.

[58] Hara, T.; Liu, F.; Liu, D.; Huang, L. Emulsion Formulations as a Vector for Gene Delivery in Vitro and Vivo. *Adv. Drug Delivery Rev*. **1997**, *24*, 265−271.

[59] Chen, Y.; Lu, Y.; Tao, C.; Huang, J.; Zhang, H.; Yu, Y.; Zou, H.; Gao, J.; Zhong, Y. Complexes Containing Cationic and Anionic pH Sensitive Liposomes: Comparative Study of Factors Influencing Plasmid DNA Gene Delivery to Tumors. *Int. J. Nanomed*., **2013**, *8*, 1573−1593.

[60] Bustamante, C.; Rivetti, C. Visualizing Protein-Nucleic Acid Interactions on a Large Scale with the Scanning Force Microscope. *Annu. Rev. Biophys. Biomol. Struct*., **1996**, *25*, 395−429.

[61] Hansma, H.G. Surface Biology of DNA by Atomic Force Microscopy. *Annu. Rev. Phys. Chem*., **2001**, *52*, 71−92.

[62] Senapati, S.; Lindsay, S. Recent Progress in Molecular Recognition Imaging Using Atomic Force Microscopy. *Accounts of Chemical Research*, **2016**, *49*, 503-510.

[63] Zou, Y.; Oupicky, D.; Mao, G. Atomic Force Microscopy Imaging of DNA Delivery Nanosystems. *NanoCellBiology* Edited by Jena, B.P.; Taatjes, D.J., **2014**, 321-340.

[64] Volcke, C.; Pirotton, S.; Grandfils, C.; Humbert, C.; Thiry, P.A.; Ydens, I.; Dubois, P.; Raes, M. Influence of DNA Condensation State on Transfection Efficiency in DNA/Polymer Complexes: An AFM and DLS Comparative Study. *J. Biotechnol*., **2006**, *125*, 11−21.

[65] Ceci, P.; Cellai, S.; Falvo, E.; Rivetti, C.; Rossi, G.L.; Chiancone, E. DNA Condensation and Self-Aggregation of Escherichia coli Dps Are Coupled Phenomena Related to the Properties of the NTerminus. *Nucleic Acids Res.*, **2004**, *32*, 5935−5944.

[66] Fisicaro, E.; Compari, C.; Bacciottini, F.; Contardi, L.; Barbero, N.; Viscardi, G.; Quagliotto, P.; Donofrio, G.; Różycka-Roszak, B.; Misiak, P.; Woźniak, E.; Sansone, F. Nonviral Gene-Delivery: Gemini Bispyridinium Surfactant-Based DNA Nanoparticles. *J. Phys. Chem. B*, **2014**, *118*, 13183-13191.

[67] Rivetti, C.; Guthold, M.; Bustamante, C. Scanning face microscopy of DNA deposited onto mica: equilibration versus kinetic trapping studied by statistical polymer chain analysis. *J. Mol. Biol.*, **1996**, *264*, 919-932.

[68] Fisicaro, E.; Compari, C.; Biemmi, M.; Duce, E.; Peroni, M.; Barbero, N.; Viscardi, G.; Quagliotto, P.L. The Unusual Behaviour of the Aqueous Solutions of Gemini Bispyridinium Surfactants: Apparent and Partial Molar Enthalpies of the Dimethanesulfonate. *J. Phys. Chem. B,* **2008**, *112*, 12312-12317.

[69] Fisicaro, E.; Pelizzetti, E.; Bongiovanni, R.; Borgarello, E. Perfluorinated surfactants: properties and applications. I. Thermodynamic properties. *Colloids Surf.*, **1990**, *48*, 259-275.

[70] Fisicaro, E.; Pelizzetti, E.; Viscardi, G.; Quagliotto, P.; Trossarelli, L. Thermodynamic Properties of Aqueous Micellar Solutions of N-(1H,1H,2H,2H Perfluoro-Octyl) Pyridinium Chloride and N-(1H,1H,2H,2H Perfluoro-Decyl) Pyridinium Chloride. *Colloids and Surfaces A: Physicochem. Eng. Aspects*, **1994**, *84*, 59-70.

[71] Fisicaro, E.; Ghiozzi, A.; Pelizzetti, E.; Viscardi, G.; Quagliotto, P. Effect of the Counterion on Thermodynamic Properties of Aqueous Micellar Solutions of 1-(3, 3, 4, 4, 5, 5, 6, 6, 6-nonafluorohexyl) Pyridinium Halides. Part I: Apparent and Partial Molar Enthalpies and Volumes at 298 K. *J. Colloid Interface Sci.*, **1996**, *182*, 549-557.

[72] Tamaki, K.; Ohara, Y.; Watanabe, S. Solution properties of sodium perfluoroalkanoates, heats of solution, viscosity B coefficients and surface tensions. *Bull. Chem. Soc. Jpn*, **1982**, *62*, 2497-2501.

[73] Tamaki, K.; Watanabe, S.; Daikyoji, Y. Partial molar volumes of sodium perfluoroalkanoates and lithium perfluoro-1-alkanesulfonates in aqueous solutions. *Bull. Chem. Soc. Jpn*, **1990**, *63*, 3681-3682.

[74] DeLisi, R.; Ostiguy, C.; Perron, G.; Desnoyers, J.E. Complete thermodynamics properties of nonyl- and decyltrimethylammonium bromides in water. *J. Coll. Interf. Sci.*, **1979**, *71*, 147-166.

[75] Sharma, V.D.; Ilies, M.A. Heterocyclic Cationic Gemini Surfactants: A Comparative Overview of Their Synthesis, Self-Assembling, Physicochemical, and Biological Properties. *Med. Res. Rev*., **2014**, *34*, 1−44.

[76] Yang, P.; Singh, J.; Wettig, S.; Foldvari, M.; Verrall, R.E.; Badea, I. Enhanced Gene Expression in Epithelial Cells Transfected with Amino Acid-Substituted Gemini Nanoparticles. *Eur. J. Pharm. Biopharm*., **2010**, *75*, 311−320.

[77] Sing, J.; Michel, D.; Chitanda, J.M.; Verral, R.; Badea, I. Evaluation of Cellular Uptake and Intracellular Trafficking as Determining Factors of Gene Expression for Amino Acid-substituted Gemini Surfactant-Based DNA Nanoparticles. *J. Nanobiotechnol*., **2012**, *10*, 1−14.

[78] Donkuru, M.D.; Badea, I.; Wettig, S.; Verrall, E.; Elsabahy, M.; Foldvari, M. Advancing Nonviral Gene Delivery: Lipid- and Surfactant-Based Nanoparticle Design Strategies. *Nanomedicine*, **2010**, *5*, 1103−1127.

[79] Sharma, V.D.; Lees, J.; Hoffman, N.E.; Brailoiu, E.; Madesh, M.; Wunder, S.L.; Ilies, M.A. Modulation of Pyridinium Cationic Lipid-DNA Complex Properties by Pyridinium Gemini Surfactants and Its Impact on Lipoplex Transfection Properties. *Mol. Pharmaceutics*, **2014**, *11*, 545−559.

[80] Krafft, M.P.; Contardi, L.; Fisicaro, E.; Compari, C. manuscript in writing.

[81] Donkuru, McD.; Wettig, S.D.; Verrall, R.E.; Badea, I.; Foldvari, M. Designing pH-Sensitive Gemini Nanoparticles for Non-Viral Gene Delivery Intokeratinocytes. *J. Mater. Chem*. **2012**, *22*, 232−6244.

[82] Badea, I.; Shaterian, N.; Foldvari, M. Topical Gene Delivery in Mice Using Gemini surfactant Lipid Nanoparticles with and without Tape Electrode Electroporation. *Drug Delivery Lett*., **2011**, *1*, 62−66.

[83] Gerber, F.; Krafft, M.P.; Vandamme, T.F.; Goldmann, M.; Fontaine, P. Fluidization of a dipalmitoylphosphatidylcholine monolayer by fluorocarbon gases: potential use in lung surfactant therapy. *Biophysical Journal*, **2006**, *90*, 3184-3192.

[84] Raczka, E.; Kukowska-Latallo, J.F.; Rymaszewski, M.; Chen, C.; Baker Jr, J.R. The effect of synthetic surfactant Exosurf on gene transfer in mouse lung in vivo. *Gene Ther*., **1998**, *5*, 1333–1339.

[85] Gaucheron, J.; Santaella, C.; Vierling, P. Highly fluorinated lipospermines for gene transfer: synthesis and evaluation of their in vitro transfection efficiency. *Bioconjug. Chem*., **2001**, *12*, 114–128.

[86] Krafft, M.P. Overcoming inactivation of the lung surfactant by serum proteins: a potential role for fluorocarbons? *Soft Matter*, **2015**, *11*, 5982–5994.

PART 2:

POTENTIAL METAL-ENZYMES INHIBITORS

Chapter II

Metal/ligand interaction in potentially antiviral systems

1. INTRODUCTION

INTRODUCTION

Many metal ions play a vital role in biological functions in humans (e.g. sodium, potassium, magnesium, calcium, iron, zinc, copper, manganese, chromium, molybdenum and selenium) and currently many metal-based compounds or salts are routinely administered to patients for therapeutic and diagnostic purposes. Essential metal nutrients are supplied as dietary supplements to overcome deficiencies; otherwise metals are removed *via* chelation in the case of overload[1]. A large number of human diseases are caused by disorders of metal homeostasis and bioavailability. Nowadays, an ever-increasing number of metal-based drugs containing a broad spectrum of metals is available, most of them, not essential for humans, are able to target proteins and/or DNA. From the discovery of cisplatin, still used against specific types of cancer, a great variety of metal based anticancer drugs has been designed and studied[2]. Transition metal coordination complexes are also employed in medicine. For example, gold complexes have been extensively investigated as antibiotic, antiarthritic and anti-cancer agents, bismuth complexes as potent metalloenzyme inhibitors, anti-diarrheals and anti-bacterials, ruthenium complexes have been shown to exhibit highly encouraging anti-cancer activity, vanadium sulphate is being investigated in diabetes research as a potential alternative to insulin in type II diabetes[1-6]. More recently, metal coordination complexes have been employed in molecular recognition of biological substrates[7], specifically as protein biosensors and as inhibitors of protein complexation events and of biological functions.

The research group I'm working with, is involved in the study of many classes of potential antiviral molecules and of their mechanism of action, both against the human immunodeficiency virus type 1 (HIV-1) and against human influenza A or B virus. The devised strategy is to chelate the metal ions present in the active site of the HIV-1

Integrase (HIV-1 IN) or of the influenza endonuclease, so as to prevent viral replication. In fact, many molecules carry out their therapeutic action because they are able to bind the metal in the metal-enzyme active site. Magnesium ion, for instance, is an essential cofactor for several enzymes such as polymerases, ribonucleases, transportases and integrases and also in many processes involving formation and modification of phosphate chains. Understanding the mechanism of action of the inhibitors that act by chelating magnesium is therefore of great importance in order to develop new antiviral drugs. Development of potent inhibitors requires optimizing the binding affinity to the target, which is dictated by the binding free energy composed of both enthalpic and entropic contributions. The structure-based drug design enormously benefits from thermodynamic profiles, which provide information on the driving forces for binding.

For some years we have been studying new HIV-1 integrase inhibitors[8-11]. HIV-1 integrase (IN) catalyzes the integration of proviral cDNA into the host cell genome; it is an essential enzyme for viral replication[8-14] and a validated target for the development of drugs against HIV[15-17]. Several Integrase inhibitors were identified through in vitro inhibition assays with recombinant IN[18-23], and among them the diketoacid (DKA, Figure 52) class of compounds[24-26] showed the most promising derivatives[1].

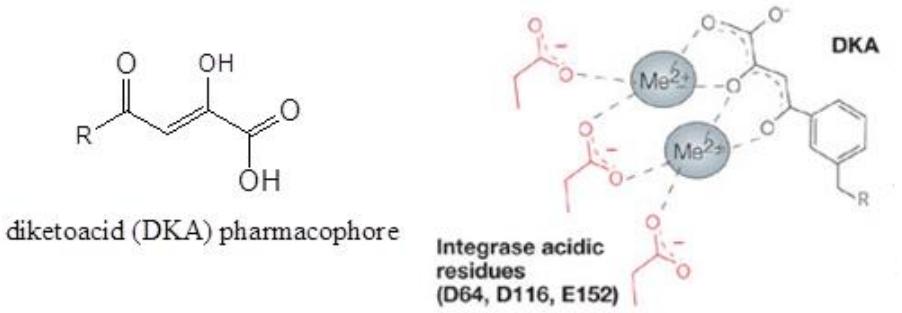

Figure 52. DKA pharmacophore (left) and the scheme of its mode of action (right). Ref.[1].

DKA-based MK-0518 (Raltegravir) and the 4-quinolone-3-carboxylic acid GS-9137 (Elviltegravir) (Figure 53) have been allowed by FDA for clinical use, confirming Integrase as a rational retroviral drug target[1,27-31].

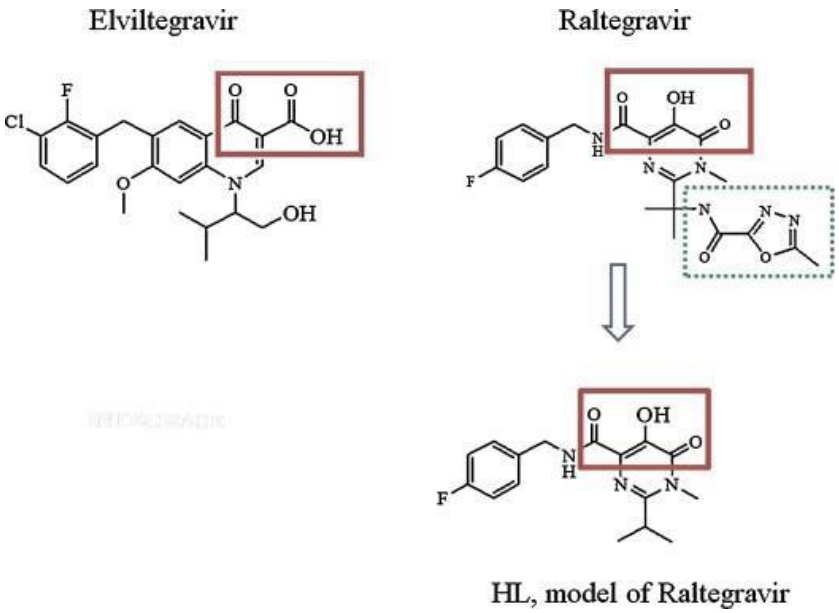

Figure 53. Schemes of the antiretroviral drugs Elvitegravir and Raltegravir, and of the model ligand N-(4-fluorobenzyl)-5-hydroxy-2-isopropyl-1-methyl-6-oxo-1,6-dihydroxypyrimidine-4-carboxylate, HL, synthesized by the Chemistry Department of the University of Parma. Ref.[1].

Influenza virus

Influenza virus (Figure 54) is an enveloped virus with a segmented negative-oriented single-stranded RNA genome, belonging to the *Orthomyxoviridae*[32].

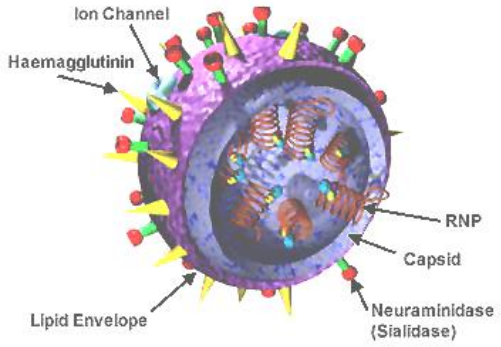

Figure 54. Influenza virus. [From: http://www.niaid.nih.gov NIAID, picture of public domain from National Institute of Health and Human Services].

Seasonal human influenza A or B virus infections are an important cause of morbidity and mortality, particularly in children and elderly, chronically ill or immunocompromised individuals,[33] and there is a permanent risk of sudden influenza pandemics, such as the notorious 'Spanish flu' in 1918[34] and the swine-origin H1N1 pandemic in 2009[35] Influenza vaccination is the most widely used prophylactic measure; moreover, two classes of anti-influenza virus drugs are available, acting on the viral M2 ion-channel (amantadine and rimantadine) or on viral neuraminidase (zanamivir and oseltamivir). The M2 inhibitors have limited clinical utility due to their central nervous system side effects and resistance is a growing concern for both M2 inhibitors and oseltamivir[36-40]. Therefore, there is an urgent need for antiviral compounds with novel pharmacophores and a different mode of action[41].

The influenza virus polymerase is widely recognized as an attractive target for antiviral drug development; inhibition of the PA endonuclease, in particular, has deserved much attention in recent years[42,43]. The influenza virus polymerase complex (Figure 55) is composed of three subunits: PB1, PB2 and PA[44,45].

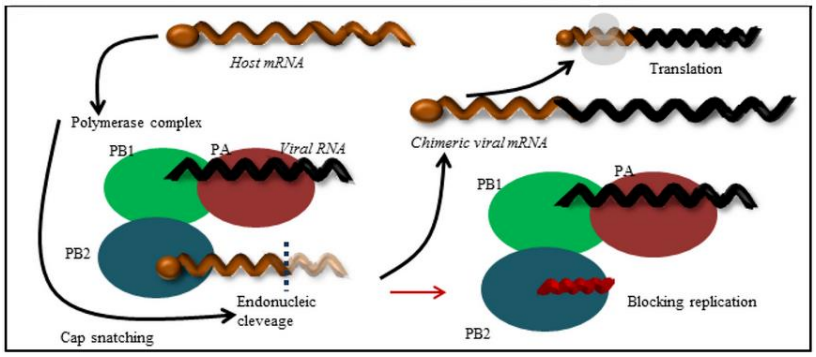

Figure 55. Mechanism of action of the influenza virus polymerase complex. [*Viruses*, **2015**, *7*(10), 5428-5442; doi:10.3390/v7102883].

The PA subunit performs the 'cap-snatching' endonuclease reaction, the PB2 subunit is responsible for initial binding of the capped RNAs, while the actual RNA synthesis is performed by the PB1 protein. The endonuclease catalytic site resides in the N-terminal domain of PA (PA-Nter)[45-47]. It comprises a histidine (His41) and a cluster of three strictly conserved acidic residues (Glu80, Asp108, Glu119), which coordinate (together with Ile120) one[47], two[48], or three[49] manganese or magnesium ions. The two-metal-ion model is consistent with numerous biochemical findings[50]. Since the intracellular concentration of free Mg^{2+} is at least 1000-fold higher than that of Mn^{2+}, magnesium may be more biologically relevant[51,52]. As in the case of HIV-1 integrase[53,54] several PA-binding agents with metal-chelating properties have been identified as influenza endonuclease inhibitors, including 2,4-dioxobutanoic acid derivatives[55,56], flutimide and its derivatives[56], as well as tetramic acids[57], 5-hydroxypyrimidin-4-one

derivatives and others. The common pharmacophoric motif of these inhibitors, is likely responsible for functional sequestration of the metal ions in the catalytic site of PA-Nter[1].

In recent years, the research group I'm working with, focused the attention on the research of chemical scaffolds able to chelate metal ions of PA-Nter, resulting in inhibition of influenza virus replication[58,59], taking in mind the functional similarity between the active sites of HIV-IN and PA-Nter. Accordingly, we focused our attention on two classes of molecules, previously tested as HIV IN inhibitors[60], containing the salicylic and the hydrazonic group (Figure 57). These molecules are chelating inhibitors with different coordinating ability, since they can chelate only one or up to two divalent metal ions. Previous study[58], demonstrated the metal complexing ability of 2-hydroxyamide-based scaffolds towards the metal cofactor: all three salicylamidic ligands (GR26, GR28, and GR30**)** are able to chelate Mg^{2+} ions, but form complexes with different stoichiometric ratios (Figure 56).

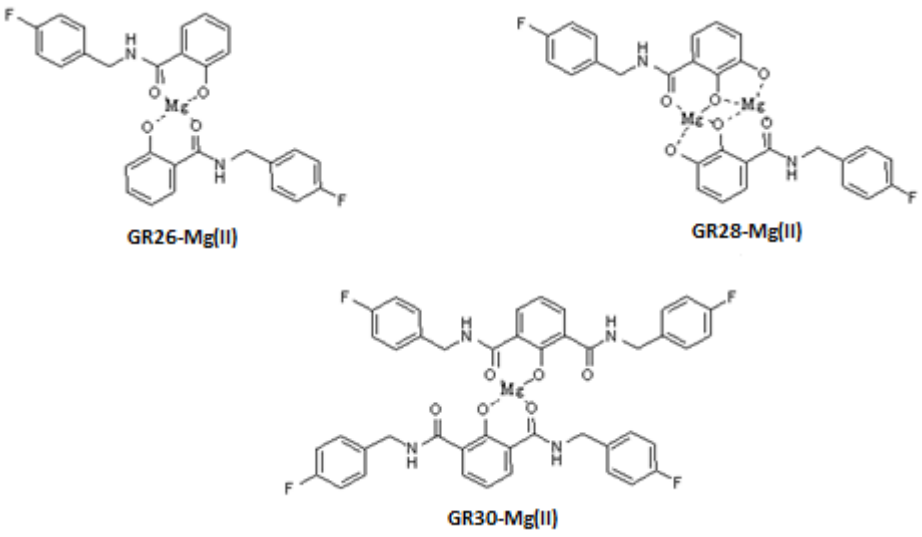

Figure 56. Complexes formed by salicylamidic derivatives with Mg(II).

The metal-chelation ability is employable for the development of promising inhibitors of a wide range of metal-enzymes of biological and pharmaceutical interest. In this thesis it is evaluated the interaction of these two classes of molecules under study with Mg(II), a representative of the class of "*hard*" metal ions, and Cu(II), a "*soft*" metal ion, as defined following the Pearson's classification of metal ions[61].

As previously said, Magnesium, an alkaline earth metal, is a cofactor in more than 300 enzymes. This metal is one of the most abundant element by mass in the human body that regulate different biochemical reactions including protein synthesis, muscle and nerve functions, blood glucose control, and blood pressure regulation[62]. Many viral metal-enzymes require Magnesium ions to function: in fact, Mg(II) ions are found to be present in the active site, for example, of the Integrase enzyme of the Human Immunodeficiency Virus (HIV IN) and Influenza Endonuclease.

On the other hand, Copper is a transition metal present in different concentrations throughout nature at both elemental state and salts. Copper ion possesses antimicrobial properties that allows it to destroy many microorganisms, e.g. Adenovirus and Influenza A virus. As one of the most important essential transition metals, Copper is involved in many biological processes such as blood red cells and connective tissue formation, bone, brain and heart growth, glucose and cholesterol metabolism and skin pigmentation.

2. EXPERIMENTAL SECTION

2.1 Materials

The study was conducted on two different classes of molecules: salicylamides and hydrazones derivatives, synthesized by the research group of Professor Carcelli from the University of Parma Chemistry Department.

a | Salicylamides derivatives

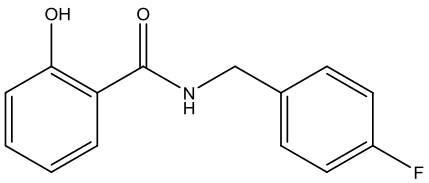

GR26
(MW = 264.26 g/mol)

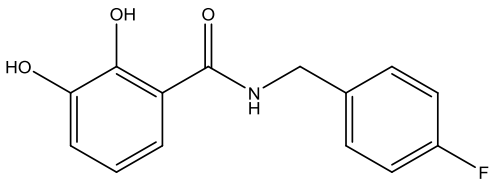

GR28
(MW = 261.26 g/mol)

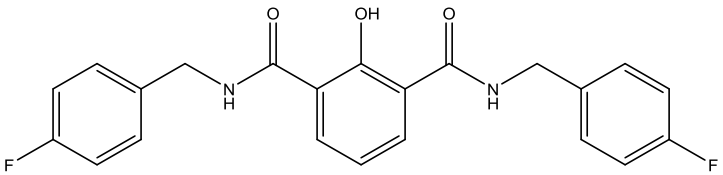

GR30
(MW = 396.39 g/mol)

b | Hydrazones- derivatives

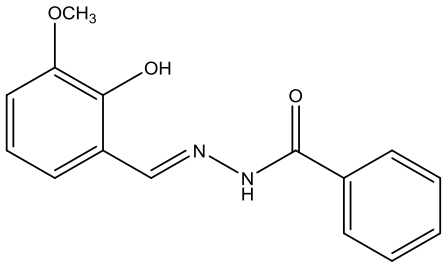

GR31
(MW = 270.27 g/mol)

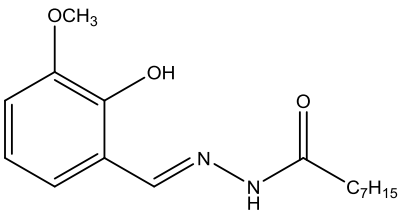

GR55
(MW = 292.38 g/mol)

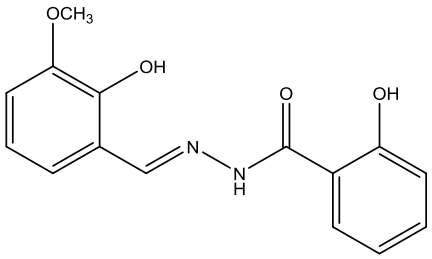

DR31
(MW = 286.28 g/mol)

Figure 57. Structure of the compounds under investigation. **a** | Salicylamides- and **b** | hydrazones- derivatives and their Molecular Weight (MW).

The concentration of the Mg(II) stock solution, prepared from $MgCl_2 \cdot 6H_2O$ (Merck), was determined by using EDTA as a titrant in the presence of NH_3/NH_4Cl buffer, using Eriochrome Black T as indicator. The concentration of the Cu(II) stock solution, prepared from $CuCl_2 \cdot 2H_2O$ (Merck), was also determined by using EDTA as a titrant in the presence of concentrated ammonia using Fast Sulfon Black as indicator.

Freshly boiled doubly distilled water, stored under nitrogen (N_2), was used throughout. Doubly distilled methanol was boiled and stored in CO_2-free conditions. Hydrochloric acid (HCl, *ca.* 0.2 M) and potassium hydroxide solution (KOH, *ca.* 0.1 M) were prepared by diluting the content of Merck Titrisol ampoules with the proper quantity of water and methanol to achieve methanol:water ratio of 9:1 v/v. The potassium hydroxide solution was standardized with potassium phthalate acid (C. Erba; dried at 120 °C).

2.2 Methods

- *Potentiometric titrations*

Potentiometric titrations were used to determine the Equilibrium constant for protonation and complexation in methanol:water = 9:1 v/v solution at ionic strength of 0.1 M KCl. The titrations were carried out under nitrogen in the pH range 2.5-11 by a fully automated apparatus equipped with a CRISON GLP 21-22 digital voltmeter (resolution 0.1 mV) and a 5 ml Metrohm Dosimat 655 autoburet, and controlled by a homemade software in BASIC, working on a IBM computer (Figure 58).

Temperature (25 ± 0.1°C) was controlled to ± 0.1°C by using a thermostatic circulating water bath (ISCOGTR 2000 IIx).

Figure 58. The autoburet, the cell and the pHmeter.

The electrodic chain (Crison 5250 glass electrode and 0.1 M KCl in methanol:water = 9:1 v/v calomel electrode, Radiometer 401) was calibrated in terms of $[H^+]$ by means of

a strong acid – strong base titration by Gran's method[63] allowing for the determination of the standard potential, E° (371.5 ± 0.4 mV), and of the ionic product of water, K_w (pK_w = 14.40 ± 0.05).

The data obtained were processed using the GRAPPLE program that process the data according to the Gran method or, optionally, the Nernst equation to linearize the titration curve. We have chosen to use the Gran plot, and the program linearize the curve by a least-squares fit and determines the values and the relative standard deviations of the parameters E_0, the standard potential of the electrode chain, K_w^*, the water ionic product, the acidic and basic equivalence volumes and the difference between the two values.

The pre-treatment and storage of methanol, as described in the experimental section, appears to be absolutely necessary if good linearity of the Gran plot has to be obtained. During the whole strong acid- strong base titration, the methanol:water ratio must be kept perfectly constant to ensure constancy of the junction potentials, activity coefficients[64] and $K_w^{*\prime}$, the operational ionic product of water in the mixed solvent used. This means that the titrants and the solution in the potentiometric cell, must be prepared in the same solvent. In fact, the titration performed using an aqueous potassium hydroxide solution without pre-treatment of the methanol, the Gran plot is non-linear in the acid region[65], as shown in Figure 59.

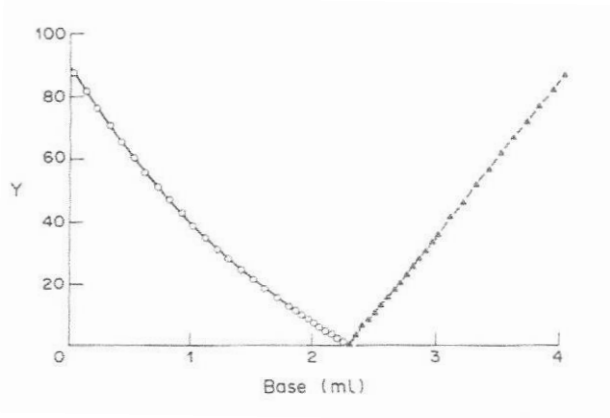

Figure 59. Gran plot for a strong acid-strong base titration in 9:1 v/v methanol:water with a saturated KCl/calomel reference electrode and KOH as titrant, without pre-treatment of methanol. Picture from Ref.[65].

As the mandatory steps above mentioned were fulfilled, the use of a saturated KCl/calomel electrode gave a Gran plot like that shown in Figure 60**a**: in the alkaline region the plot shows two branches with different slopes after the equivalent point. This could be ascribed to the potassium chloride precipitation at the liquid junction between the mixed solvent and the aqueous saturated KCl solution in the reference electrode, resulting in a sudden variation of the liquid-junction potential[65]. The use of a 0.1M solution of potassium chloride in methanol:water = 9:1 (v/v) in the calomel electrode overcomes this difficulty and results in a Gran plot like that reported in Figure 60**b**.

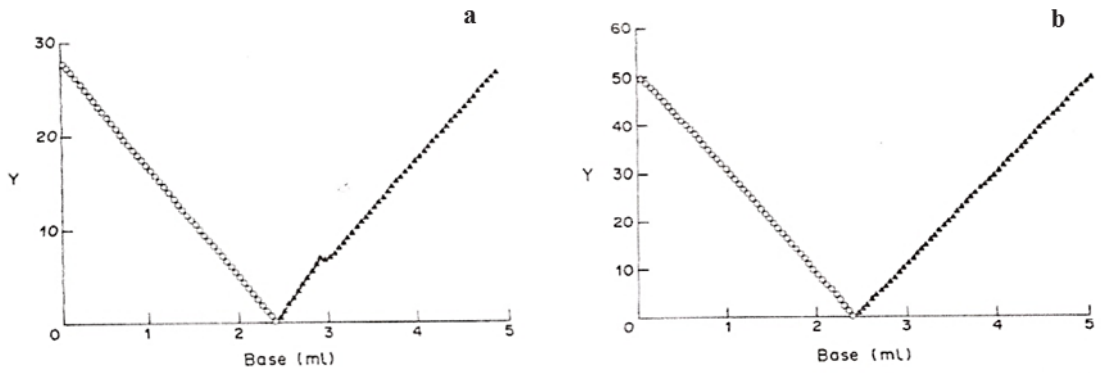

Figure 60. Gran plot for a strong acid-stong base titration in 9:1 v/v methanol:water with **a** | a commercial aqueous saturated KCl/calomel reference electrode, and **b** | a 0.1M KCl/calomel reference electrode filled with a 9:1 v/v methanol:water solution. Picture from Ref.[66].

The ligand solutions, prepared by weight, were titrated with standard KOH (methanol:water = 9:1 v/v, I = 0.1 M KCl) with and without metal ions. A constant speed magnetic stirring was applied during the entire titration. Double-distilled water and freshly boiled methanol, stored under nitrogen, were used throughout. The experimental procedure to reach high accuracy in the determination of the equilibrium constants in this mixed solvent has been described in detail elsewhere[65]. The protonation constants of the compounds under investigation (Tables 17 and 20) were obtained by titrating 20 ml of samples of each ligand (3×10^{-3} M). Titrations in different ligand/metal ratios (from 1 up to 4) were performed in order to obtain the complex formation constants. At least two measurements were performed for each system. The software HYPERQUAD[66] was used to obtain the speciation and the logarithm of the stability constants ($\log \beta_{pqr}$) from titration data. $\beta_{pqr} = [M_pL_qH_r]/[M]^p[L]^q[H]^r$ is the cumulative formation constant for the equilibrium reaction $pM + qL + rH = M_pL_qH_r$, in which M indicates the metal, L the completely deprotonated ligand and H the proton. Charges are omitted for simplicity.

- *Isothermal Titration Calorimetric (ITC) studies*

ITC measurements were carried out on a CSC model 5300 N-ITC III isothermal titration calorimeter (Calorimetry Sciences Corporations, USA) at 25 °C (Figure 61). KOH solution (0.065–0.145 M) in methanol:water = 9:1 (v/v) at 0.1 M KCl ionic strength was injected in steps of 5 μL into a 960 μL reaction cell by a 250 μL syringe with an interval of 400-500 s between two successive injections with stirring speed of 150 revolutions per minute (rpm).

To obtain the protonation heat of the ligand, the cell was filled up with a solution of methanol:water = 9:1 at 0.1 M KCl ionic strength containing only the ligand. Dilution heats were subtracted by carrying out blank experiments, in which the KOH solution was injected into the same solvent, without ligand. The molar enthalpy change for the reaction $H^+ + OH^- = H_2O$ has been obtained by titrating a solution of HCl with KOH, both prepared in the mixed solvent (methanol:water = 9:1 v/v, I = 0.1 M KCl). It results -20.6 ±0.4 kJ mol^{-1} [1]. The experimental peaks were integrated and corrected for the dilution heats by the NanoAnalyze (TA Instrument) software. The resulting data were elaborated by the HypΔH software[1,67], assuming the protonation constants from potentiometric measurements.

Figure 61. The calorimeter CSC 5300 nITC III at the Interdepartmental Measuring Center *"Casnati"* at the University of Parma.

3. RESULTS AND DISCUSSION

Thermodynamics of equilibria in methanol:water = 9:1 v/v solution by ITC[1]

The speciation in methanol:water = 9:1, the solvent in which the greatest part of our ligands is soluble, and formation constants of their complexes with divalent metal ions, have been carefully defined to gain a deeper insight on the mechanism of action of the new potential drugs. Isothermal titration calorimetry (ITC) in methanol:water = 9:1 solution could provide useful information in this direction by studying the complete thermodynamics of complexes formation in solution[68,69]. We decided to refine the experimental method in order to obtain reliable results, due to the lack of information in literature about this subject. For this purpose, we have chosen to study the thermodynamics of the complexation of the ligand HL (Figure 53), a simplified model of Raltegravir, with Mg(II), Mn(II), Co(II) and Zn(II), because most enzymes that participate in the biochemistry of nucleic acids require divalent metal ion cofactors to promote activity[70]. Having already determined the speciation by potentiometry of the above systems (Table 15), we decided to perform ITC experiments in the same experimental conditions (same solvent, same ionic strength, same ligand/metal ratio, same titrant), simply scaling up the experiments to the microcalorimetric requirements.

Table 15.

Standard thermodynamic parameters for the complexes formation between the HL ligand and some divalent metal ions. Standard deviations ae reported in parenthesis. Ref.[1].

			Mg(II)		Mn(II)		Co(II)		Zn(II)	
p	**q**	**r**	**Log β_{pqr}** [b]	**ΔH kJ mol^{-1} ΔS J mol^{-1} K^{-1}**	**Log β_{pqr}** [b]	**ΔH kJ mol^{-1} ΔS J mol^{-1} K^{-1}**	**Log β_{pqr}** [b]	**ΔH kJ mol^{-1} ΔS J mol^{-1} K^{-1}**	**log β_{pqr}**	**ΔH kJ mol^{-1} ΔS J mol^{-1} K^{-1}**
1	1	0	5.11 (0.23)	5,9 (0,7) 118(5)	5.93 (0.07)	-2,0 (0,6) 107(3)	6.91 (0.03)	-1,4 (0,5) 128(2)	4.87 (0.20)	-17,0 (0,8) 37(4)
1	2	0	9.08 (0.22)	1,7 (0,8) 180(5)	10.18 (0.07)	-6,2 (0,8) 175(3)	11.67 (0.06)	-5,5 (0,7) 205(3)	9.29 (0.11)	-28,6 (0,4) 83(3)
1	0	-2[a]							-19.90 (0.22)	+34,0(1.0) -267(10)
0	1	1	L + H ↔ LH		Log β_{011}= 8.639 (0.002			-7,1 (0,1) 141,6(3)		

[a] $Zn(OH)_2$, considered to obtain a good fit of the potentiometric data [67]

[b] From Ref. [7]

The data were processed by means of the HypΔH software[67] that enables the calculation of the formation enthalpies using previously determined stability constants[8] obtained by potentiometry and to evaluate from the microcalorimetric titrations the heats of formation of the complexes. To avoid the presence of bubbles in both titrate and titrant solutions, the reagents were degassed under vacuum before the experiments, in order to obtain good microcalorimetric titration. When the solvent is formulated principally with methanol, due to his greater vapor pressure, this operation could change significantly the concentrations of the starting solutions, so invalidating the fit by the HypΔH software. We decided to standardize the solutions after degassing[1]. Moreover, the syringe must be filled up by KOH solution in dry box saturated with nitrogen, avoiding CO_2 absorption from the atmosphere by the alkaline solution. The second problem to face with was to find out the water formation heat in methanol:water = 9:1 solution at ionic strength 0.1 M KCl, a value absolutely needed to extract from the experimental data the correct heats of formation of the complexes. Also in this case, literature data about this subject are almost lacking. The molar enthalpy change for the reaction $H^+ + OH^- = H_2O$ has been obtained by titrating a solution of HCl with KOH, both prepared in the mixed solvent (methanol:water = 9:1 v/v, I = 0.1 M KCl). It results -20.6±0.4 kJ mol^{-1} [1], a value very different from the same obtained in pure water (-55.83 kJ mol^{-1}). The protonation heat of the ligand was obtained by titrating HL in the cell by a KOH solution, and subtracting, as for all our experiments, the dilution heat of the titrant. As reported in Table 15, it results -7.1(1) kJ mol^{-1} [1]. This is the starting point for evaluating the formation heats of the complexes with the metal ions (Table 15) by the HypΔH software. In Figure 62 is reported an example of the output of a microcalorimetric titration for the system Zn(II):HL = 1:4 [1].

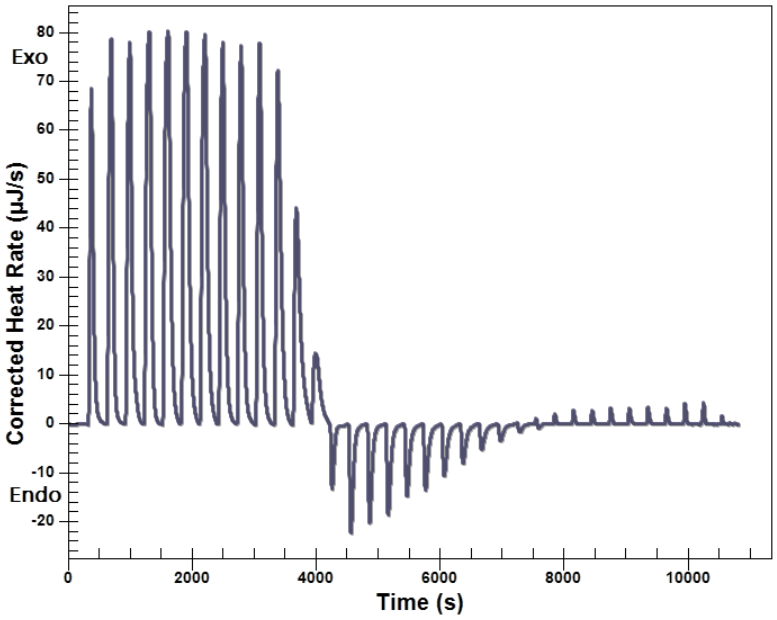

Figure 62. Calorimetric signal as a function of the injection number for the system Zn(II):HL = 1:4 in methanol:water = 9:1 0.1M KCl as ionic strength, titrated by KOH 0.145 M in the same solvent. The cell was prepared with 0.7156 µmole of Zn(II), 2.8613 µmole of HL and 1.0312 µmole of H^+ added as HCl. Ref.[1].

For the same system, in Figure 63 it is shown the nice agreement between experimental and calculated thermal data in relation with the distribution diagram of the species from the HypΔH output for the Zn(II):HL = 1:4 system[1].

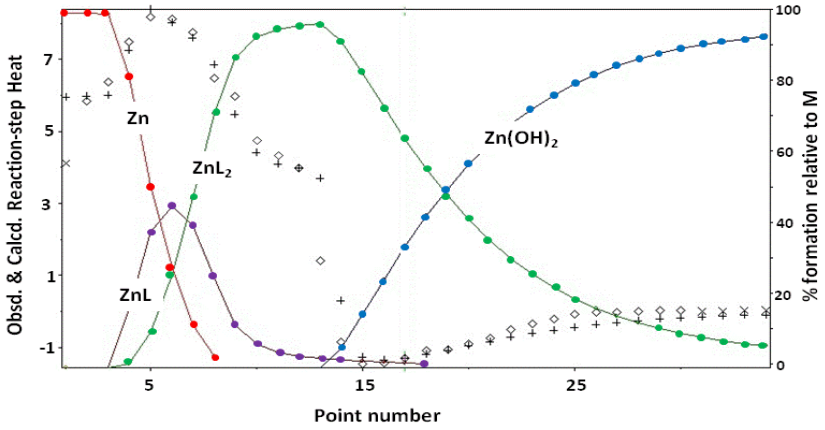

Figure 63. Observed (◊) and calculated (+) step reaction heats for the Zn(II):HL = 1:4 in methanol:water = 9:1, I = 0.1M KCl. In the same figure the distribution diagram of the species. Ref.[1].

The interaction between HL and all the divalent metal ions investigated, give rise to the same complex species in solution, namely ML and ML_2. Moreover, Mn(II) and Co(II) exhibit a very similar thermodynamic behavior, with a low negative enthalpic and a greater positive entropic contributions[1]. Both the CoL and CoL_2 complexes show the greatest affinity due to the more negative value of $\Delta G°$. Only Mg(II) complexes display a positive formation enthalpy; consequently their formation is entropy driven. In fact the Mg(II) ion is characterized by a high charge density, small ionic radius and tendency to bind water molecules in the inner coordination sphere. Thermodynamic data suggest that the molecule (HL) under study is able to substitute water in the inner sphere, consuming energy but with an entropic gain due to the solvent molecules released. Zn(II) shows the highest favorable enthalpy and the lowest positive entropy contribution, suggesting a different coordination mechanism.

Salicylamides derivatives

The speciation of salicylamides derivatives with magnesium ions has been previously investigated by potentiometry but nothing is known about their ability to bind divalent metal ions of the first transition series, especially Cu(II). Following the Pearson's classification of metal ions[61], after having studied the complexation ability of the 2-hydroxyamide ligands with a hard Lewis acid like Mg(II), we here report the speciation in solution of the same ligands with a "soft" metal ion like Cu(II). Moreover, we have proved that transition metal complexes of chelating inhibitors shows an interesting antiviral activity[71]. Therefore, we studied by potentiometry in mixed solvent methanol:water = 9:1 and ionic strength 0.1 M KCl the solution behavior of GR26 (HL^1), GR28 (H_2L^2), and GR30 (HL^3) with Cu(II). We recall that the acidity (pK_a) of

the salicylic OH of the ligands resulted 9.51(0.01) for GR26, 9.10(0.01) for GR28, and 7.28(0.01) for GR30 and that the second acidity constant (pK_{a2}) for GR28 is greater than 12, out of the working range of the glass electrode[63].

The thermodynamic study of the protonation of the ligands was completed by performing ITC experiments in the same mixed solvent and at the same ionic strength of the potentiometric titrations, using the procedure above described. The protonation reactions of all the compounds under study, have been completely thermodynamically evaluated by using potentiometric titration to determine the pKa values and isotherm micro-calorimetric titration to measure the heat absorbed or released during the reaction and the correspondent enthalpic and enthropic variations.

The data were processed by means of the HypΔH software[67] and results are shown in Table 16.

Table 16. Thermodynamic parameters for the protonation of the ligands under study. In brackets the standard deviation on the last figure.

	$\log K_1$	ΔG (kJ mol^{-1})	ΔH (kJ mol^{-1})	ΔS (J K^{-1}mol^{-1})
GR26 (HL^1)	9.51	-54.27 (2)	-10.9 (1)	145 (2)
GR28 (H_2L^2)	9.11	-51.99 (2)	-16.9 (5)	117 (4)
GR30 (HL^3)	7.28	-41.54 (2)	-8.6 (2)	110 (2)

By way of an example, in Figures 64-66 the experimental data from ITC and the comparison between experimental and computed cumulative heats for are reported.

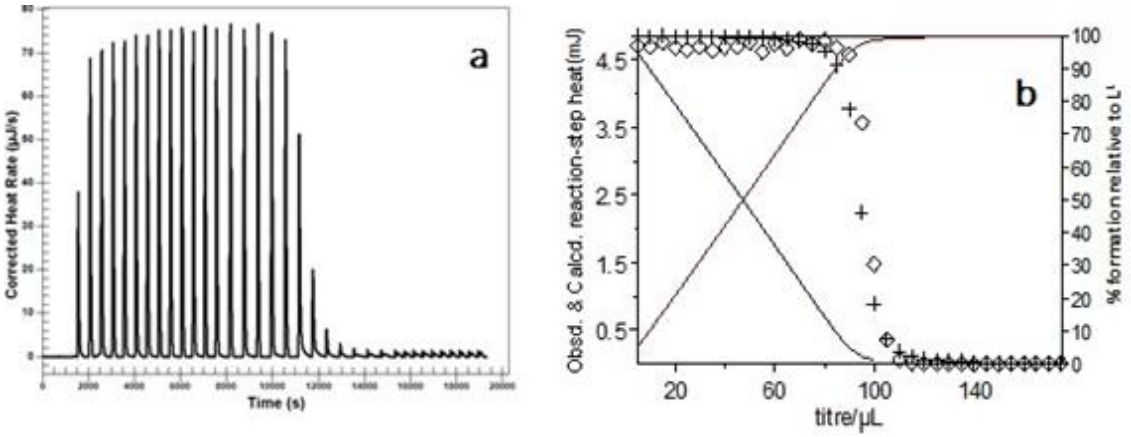

Figure 64. a | Raw data from the ITC titration for the protonation of GR26 (HL^1). Upward peaks indicate an exothermic reaction. Each peak corresponds to a single 5 µl injection. **b** | Comparison between experimental and computed stepwise heats (output from HypΔH software). Experimental conditions: inside the cell GR26 9.5 µmoles, titrant KOH 0.1 M.

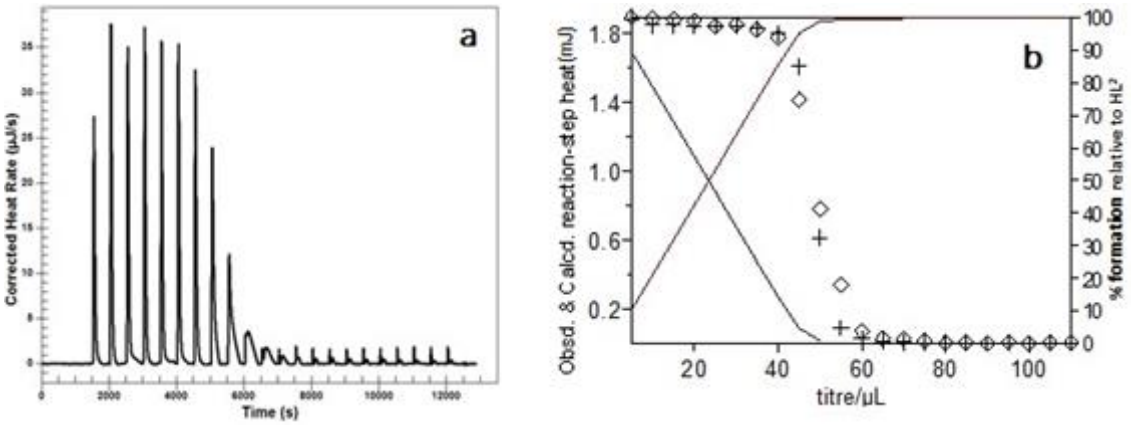

Figure 65. a | Raw data from the ITC titration for the protonation of GR28 (H_2L^2). Upward peaks indicate an exothermic reaction. Each peak corresponds to a single 5 µl injection (titrant KOH 0.1 M). **b** | Comparison between experimental and computed stepwise heats (output from HypΔH software). Experimental conditions: inside the cell GR28 4.75 µmoles, titrant KOH 0.1 M.

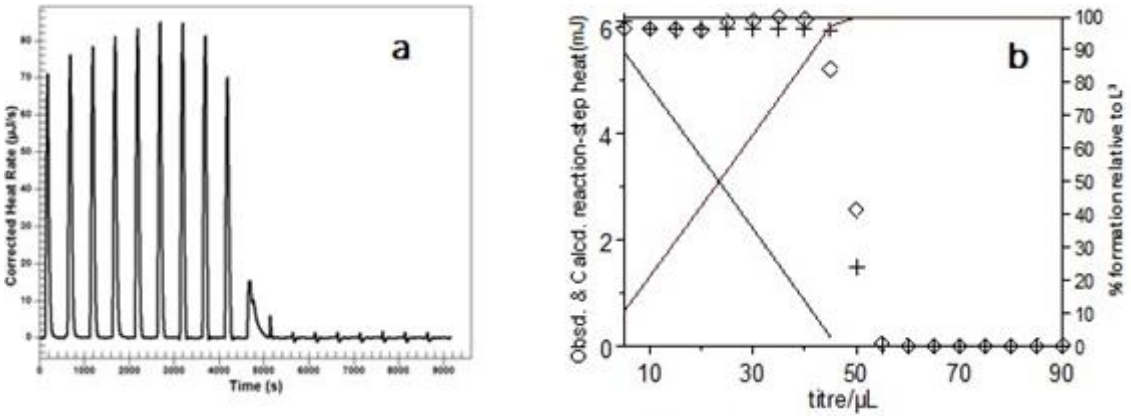

Figure 66. a | Raw data from the ITC titration for the protonation of GR30 (HL^3). Upward peaks indicate an exothermic reaction. Each peak corresponds to a single 5 μl injection (titrant KOH 0.1 M). **b** | Comparison between experimental and computed stepwise heats (output from HypΔH software). Experimental conditions: inside the cell GR30 4.75 μmoles, titrant KOH 0.1 M.

As far as the potentiometric titrations of the ligand:Cu(II) systems are concerned, we had to face with the poor solubility of the systems GR26:Cu(II) and GR30:Cu(II) in a given pH range. In particular, for GR26, we found the presence of precipitate in the pH range 6 – 8 for the metal:ligand ratio 1:2 and only around pH 6 for the metal:ligand ratio 1:4, while for compound GR30 the precipitate is formed above pH = 8 for the 1:4 ratio and above pH = 9 for 1:2 ratio.

Table 17 refers the models of speciation in solution for the ligands under study and Cu(II) ions, showing the best statistical parameters and the best fit between experimental and computed potentiometric titration curves.

Table 17.

Logarithms of the formation constants ($\beta_{pqr} = [M_pL_qH_r]/[M]^p[L]^q[H]^r$) in methanol:water = 9:1 v/v, I = 0.1 M KCl at 25°C for the ligands under study with Cu(II). SDs are given in parentheses. The monodeprotonated ligands are indicated by L, i.e. L^1, HL^2 and L^3. Charges are omitted for simplicity.

				GR26 (HL^1)	**GR28** (H_2L^2)	**GR30** (HL^3)
p	**q**	**r**		**Log β_{pqr}**	**Log β_{pqr}**	**Log β_{pqr}**
1	1	0		5.66 (0.37)	8.74 (0.06)	5.42 (0.06)
1	2	0		8.99 (0.47)		9.22 (0.10)
1	2	-1		0.10 (0.38)	4.53 (0.07)	0.82 (0.08)
1	2	-2		-12.02 (0.38)	-6.70 (0.11)	
0	1	1	$L + H \leftrightarrow LH$	9.51 (0.01)	9.11 (0.01)	7.28 (0.01)

The distribution diagrams as a function of the pH, evaluated for L:Cu = 4:1 at a Cu(II) concentration equal to 1.25 mM, are reported in Figure 67.

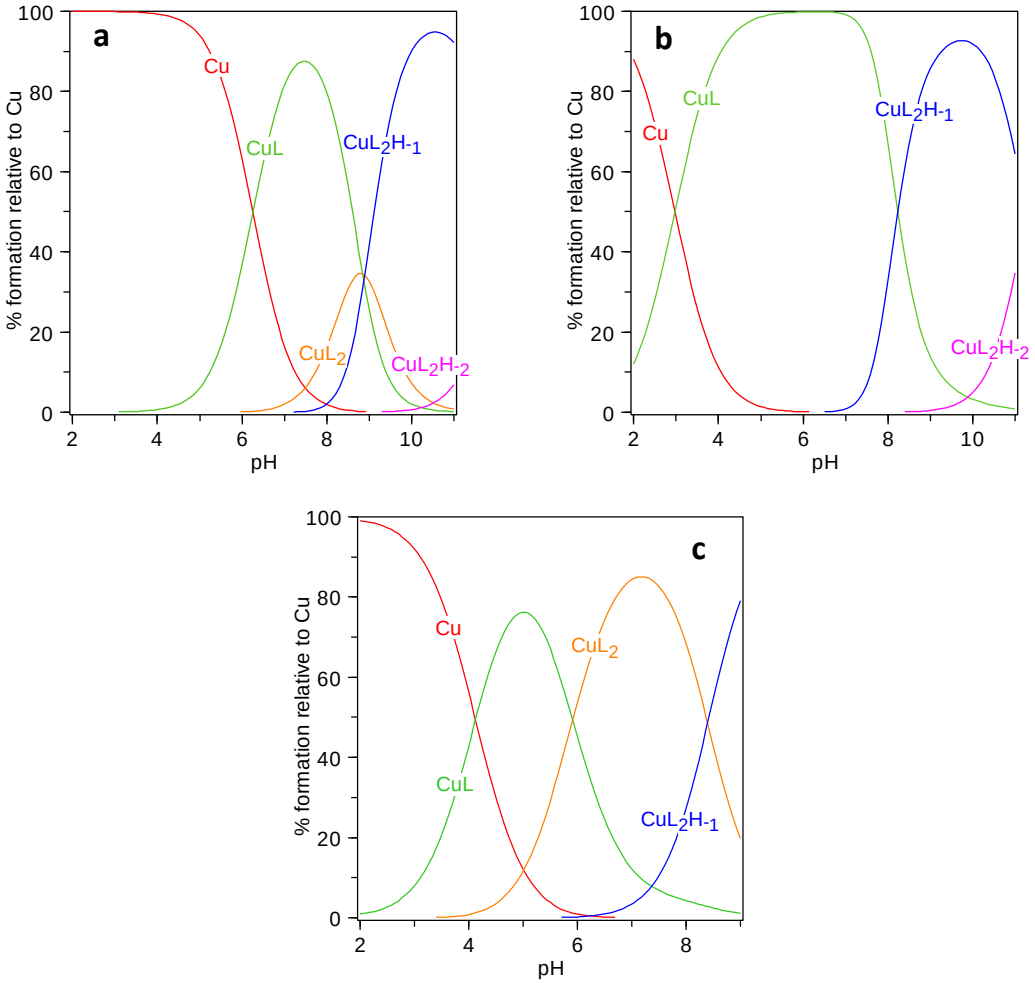

Figure 67. Distribution diagrams for the systems L:Cu = 4:1 (Cu(II) concentration = 1.25 mM). **a** | GR26-Cu(II); **b** | GR28-Cu(II); **c** | GR30-Cu(II). The monodeprotonated ligands are indicated by L, i.e. L^1, HL^2 and L^3. Charges are omitted for simplicity.

As expected, the ligands show a greater affinity towards Cu(II) than towards Mg(II). While Mg(II) is able to bind the ligands only starting at a pH at which they are already deprotonated, probably forming outer sphere complexes, Cu(II) is able to lower the pK_a value of the ligands of a few units forming complex species already at acidic pH. GR26

(HL^1) and GR30 (HL^3) give rise to the same species in solution, with similar affinity, namely CuL, CuL_2 and CuL_2H_{-1}. In the case of GR26, we suggest that the precipitate formed around pH 7 could be the neutral species CuL_2 that resolubilizes forming CuL_2H_{-1}. Moreover, for GR26 we were able to find out also the species CuL_2H_{-2}, formed beyond pH 10 and probably due to the dissociation of two water molecules completing the coordination sphere of the Cu(II) ion. It was not possible to search for this species in the case of GR30, because the solution is turning opaque beyond pH 9, probably due to the precipitation of hydroxylated compounds. GR28 (H_2L^2) gives rise to the same species as GR26 (HL^1), but seems unable to form the complex CuL_2, that was always discarded by the software in every combination tested. We recall that, in this case, the monodeprotonated ligand, i.e. HL^2, is indicated by L.

At physiological pH the species CuL_2 is the most abundant for GR30 (HL^3), reaches only a few percent for GR26 (HL^1) and is completely absent for GR28 (H_2L^2). These last two ligands at neutral pH form preferably the species ML. We have examined the hypothesis of the formation in solution of di-metallic species, but they were always rejected by the software. We cannot exclude that in different conditions, when locally the concentration of copper is high, like inside an active site of a metal-enzyme, dinuclear complexes can form.

The ligands and their complexes were tested as antiviral activity both with enzymatic and cellular assays at the Rega Institute for Medical Research, KU Leuven (Belgium).

The hydroxybenzamide-based ligands GR26-GR30 and their magnesium(II) complexes were previously tested for their ability to inhibit the endonuclease activity of PA-Nter in an enzymatic assay with recombinant PA-Nter[58]. Complex (GR28-Mg) proved to be the most active compound, with an IC_{50} = 18 μM, which is 6-fold higher than that of

the reference compound DPBA (2,4-dioxo-4-phenylbutanoic acid) and it is lower than the value of the corresponding free ligand GR28 (IC_{50} = 33 µM). On the contrary, GR26 e GR30 and their Mg(II) complexes, did not inhibit the endonuclease reaction at 500 µM, the highest concentration tested[58].

Hydrazones-derivatives

Hydrazones-derived ligands, shown in Figure 57**b**, were also studied in solution with Mg(II) and Cu(II) ions. The protonation constants were obtained by titrating 20 ml of samples of each ligand (3 x 10^{-3} M) and the HYPERQUAD software was used to obtain the cumulative formation constants[66]. These compounds show a lower acidity than the salicylamides derivatives. Compound GR55 differs from GR31 for the substitution of the aliphatic part with an aromatic ring, with a reduction of the acidity of the o-vanillin hydroxyl. The structure of compound DR31 differs from GR31 for the introduction of a hydroxyl- substituent on the benzene aromatic ring. This implies, as expected, an acidity increment of the o-vanillin hydroxyl with a pK_a two units lower than that of GR31. DR31 is a diprotic acid with pK_{a1} = 8.43 and pK_{a2} = 12.11.

As for the salicylamidic derivatives, the thermodynamic parameters obtained by ITC titration (Table 18) suggest that the protonation is entropically and enthalpically favored.

Table 18. Thermodynamic parameters for the protonation of the ligands under study at 298 K. In brackets the standard deviation on the last figure.

	$logK_a$	ΔG (kJ mol $^{-1}$)	ΔH (kJ mol $^{-1}$)	ΔS (J K $^{-1}$ mol $^{-1}$)
GR55	11.18 (0.01)	-63.9 (2)	-11.1 (2)	177 (3)
GR31	10.64 (0.01)	-60.6 (2)	-15.6 (7)	151 (4)
DR31	8.43 (0.01) 12.11 (0.01)	-68.8 (2) -78.8 (2)	-8 (3) -18 (3)	204 (9)

The ΔH values reported in Table 18 correspond to the enthalpies of formation associated to this reaction:

$$L + H \rightarrow LH$$

and, in the case of compound DR31, to the reaction

$$LH + H \rightarrow LH_2$$

In Figures 68-70 below, are reported the results obtained from ITC protonation experiment of these ligands.

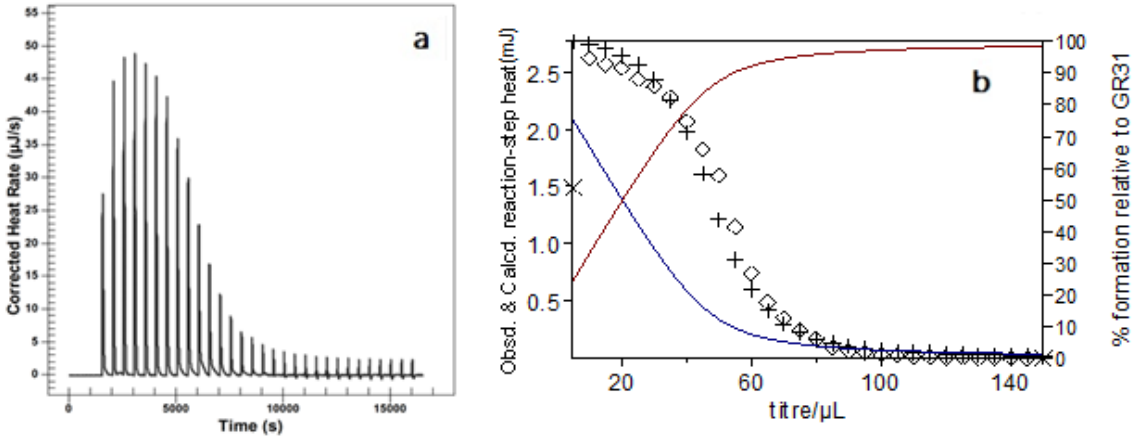

Figure 68. a | Raw data from the ITC titration for the protonation of GR31. Upward peaks indicate an exothermic reaction. Each peak corresponds to a single 5 µl injection (titrant KOH 0.1 M). **b** | Comparison between experimental and computed stepwise heats (output from HypΔH software). Experimental conditions: inside the cell GR31 5.7 µmoles, titrant KOH 0.1 M.

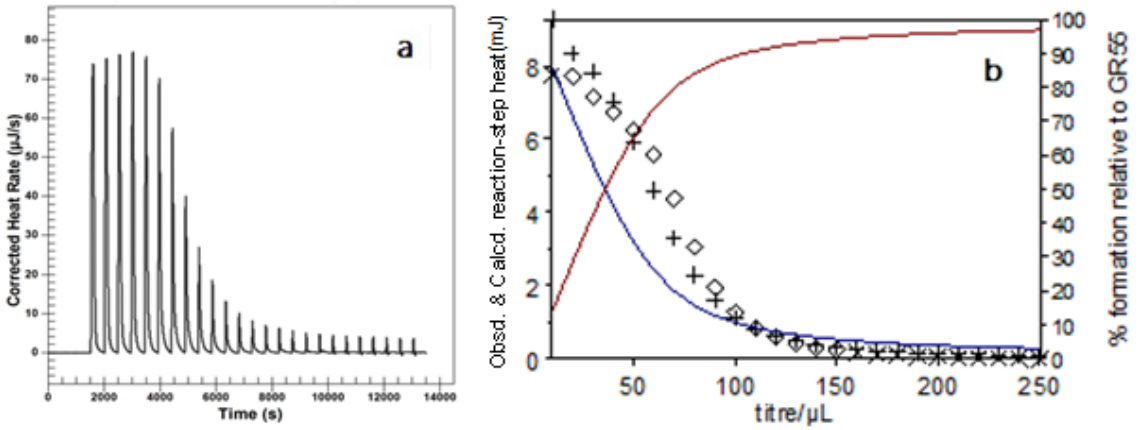

Figure 69. a | Raw data from the ITC titration for the protonation of GR55. Upward peaks indicate an exothermic reaction. Each peak corresponds to a single 5 µl injection (titrant KOH 0.1 M). **b** | Comparison between experimental and computed stepwise heats (output from HypΔH software). Experimental conditions: inside the cell GR55 6.1 µmoles, titrant KOH 0.1 M.

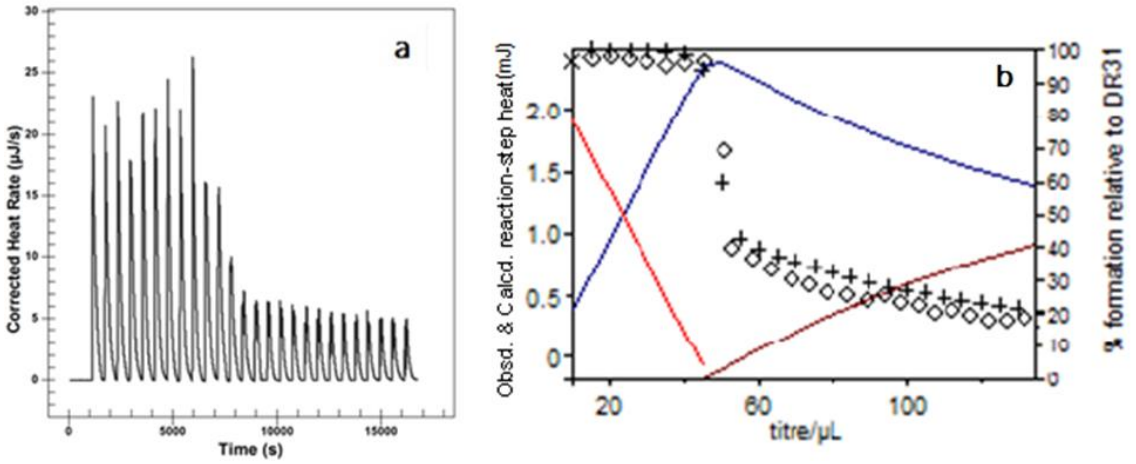

Figure 70. a | Raw data from the ITC titration for the protonation of DR31. Upward peaks indicate an exothermic reaction. Each peak corresponds to a single 5 μl injection (titrant KOH 0.1 M). **b** | Comparison between experimental and computed stepwise heats (output from HypΔH software). Experimental conditions: inside the cell DR31 2.38 μmoles, titrant KOH 0.1 M.

This class of ligands present a chelating-triad potentially able to chelate metal ions. To obtain the complex formation constants, the titrations were performed in different ligand/metal ratios (from 1 up to 4).

In Table 19, the models of speciation in solution for the ligands under study with Mg(II) and Cu(II) ions, showing the best statistical parameters and the best fit between experimental and computed potentiometric titration curves, are shown.

Table 19.

Summary table of the constant logs of the protonation and the complexes formation ($ß_{pqr}$ = $[M_pL_qH_r]/[M]^p[L]^q[H]^r$) between the hydrazones derivatives with Mg(II) and Cu(II), in the mixed solvent MeOH:H_2O in 9:1 ratio. The standard deviations are reported in brackets. Charges are omitted for simplicity.

				GR31	**GR55**	**DR31**
					Mg(II)	
p	**q**	**r**		**log β_{pqr}**	**log β_{pqr}**	**log β_{pqr}**
1	1	0		5.04 (0.04)	5.29 (0.06)	7.64 (0.02)
1	2	0		9.46 (0.03)	9.47 (0.42)	11.76 (0.07)
1	1	1				14.87 (0.17)
1	2	1				22.04 (0.13)
1	0	-2				-21.42 (0.09)
					Cu(II)	
1	1	0		11.97 (0.24)	11.84 (0.06)	18.60 (0.05)
1	1	-1		7.58 (0.24)	6.41 (0.06)	6.73 (0.07)
1	2	-1		10.92 (0.25)	10.12 (0.07)	10.27 (0.18)
1	2	-2		-0.78 (0.24)	-2.03 (0.07)	-1.49 (0.09)
0	1	1	$L + H \leftrightarrow LH$	10.64 (0.01)	11.18 (0.01)	8.43 (0.01)
0	1	2	$LH + H \leftrightarrow LH_2$			12.11 (0.01)

The distribution diagrams as a function of the pH, evaluated for L:Mg = 4:1 at a Mg(II) concentration equal to 1.25 mM, are reported in Figure 71.

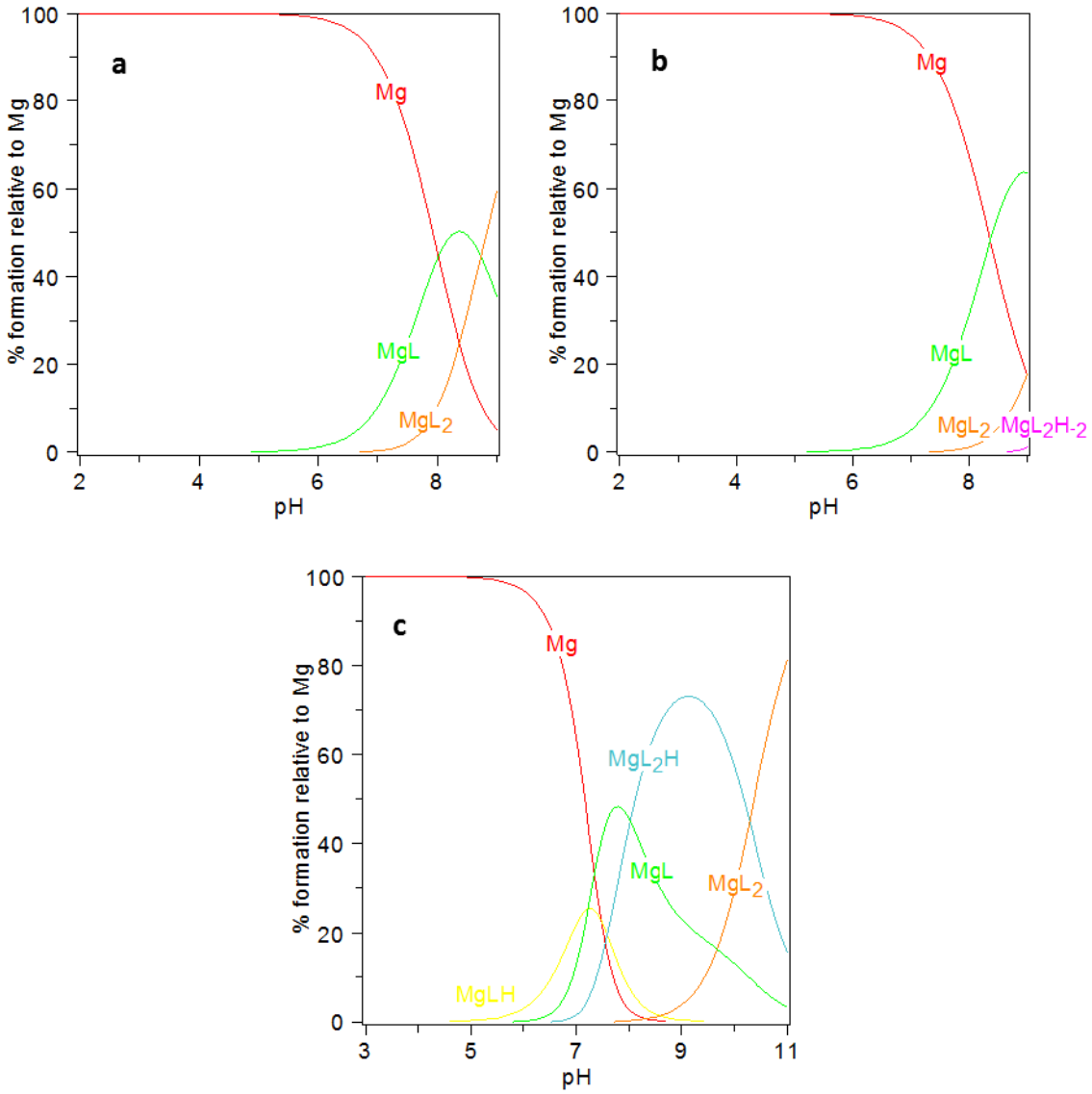

Figure 71. Distribution diagrams for the systems L:Mg=4:1 (Mg(II) concentration = 1.25 mM). **a** | GR31-Mg(II); **b** | G55-Mg(II); **c** | DR31-Mg(II). Charges are omitted for simplicity.

In the case of the complexes with Mg(II), the distribution diagrams of all three compounds show that this metal is poorly chelated at physiological pH. For GR55 and GR31, the ML species at pH 7.4 is present at nearly 15% and 25% respectively. This

complex starts forming at a pH value under pH 7 at which, in the absence of metal ions, the ligands would still be protonated. This means that the coordination with metal ions makes the o-vanillin hydroxyl more acidic. DR31 forms at physiological pH a 10% of MLH, in which the first proton has been removed, and a 30% of the completely deprotonated ML species. Staring from pH about 9 the solution becomes cloudy for the formation of a precipitate, probably the species ML_2.

In the case of Cu(II), in general, all hydrazones under study are able to form complexes with this metal, with an increased affinity respect to the salycilamidic compounds. The ligands show a greater affinity towards Cu(II) than towards Mg(II). The copper(II) ion greatly increases the acidity of the amidic hydrogen and induces its deprotonation. The three ligands give rise to the same species in solution, with similar affinity. The model is well-supported by good statistical parameters and from the perfect superposition of the calculated and experimental curves.

The distribution diagrams (Figure 72) show that Cu(II) is already complexed at acidic pH. GR55 and GR31 form, at lower pH values, the ML species that lose another proton above pH 3, giving rise to the MLH_{-1}, the most prevalent at physiological pH. Above pH 9, a second molecule of ligand binds the MLH_{-1} to form the ML_2H_{-1} that evolve in the ML_2H_{-2} at higher pH. In the case of compound DR31, only the ML species is present in the range $3<pH<9$. It is worth noting that this ML species corresponds to the MLH_{-1} of GR55 and GR31 because DR31 is the only one diprotic hydrazone.

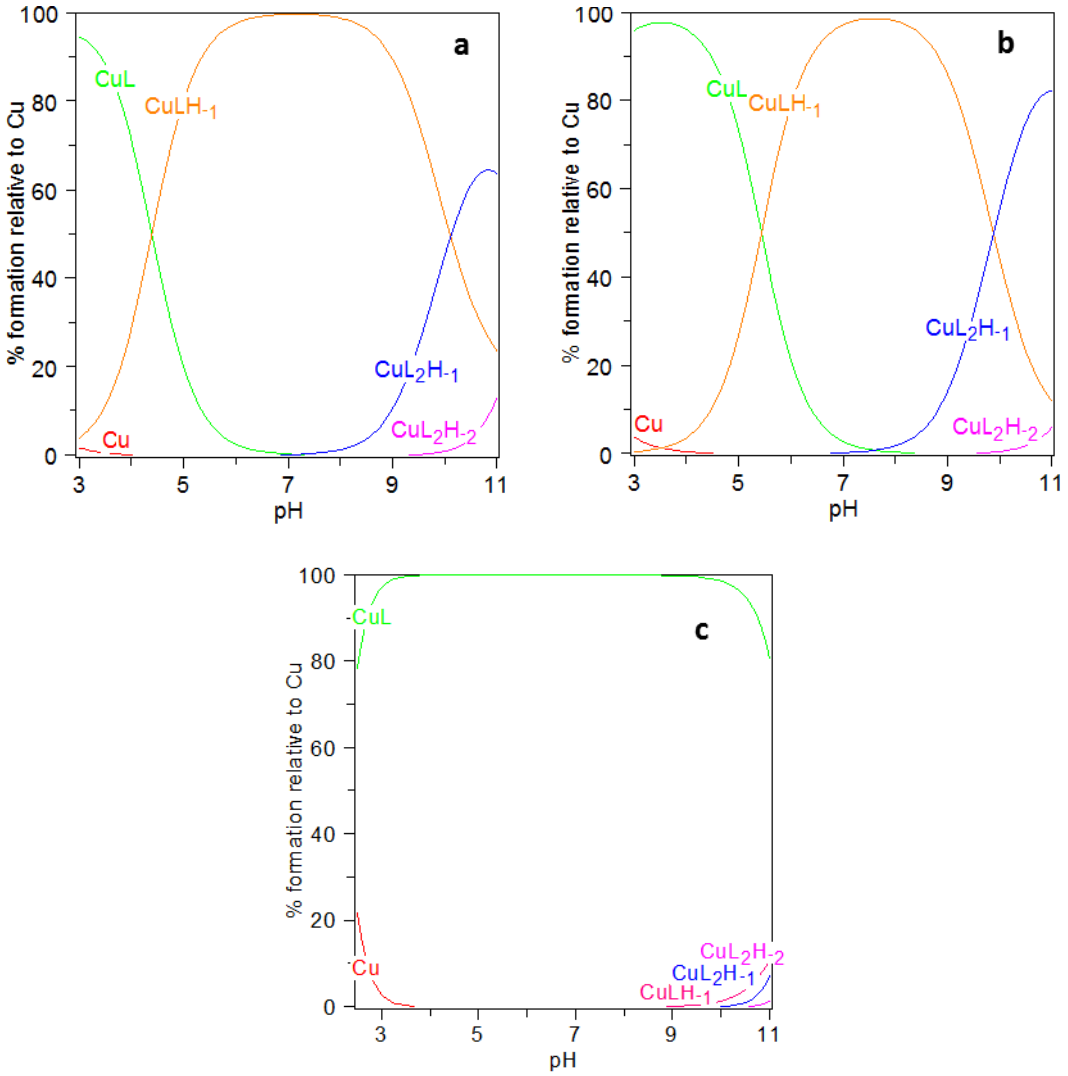

Figure 72. Distribution diagrams for the systems L:Cu=4:1 (Cu(II) concentration = 1.25 mM). **a** | GR31-Cu(II); **b** | GR55-Cu(II); **c** | DR31-Cu(II). Charges are omitted for simplicity.

We cannot exclude the presence of species with general formula M_nL_n: the mathematical algorithm used to find out the species in solution cannot distinguish between the different *n* values, because the correlation between the species does not allow the convergence of the iterative calculation. Effectively, as already discussed[72], mass spectrometric data confirm the formation of Cu_4L_4 also in solution, in agreement with the structure (Figure 73) of the complex isolated in the solid state.

Biological assays for these molecules are underway of study at the Rega Institute for Medical Research, KU Leuven, Belgium.

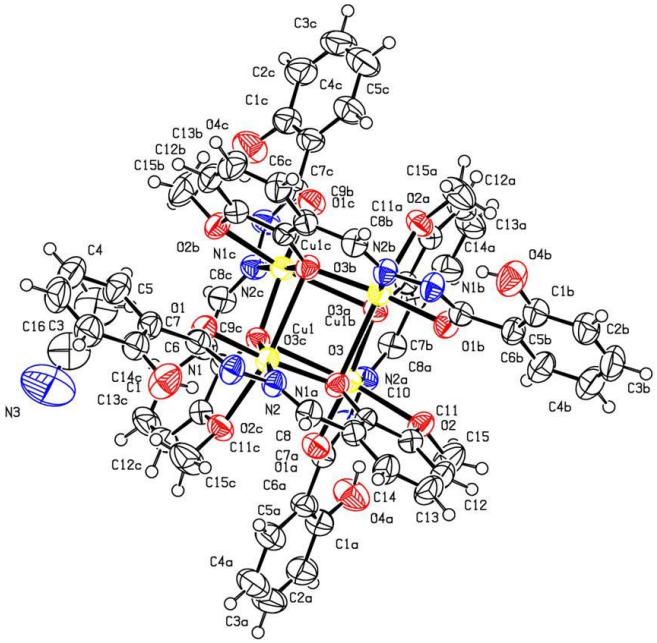

Figure 73. Ellipsoid plot of DR31[72].

4. CONCLUSIONS

CONCLUSIONS

This study was focused on the design, synthesis, chemical and biological evaluation of some scaffolds containing a chelating motif able to bind one or two metal ions in the active site of some viral enzymes, so inhibiting viral replication. Analysis of the potentiometric and X-ray data demonstrated the metal-complexing ability of 2-hydroxyamide- and acylhydrazone-based scaffolds. Salycilamides and their Mg(II) complexes, studied for their interesting biological properties for a long time, have interesting *in vitro* activities against influenza virus. Their complexing properties, examined also by means of potentiometric techniques in solution, suggest that their activity can be due to the possibility to chelate the Mg(II) ions in the active site of influenza virus endonuclease. The results obtained from the potentiometric studies and the molecular modeling analysis suggest that GR28 could effectively interact with the two metal ions present in the active site of the enzyme, by using the catechol and the amide oxygen, and, in this way, it could exercise its biological activity. Obviously, the mechanism of action and the precise viral target of the compounds presented here remain to be identified and further investigations will be performed. In fact, biological assays of acylhydrazone-based scaffolds are still in progress. To the best of our knowledge, no data are present in literature on antiviral activity of metal complexes of hydrazones ligands on DNA-viruses and this study can help to relate the structural characteristics of the complexes to their antiviral activity.

5. REFERENCES

REFERENCES

[1] Fisicaro, E.; Compari, C.; Bacciottini, F.; Contardi, L.; Carcelli, M.; Rispoli, G.; Rogolino, D., Thermodynamics of complexes formation by ITC in methanol/water = 9/1 (v/v) solution: A case study. *Thermochimica Acta*, **2014**, *586*, 40-44.

[2] Bruijnincx, P.C.A.; Sadler, P.J. New trends for metal complexes with anticancer activity. *Curr. Opin. Chem. Biol.*, **2008**, *12*, 197–206.

[3] Chi-Ming Che, Fung-Ming Siu, Metal complexes in medicine with a focus on enzyme inhibition. *Curr. Opin. Chem. Biol.*, **2010**, *14*, 255–261.

[4] Sadler, P.J.; Guo, Z. Metal complexes in medicine: design and mechanism of action. *Pure Appl. Chem*., **1998**, *70*, 863–871.

[5] Sekhon, B.S. Inorganics/bioinorganics: biological, medicinal and pharmaceutical uses, *J. Pharm. Educ. Res*., **2011**, *2*, 1-20.

[6] Thompson, K.H.; Orvig, C. Boon and bane of metal ions in medicine. *Science*, **2003**, *300*, 936.

[7] Dik-Lung Ma; Hong-Zhang He; Ka-Ho Leung; Shiu-Hin Chan; Chung-Hang Leung, Bioactive luminescent transition-metal complexes for biomedical applications. *Angew. Chem. Int. Ed*., **2013**, *52*, 7666–7682.

[8] Bacchi, A.; Carcelli, M.; Compari, C.; Fisicaro, E.; Pala, N.; Rispoli, G.; Rogolino, D.; Sanchez, T.W.; Sechi, M.; Sinisi, V.; Neamati, N. Investigating the role of metal chelation in HIV-1 integrase strand transfer inhibitors. *J. Med. Chem.*, **2011**, *54*, 8407–8420.

[9] Bacchi, A.; Biemmi, M.; Carcelli, M.; Carta, F.; Compari, C.; Fisicaro, E.; Rogolino, D.; Sechi, M.; Sippel, M.; Sotriffer, C.A.; Sanchez, T.W.; Neamati, N. From ligand to complexes. Part 2. Remarks on human immunodeficiency virus type 1 integrase inhibition by diketoacid metal complexes. *J. Med. Chem.*, **2008**, *51*, 7253–7264.

[10] Sechi, M.; Bacchi, A.; Carcelli, M.; Compari, C.; Duce, E.; Fisicaro, E.; Rogolino, D.; Gates, P.; Derudas, M.; Al-Mawsawi, L.Q.; Neamati, N. From ligand to complexes: inhibition of human immunodeficiency virus type 1 integrase by β-Diketo acid metal complexes. *J. Med. Chem.*, **2006**, *49*, 4248–4260.

REFERENCES

[11] Bacchi, A.; Carcelli, M.; Compari, C.; Fisicaro, E.; Pala, N.; Rispoli, G.; Rogolino, D.; Sanchez, T.W.; Sechi, M.; Sinisi, V.; Neamati, N. HIV-1 IN strand transfer chelating inhibitors: a focus on metal binding. *Mol. Pharm.*, **2011**, *8*, 507–519.

[12] Brown, P.O. in: Coffin, J.C.; Hughes, S.H.; Varmus H.E. (Eds.), Integration. In Retro-Viruses, *Cold Spring Harbor Press*, Plainview, NY, **1999**.

[13] Esposito, D.; Craigie, R. Integrase structure and function. *Adv. Virus Res.*, **1999**, *52*, 319–333.

[14] Asante-Appiah, E.; Skalka, A.M. Molecular mechanisms in retrovirus DNA integration. *Antiviral Res.*, **1997**, *36*, 139-156.

[15] Neamati, N. Structure-based HIV-1 integrase inhibitor design: a future perspective. *Expert Opin. Investig. Drugs*, **2001**, *10*, 281–296.

[16] Anthony, N.J. HIV-1 integrase: a target for new AIDS chemotherapeutics. *Curr. Top. Med. Chem.*, **2004**, *4*, 979–990.

[17] Pommier, Y.; Johnson, A.A.; Marchand, C. Integrase inhibitors to treat HIV/AIDS. *Nat. Rev. Drug Discov.*, **2005**, *4*, 236–248.

[18] Dayam, R.; Neamati, N. Small-molecule HIV-1 integrase inhibitors: the 2001–2002 update. *Curr. Pharm. Des.*, **2003**, *9*, 1789–1802.

[19] Dayam, R.; Deng, J.; Neamati, N. HIV-1 integrase inhibitors: 2003–2004 update. *Med. Res. Rev.*, **2006**, *26*, 271–309.

[20] Dayam, R.; Gundla, R.; Al-Mawsawi, L.Q.; Neamati, N. HIV-1 integrase inhibitors: 2005–2006 update. *Med. Res. Rev.*, **2008**, *28*, 118–154.

[21] Cotelle, P. Patented HIV-1 integrase inhibitors (1998–2005), recent patent santi-infect. *Drug Discov.*, **2006**, *1*, 1–15.

[22] Johnson, A.A.; Marchand, C.; Pommier, Y. HIV-1 integrase inhibitors: a decade of research and two drugs in clinical trial. *Curr. Top. Med. Chem.*, **2004**, *4*, 671–686.

[23] Zeinalipour-Loizidou, E.; Nicolaou, C.; Nicolaides, A.; Kostrikis, L.G. HIV-1 integrase: from biology to chemotherapeutics. *Curr. HIV Res.*, **2007**, *5*, 365–388.

[24] Hazuda, D.J.; Felock, P.; Witmer, M.; Wolfe, A.; Stillmock, K.; Grobler, J.A.; Espe-seth, A.; Gabryelski, L.; Schleif, W.; Blau, C.; Miller, M.D. Inhibitors of strand transfer that prevent integration and inhibit HIV-1 replication in cells. *Science*, **2000**, *287*, 646–650.

[25] Goldgur, Y.; Craigie, R.; Cohen, G.H.; Fujiwara, T.; Yoshinaga, T.; Fujishita, T.; Sug-imoto, H.; Endo, T.; Murai, H.; Davies, D.R. Structure of the HIV-1 integrase catalytic domain complexed with an inhibitor: a platform for antiviral drug design. *Proc. Natl. Acad. Sci. U.S.A.*, **1999**, *96*, 13040–13043.

[26] Pais, G.C.G.; Burke, T.R. Novel aryl diketo-containing inhibitors of HIV-1 integrase. *Drugs Future*, **2002**, *27*, 1101–1111.

[27] Wang, Y.; Serradell, N.; Bolos, J.; Rosa, E.; MK-0518, HIV integrase inhibitor. *Drugs Future*, **2007**, *32*, 118–122.

[28] Rowley, M. The discovery of Raltegravir, an integrase inhibitor for the treatment of HIV infection. *Prog. Med. Chem*., **2008**, *46*, 1–28.

[29] Grinsztein, B.; Nguyen, B.Y.; Katlama, C.; Gatell, J.M.; Lazzarin, A.; Vittecoq, V.; Gonzalez, C.J.; Chen, J.; Harvey, C.M.; Isaacs, R.D. Safety and efficacy of the HIV-1integrase inhibitor raltegravir (MK-0518) in treatment-experienced patients with multidrug-resistant virus: a phase II randomised controlled trial. *Lancet*, **2007**, *369*, 1261–1269.

[30] Sorbera, L.A.; Serradell, N. GS-9137. Anti-HIV agent, HIV integrase inhibitor. *Drugs Future*, **2006**, *31*, 310–313.

[31] Sato, M.; Motomura, T.; Aramaki, H.; Matsuda, T.; Yamashita, M.; Ito, Y.; Kawakami, H.; Matsuzaki, Y.; Watanabe, W.; Yamataka, K.; Ikeda, S.; Kodama, E.; Matsuoka, M.; Shinkai, H. Novel HIV-1 integrase inhibitors derived from quinolone antibiotics. *J. Med. Chem*., **2006**, *49*, 1506–1508.

[32] Lamb, R. A.; Krug, R. M. Orthomyxoviridae: the viruses and their replication. In *Fields virology, 4th ed.* (Eds. Knipe, D. M., Howley, P. M., Griffin, D. E., Lamb, R. A., Martin, M. A., Roizman, B., Straus, S. E.) 1487-1531 (Lippincott Williams & Wilkins: Philadelphia, **2001**).

[33] World Health Organization. Influenza (seasonal)-Fact sheet N°211. http://www.who.int/mediacentre/factsheets/fs211/en/ (accessed 19-1-2015).

[34] Taubenberger, J. K.; Morens, D. M. 1918 Influenza: the mother of all pandemics. *Emerg. Infect. Dis.*, **2006**, *12*, 15-22.

[35] Garten, R. J.; Davis, C. T.; Russell, C. A.; Shu, B.; Lindstrom, S. et al. Antigenic and genetic characteristics of swine-origin 2009 A(H1N1) influenza viruses circulating in humans. *Science*, **2009**, *325*, 197–201.

[36] Jefferson, T.; Demicheli, V.; Di Pietrantonj, C.; Rivetti, D. Amantadine and rimantadine for influenza A in adults. Cochrane Database. *Syst. Rev.* CD001169, **2006**.

[37] Deyde, V. M.; Xu, X.; Bright, R. A.; Shaw, M.; Smith, C. B. et al. Surveillance of resistance to adamantanes among influenza A(H3N2) and A(H1N1) viruses isolated worldwide. *J. Infect. Dis.*, **2007**, *196*, 249-257.

[38] Moscona, A. Global transmission of oseltamivir-resistant influenza. *N. Engl. J. Med.* **2009**, *360*, 953-956.

[39] Memoli, M.J.; Davis, A.S.; Proudfoot, K.; Chertow, D.S.; Hrabal, R.J et al. Multidrug-resistant 2009 pandemic influenza A(H1N1) viruses maintain fitness and transmissibility in ferrets. *J. Infect Dis.*, **2011**, *203*, 348−357.

[40] van der Vries, E.; Schutten, M.; Fraaij, P.; Boucher, C.; Osterhaus, A. Influenza virus resistance to antiviral therapy. *Adv. Pharmacol.*, **2013**, *67*, 217-246.

[41] Vanderlinden, E.; Naesens, L. Emerging antiviral strategies to interfere with influenza virus entry. *Med. Res. Rev.* **2014**, *34*, 301–339.

[42] Yuan, Shuofeng; Chu, Hin; Singh, Kailash; Zhao, Hanjun; Zhang, Ke; Kao, Richard Y. T.; Chow, Billy K. C.; Zhou, Jie; Zheng, Bo-Jian A novel small-molecule inhibitor of influenza A virus acts by suppressing PA endonuclease activity of the viral polymerase. *Scientific Reports*, **2016**, *6*, 22880.

[43] Rogolino, D.; Carcelli, M.; Sechi, M.; Neamati, N. Viral enzymes containing magnesium: metal binding as a successful strategy in drug design. *Coord. Chem. Rev.*, **2012**, *256*, 3063-3086.

[44] Boivin, S.; Cusack, S.; Ruigrok, R. W.; Hart, D. J. Influenza A virus polymerase: structural insights into replication and host adaptation mechanisms. *J. Biol. Chem.*, **2010**, *285*, 28411-28417.

[45] Dias, A.; Bouvier, D.; Crépin, T.; McCarthy, A. A.; Hart, D. J. et al. The cap-snatching endonuclease of influenza virus polymerase resides in the PA subunit. *Nature*, **2009**, *458*, 914-918.

[46] Yuan, P.; Bartlam, M.; Lou, Z.; Chen, S.; Zhou, J. et al. Crystal structure of an avian influenza polymerase PA(N) reveals an endonuclease active site. *Nature*, **2009**, *458*, 909-913.

[47] Tefsen, B.; Lu, G.; Zhu, Y.; Haywood, J.; Zhao, L. et al. The N-terminal domain of PA from bat-derived influenza-like virus H17N10 has endonuclease activity. *J. Virol.*, **2014**, *88*, 1935-1941.

[48] DuBois, R. M.; Slavish, P. J.; Baughman, B. M.; Yun, M. K.; Bao, J. et al. Structural and biochemical basis for development of influenza virus inhibitors targeting the PA endonuclease. *PLoS Pathog.*, **2012**, *8*, e1002830.

[49] Bauman, J. D.; Patel, D.; Baker, S. F.; Vijayan, R. S.; Xiang, A. et al. Crystallographic fragment screening and structure-based optimization yields a new class of influenza endonuclease inhibitors. *ACS Chem. Biol.*, **2013**, *8*, 2501-2508.

[50] Doan, L.; Handa, B.; Roberts, N. A.; Klumpp, K. Metal ion catalysis of RNA cleavage by the influenza virus endonuclease. *Biochemistry*, **1999**, *38*, 5612-5619.

[51] Maret, W. Metalloproteomics, metalloproteomes, and the annotation of metalloproteins. *Metallomics*, **2010,** *2*, 117-125.

[52] Jahnen-Dechent, W.; Ketteler, M. Magnesium basics. *Clin. Kidney J.*, **2012**, *5*(suppl. 1), i3-i14.

[53] Summa, V.; Petrocchi, A.; Bonelli, F.; Crescenzi, B.; Donghi, M. et al. Discovery of raltegravir, a potent, selective orally bioavailable HIV-integrase inhibitor for the treatment of HIV-AIDS infection. *J Med. Chem.*, **2008**, *51*, 5843-5855.

[54] Johns, B. A.; Kawasuji, T.; Weatherhead, J. G.; Taishi, T.; Temelkoff, D. P. et al. Carbamoyl pyridone HIV-1 integrase inhibitors 3. A diastereomeric approach to chiral nonracemic tricyclic ring systems and the discovery of dolutegravir (S/GSK1349572) and (S/GSK1265744). *J Med. Chem.*, **2013**, *56*, 5901-5916.

[55] Hastings, J. C.; Selnick, H.; Wolanski, B.; Tomassini, J. E. Anti-influenza virus activities of 4-substituted 2,4-dioxobutanoic acid inhibitors. *Antimicrob. Agents Chemother.* **1996**, *40*, 1304-1307.

[56] Stevaert, A.; Nurra, S.; Pala, N.; Carcelli, M.; Rogolino, D. et al. An integrated biological approach to guide the development of metal-chelating inhibitors of influenza virus PA endonuclease. *Mol. Pharmacol.*, **2015**, *87*, 323-337.

[57] Parkes, K. E.; Ermert, P.; Fässler, J.; Ives, J.; Martin, J. A.; Merrett, J. H.; Obrecht, D.; Williams, G.; Klumpp, K. Use of a pharmacophore model to discover a new class of influenza endonuclease inhibitors. *J. Med. Chem.*, **2003**, *46*, 1153-1164.

[58] Carcelli, M.; Rogolino, D.; Bacchi, A.; Rispoli, G.; Fisicaro, E.; Compari, C.; Sechi, M.; Stevaert, A.; Neasen, L. Metal-chelating 2-hydroxyphenyl amide pharmacophore for inhibition of influenza virus endonuclease. *Mol. Pharmaceutics*, **2014**, *11*, 304-316.

[59] Rogolino, D.; Bacchi, A.; De Luca, L.; Rispoli, G.; Sechi M. et al. Investigation of the salicylaldehyde thiosemicarbazone scaffold for inhibition of influenza virus PA endonuclease. *J. Biol. Inorg. Chem.*, **2015**, *20*, 1109-1121.

[60] Agrawal, A.; DeSoto, J.; Fullagar, J. L.; Maddali, K.; Rostami, S.; Richman, D. D.; Pommier, Y.; Cohen, S. M. Probing chelation motifs in HIV integrase inhibitors. *Proceedings of the National Academy of Sciences of the United States of America*, **2012**, *109*, 2251–2256.

[61] Pearson, R. G. Hard and soft acids and bases. *J. Am. Chem. Soc*, **1963**, *85*, 3533-3539.

[62] Rude, R. K. Magnesium. In: Coates, P. M.; Betz, J. M.; Blackman, M.R.; Cragg, G. M.; Levine, M.; Moss, J.; White, J. D. *Eds. Encyclopedia of Dietary Supplements. 2nd ed. New York, NY: Informa Healthcare*, **2010**, 527-37.

[63] Gran, G. Determination of the Equivalence Point in Potentiometric Titration, Part II. *Analyst* (London), **1952,** 77, 661-671.

[64] Rossotti, F. J. C.; Rossotti, H. Potentiometric studies in mixed solvents. The determination of activity coefficients and junction potentials using modified Gran plots. *J. Phys. Chem.*, **1964**, *68*, 3773-3778.

[65] Fisicaro, E.; Braibanti, A. Potentiometric titrations in methanol/water medium: intertitration variability. *Talanta*, **1988**, *35*, 769-774.

[66] Gans, P.; Sabatini, A.; Vacca, A. Investigation of equilibria in solution. Determination of equilibrium constants with HYPERQUAD suite of programs. *Talanta*, **1996,** *43*, 1739-1753.

[67] Gans, P.; Sabatini, A.; Vacca, A. Simultaneous calculation of equilibrium constants and standard formation enthalpies from calorimetric data for systems with multiple equilibria in solution. *J. Solution Chem*., **2008**, *37*, 467–476.

[68] Ladbury, J.E.; Klebe, G.; Freire, E. Adding calorimetric data to decision making inlead discovery: a hot tip. *Nat.Rev./Drug Discov*., **2010**, *9*, 23–27.

[69] Ghai, R.; Falconer, R.J.; Collins, B.M. Applications of isothermal titration calorimetry in pure and applied research-survey of the literature from 2010. *J. Mol.Recognit*., **2012**, *25*, 32–52.

[70] Cowan, J.A. Metal activation of enzymes in nucleic acid biochemistry. *Chem. Rev.*, **1998**, *96*, 1067–1087.

[71] Carcelli, M.; Rogolino, D.; Sechi, M.; Rispoli, G.; Fisicaro, E.; Compari, C.; Tramontano, E.; Naesens, L. Antiretroviral activity of metal-based HIV-1 integrase inhibitors. (submitted for publication).

[72] Rogolino, D.; Carcelli, M.; Bacchi, A.; Compari, C.; Contardi, L.; Fisicaro, E.; Gatti, A.; Sechi M.; Stevaert, A.; Naesens L. A versatile salicyl hydrazonic ligand and its metal complexes as antiviral agents. *J. Inorg. Biochem*., **2015**, *150*, 9-17.

PUBLICATIONS AND CONGRESSES PARTICIPATION

Formation abroad

I have spent a period of three months during my third year at the Institut Charles Sadron (CNRS, University of Strasbourg) in Strasbourg (France) under the supervision of Professor Marie-Pierre Krafft, a leading expert in the field of fluorinated materials.

Publications

1) Fisicaro, E.; Compari, C.; Bacciottini, F.; Contardi, L.; Carcelli, M.; Rispoli, G.; Rogolino, D. Thermodynamics of complexes formation by ITC in methanolo/water=9/1 v/v solution: a case study. *Thermochimica Acta* (**2014**), *586*, 40-44.

2) Fisicaro, E.; Compari, C.; Bacciottini, F.; Contardi, L.; Barbero, N.; Viscardi, G.; Quagliotto, P.; Donofrio, D.; Różycka-Roszak, B.; Misiak, P.; Sansone, F. Nonviral gene-delivery: gemini bispyridinium surfactant-based DNA nanoparticles, *Journal of Physical Chemistry B* (**2014**), *118*, 13183-13191.

3) Barbero, N.; Magistris, C.; Quagliotto, P.; Bonandini, L.; Barolo, C.; Buscaino, R.; Compari, C.; Fisicaro, E.; Contardi, L.; Viscardi, G. Synthesis, Physicochemical Characterization, and Interaction with DNA of Long-Alkyl-Chain Gemini Pyridinium Surfactants, *Chem. Plus Chem.* (**2015**), 80 (*6*), 952-962.

4) Rogolino, D.; Carcelli, M.; Bacchi, A.; Compari, C.; Contardi, L.; Fisicaro, E.; Gatti, A.; Sechi, M.; Stevaert, A.; Naesens, L. A versatile salicyl hydrazonic ligand and its metal complexes as antiviral agents, *Journal of Inorganic Biochemistry* (**2015**), *150*, 9-17.

5) Fisicaro, E.; Contardi, L.; Compari, C.; Bacciottini, F.; Pongiluppi, E.; Viscardi, G.; Barbero, N.; Quagliotto, P.; Róztcka-Roszak, B. Solution thermodynamics of highly fluorinated gemini bispyridinium surfactants for biomedical applications, Colloids and Surfaces A: Physicochem. Eng. Aspects (**2016**), *507*, 236–242.

6) Fisicaro, E.; Contardi, L.; Compari, C.; Bacciottini, F.; Pongiluppi, E.; Viscardi, G.; Barbero, N.; Quagliotto, P.; Donofrio, G.; Krafft, M. P. Nonviral gene-delivery by highly fluorinated gemini bispyridinium surfactant-based DNA nanoparticles, *Journal of Colloid and Interface Science*, **2017**, *487*, 182–191.

7) Carcelli M.; Fisicaro, E.; Compari, C.; Contardi, L.; Rogolino, D.; Stevaert, A.; Naesens, L. Antiviral activity of some metal-chelating 2-hydroxyphenyl amides – *Journal of Inorganic Biochemistry* - submitted.

8) Contardi, L.; Fisicaro, E.; Compari, C.; Krafft, M.P. – manuscript in preparation.

Congresses participations

- **Oral presentation** "Nanoparticelle biocompatibili per il drug delivery: studio microcalorimetrico dell'interazione fra alginato e ioni calcio", 3rd workshop Scienza al CIM: la parola ai giovani, 15th November **2013**, Parma.

- **Oral presentation** "Studio microcalorimetrico dell'interazione fra glycoclusters di nuova sintesi e Concanavalina-A", 3rd workshop Scienza al CIM: la parola ai giovani, 15th November **2013**, Parma.

- **Poster presentation** "Metal-chelating 2-Hydroxyphenyl Amide Pharmacophore for Inhibition of Influenza Virus Endonuclease", 2nd IAAASS (Innovative Approaches for identification of Antiviral Agents Summer School), September 28th – October 3rd **2014**, Santa Margherita di Pula, Sardinia.

- **Poster presentation** "Nonviral Gene Delivery: Gemini Bispyridinium Surfactant-Based DNA Nanoparticles", 1st Nanoday, 28th November **2014,** Parma.

- **Poster presentation** "Biocompatible nanoparticles for drug delivery: microcalorimetric study of interaction between alginate and calcium ions.", 1st Parma Nanoday, 28th November **2014**, Parma.

- **Oral presentation** "Gemini Bispyridinium Surfactants as non-viral vectors for gene-delivery", Riunione Nazionale "A. Castellani" dei dottorandi di ricerca in discipline biochimiche, 8th – 12th June **2015**, Brallo di Pregola, Pavia.

- **Participation** International Summer School "A primer in ecological networks", 15th – 17th June **2015**, Parma.

- **Poster presentation** "DNA Nanoparticles formed by Partially Fluorinated and by Hydrogenated Gemini Bispyridinium Surfactants for Nonviral Gene-Delivery", 2nd Parma Nanoday, 3rd – 4th December **2015**, Parma.

- **Oral presentation** "Nonviral gene-delivery by highly fluorinated gemini bispyridinium surfactant-based DNA nanoparticles", 4th Workshop Scienza al CIM: la parola ai giovani, 13th June **2016**, Parma.

- **Participation** 1st ULLA Workshop – Methodologies in pharmaceutical sciences: focus on drug discovery, market access and future career possibilities, 13th – 15th July **2016**, Leuven - Belgium.